



Quantum technological applications using dissipative many-body dynamics

Der Fakultät für Mathematik und Physik
der Gottfried Wilhelm Leibniz Universität Hannover
zur Erlangung des akademischen Grades

Doktorin der Naturwissenschaften
Dr. rer. nat.

genehmigte Dissertation von

M.Sc. Meghana Raghunandan

2020

Referent : Priv.-Doz. Dr. Hendrik Weimer
Korreferenten : Prof. Dr. Klemens Hammerer
: Prof. Dr. Markus Müller
Tag der Promotion : 06.05.2020

Abstract

Quantum systems cannot always be treated as isolated from their surroundings since this is an idealization which is not always true. Though theoretical analysis of open quantum systems poses great challenges as one needs to treat many-particle quantum systems as a whole, the system-environment interactions often lead to many interesting effects that are not observed in closed systems. The dissipation of a quantum system is not always a disadvantage and, in fact, if exploited properly in combination of coherent driving, one can steer the system into a desired state. This dissipation driven quantum state engineering technique finds its applications in novel technologies such as quantum computing, quantum simulation, and quantum metrology. In this thesis, we focus on the latter two, and show that using dissipative channels allows us to build quantum devices that have considerable advantages over their entirely coherent analogues.

Simulation of many-body problems on a quantum simulator will unlock the potential to provide great insights into a large number of systems especially those that are computationally intractable or experimentally challenging. The two crucial steps towards the successful functioning of quantum simulation are the *initialization* of the quantum simulators i.e, preparing the system in a known initial state, and the *Hamiltonian engineering*. While there have been many experiments demonstrating the implementation of the Hamiltonian dynamics on the quantum simulator, work still needs to be done on the problem of preparing the simulator in a suitable quantum state. This is exactly our aim here and we propose a protocol to cool a given system into the ground state of a black-box spin Hamiltonian. The central idea is to use a dissipatively driven auxiliary spin to pull out the excitations in the system, eventually cooling it to its ground state. We show that already a single auxiliary spin is efficient in cooling the quantum simulator to a low-energy state of largely arbitrary Hamiltonians as the resources scale only polynomially with the system size. We also show that our scheme of sympathetic cooling is robust against additional sources of decoherence.

The second part of the thesis deals with nanoscale quantum sensing using dissipative first order transition in the magnetization of a system of nitrogen-vacancy point defect centers in diamond. The sensitivity of a generic quantum sensor with non-interacting particles scales as the square root of the number of particles. Therefore, a sensor with large number of particles displays a better sensitivity. However, in the interest of nanoscale sensing,

having a large number of particles implies that they are closely packed next to each other. At such high densities, the particles interact strongly with each other posing great challenges to the sensing process. Here, we show that these interactions can in fact be used to trigger a first order phase transition when coupled with controlled dissipation in the system. We study the properties of the phase transition using two- and three-dimensional setups to build a nanoscale quantum sensor that is especially robust against typical disorder imperfections or additional decoherence processes, with the sensitivity not being severely limited by the T_2 decoherence time. Since our sensing protocol does not assume too many microscopic details of the process, one can easily apply this to other areas of quantum sensing and metrology.

These results especially highlight the fact that dissipation in quantum systems, that is normally considered *unwanted*, can in fact be a powerful tool that allows us to enable a large list of quantum technologies in the future.

Keywords

Open quantum systems	Offene quantensysteme
Controlled dissipation	Kontrollierte dissipation
Ground state preparation	Grundzustandspräparation
Quantum sensing	Quanten-messung
NV centers	NV-Zentren

Contents

I	Introduction	11
	Preliminary remarks	13
1	Theory of Open Quantum Systems	15
1.1	Closed systems and coherent dynamics	15
1.2	Combined evolution of system and bath	16
1.3	The quantum master equation	18
1.3.1	Quantum dynamical semigroups	18
1.3.2	Markovian quantum master equation	19
1.3.3	Lindblad formalism	19
1.4	Wave function Quantum Monte Carlo simulation	21
1.5	Examples of dissipative processes	23
2	Theory of phase transitions	25
2.1	Classical and quantum phase transitions	26
2.2	Classification of phase transitions	28
2.3	Spin models	30
2.3.1	Ising model	30
2.3.2	Heisenberg model	34
II	Initialization of quantum simulators by sympathetic cooling	39
3	Quantum simulation	41
3.1	The working of a quantum simulator	42
3.2	The task of initialization	43
3.3	The initialization protocol	44
3.3.1	Sympathetic cooling using controlled dissipation	45

3.3.2	A measure of cooling	47
3.3.3	Control parameters of the cooling dynamics	49
3.3.4	Optimization of the control parameters	53
4	Features of the dissipative protocol	57
4.1	Efficiency of the cooling protocol	57
4.2	Preparing highly entangled states	61
4.3	Measuring the many-body gap	62
4.4	Performance under decoherence	64
4.5	Experimental realization of the protocol	65
5	Cooling of molecular ions	69
5.1	Vibrational energy levels	69
5.2	Rotational energy levels	71
5.3	Selection rules for the ro-vibrational transitions	71
5.4	Cooling to the rotational ground state	72
 III High-density quantum sensing with dissipative first order transitions		 75
6	Nitrogen-Vacancy centers in diamond	77
6.1	Electronic level structure	78
6.2	Magnetometry using NV centers	80
6.2.1	Sensitivity of the sensor	80
6.2.2	Sensing at high densities	81
7	Dissipative first order transition	83
7.1	The sensing protocol	83
7.2	Two-dimensional lattice geometry	84
7.3	Effects of long-range interactions and vacancy disorder	91
7.4	Performance under decoherence processes	93
7.5	Sensing DC fields	93
7.6	Sensitivity estimation	95
8	Three-dimensional systems	97
8.1	Cubic lattice geometry	97
8.2	Random disorder in the system	98
8.3	Temporal coherence of the NV signal	101
8.4	Error analysis	102

Contents

IV	Conclusion	105
9	Summary and outlook	107
V	Appendices	111
A	Effective operator formalism	113
B	Critical point of the finite size Ising model	117
C	Lamb-Dicke regime for long-range Ising Hamiltonian	119
D	NV spin Hamiltonian	121
	Bibliography	123
	Acknowledgements	138

Part I
Introduction

Preliminary remarks

Open quantum systems play an important role in quantum mechanics because a complete isolation of a system is impossible in real life and couplings to external environment often influence a system, greatly changing its properties [1]. Dissipation in a system is often considered a nuisance as one needs to handle the system and the environment as a whole and treating quantum systems with large (let alone infinite) degrees of freedom is extremely challenging. Though in some situations environment-induced dissipation can indeed lead to undesired decoherence [2, 3] that destroy subtle quantum mechanical correlations, in many other cases the interplay between coherent and dissipative dynamics could lead to rich physics via many interesting novel phenomena [4]. The dynamics of such driven-dissipative systems resulting in a non-equilibrium stationary state often offer a rich variety of phenomena such as steady state phase transitions [5, 6], dissipative binding mechanisms [7, 8], interaction-mediated cooling [9, 10], quantum heat switch [11], as well as non-trivial quantum effects in biological systems [12].

From a fundamental point of view and from a technological point of view, driven-dissipative quantum many-body systems have generated a tremendous amount of interest over the past decade. Ever since the initial proposal of using controlled dissipation as a tool for quantum information and quantum many-body physics [13, 14], this idea has been constantly gaining more and more momentum particularly in the area of state preparation techniques [15, 16, 17, 18, 19, 20]. These techniques have especially helped us get closer to achieving the fast emergent technology of quantum simulation.

On the other hand, driven-dissipative systems have also been employed in the area of quantum sensing and metrology. Coherent methods of quantum sensing majorly bank on minimal interaction between the sensor and the environment and therefore on dynamical decoupling protocols [21] which restrict the detection of certain kinds of fields [22]. To combat these problems, dissipative protocols have been devised and indeed such schemes employing controlled dissipation have been shown to have features that make them significantly more advantageous than their purely coherent counterparts [23, 24].

This thesis covers both the above mentioned quantum technologies enabled by controlled dissipation namely, initialization of a quantum simulator, and, high-density quantum sensing, and is therefore divided into these two main parts. They directly follow the first part which serves as an introduction to the fundamental concepts behind this thesis.

Controlled dissipation being the main topic of focus of this thesis, it would be remiss to not begin with a chapter on the theory of open quantum systems. Chapter 1 gives an introduction to open quantum systems focusing on the basic concepts and tools involved in solving them. Chapter 2 introduces the theory of phase transitions recapitulating the central ideas involved in its description using the examples of typical spin-1/2 systems.

In part II, a novel scheme for the initialization of a quantum simulator is presented. Having introduced the basic concepts behind quantum simulation in general in chapter 3, this novel cooling protocol is presented in chapter 4. The basic principle is to use a single dissipatively driven auxiliary spin to sympathetically cool a system into the ground state of a black-box spin Hamiltonian. This approach to dissipative state preparation allows to go beyond stabilizer and frustration-free systems and gives a generalized protocol for largely arbitrary Hamiltonians. The results show the scalability of the protocol and its robustness against additional decoherence processes for paradigmatic models of transverse field Ising and Ising-like chains and the antiferromagnetic Heisenberg chain. In chapter 5, we present the first steps to extend the cooling protocol to molecular ions.

Part III of the thesis proposes a second protocol that allows quantum sensing at the scale of nanometers using an interacting ensemble of nitrogen vacancy (NV) centers in diamond. The protocol relies on the existence of a first order phase transition in the NV magnetization at a critical value of the driving field. Following the introduction to NV centers and magnetometry using them in chapter 6, the protocol is introduced in chapter 7 and its main features are discussed for a two-dimensional lattice system. Chapter 8 is an extension of the protocol to three-dimensional systems.

Finally, chapter 9 summarizes the results presented here in this thesis and presents possible directions for future research.

Chapter 1

Theory of Open Quantum Systems

An open quantum system is one that interacts with its external surroundings. The dynamics of such a system is no longer coherent and *cannot* be described by the usual Schrödinger equation,

$$i\hbar \frac{d}{dt} |\psi(t)\rangle = H |\psi(t)\rangle. \quad (1.1)$$

Moreover, these systems are in general not in pure states $|\psi(t)\rangle$ calling for the need to describe them in terms of density operators or density matrices,

$$\rho = \sum_i p_i |\psi_i\rangle \langle \psi_i|, \quad (1.2)$$

where, p_i is the probability of finding the system in a pure state $|\psi_i\rangle$. The density matrix is a general alternative formalism to describing a quantum system by a state vector, and can be used to directly extract useful quantities such as the expectation value of an operator, purity of the state etc.

In the following, we learn how one describes an open quantum system by first treating it as part of a larger closed system and then using the concepts of composite systems and partial trace in order to study the properties of the system we are actually interested in.

1.1 Closed systems and coherent dynamics

In the interest of mixed states, it is useful for us to write the Schrödinger equation in terms of the density matrix. This equation is now called the

Liouville-von Neumann equation and reads as,

$$\frac{d}{dt}\rho(t) = -\frac{i}{\hbar}[H, \rho(t)], \quad (1.3)$$

where, the notation $[A, B] = AB - BA$ represents the commutator of the operators A and B .

If the Hamiltonian of interest H is independent in time t , we can integrate the Liouville-von Neumann equation to obtain

$$\begin{aligned} \rho(t) &= \exp(\mathcal{L}t)\rho(0) \\ &\equiv \mathcal{V}(t)\rho(0) \end{aligned} \quad (1.4)$$

where $\mathcal{L}\rho = -i/\hbar[H, \rho]$ is called the Liouville superoperator and it maps the density operator $\rho(t)$ to its time derivative. \mathcal{V} is another superoperator also called the dynamical map since it maps the density matrix at initial time $t = 0$ to its form at time t .

One can relate this dynamical map \mathcal{V} to the unitary time evolution operator $U(t) = \exp(-iHt/\hbar)$ via,

$$\mathcal{V}(t)\rho(0) = U(t)\rho(0)U^\dagger(t) \quad (1.5)$$

1.2 Combined evolution of system and bath

We first start by considering an open quantum system as part of a larger closed system that undergoes the normal unitary evolution. The Hilbert space of such a composite system is given by the tensor product of the Hilbert spaces of the individual subsystems $\mathcal{H} = \mathcal{H}_S \otimes \mathcal{H}_B$, where the subscripts S and B denote system and bath, respectively.

Now, the total dynamics of the $(S + B)$ combination is fully coherent and given by,

$$\rho(t) = U_{SB}\rho(0)U_{SB}^\dagger \quad (1.6)$$

where U_{SB} is the unitary time-evolution operator of the total system with $U_{SB} = \exp(-iH_{tot}t/\hbar)$. Here, H_{tot} is the Hamiltonian of the total system given by,

$$H_{tot} = H_S + H_B + H_{int}, \quad (1.7)$$

where H_S and H_B are the Hamiltonians of the system and the bath respectively, and, H_{int} captures the interaction between S and B . See figure 1.1 for a diagrammatic representation. Since we are interested in the dynamics of only the system, we need to perform a partial trace over the bath B .

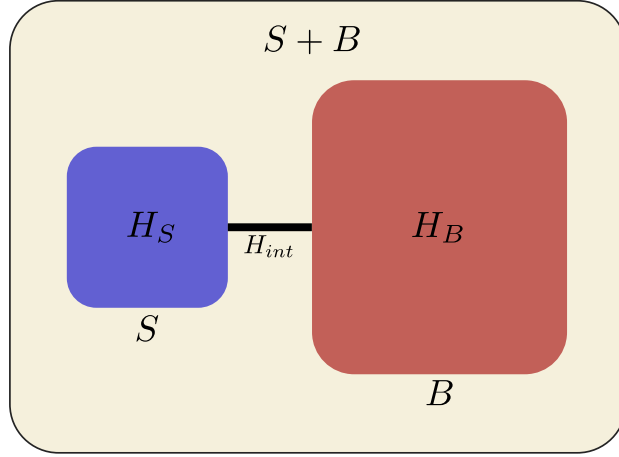


Figure 1.1: Diagrammatic representation of an open quantum system.

Partial trace:

Given a composite system $(A + B)$, the Hilbert space of which contains the individual Hilbert spaces of the subsystems \mathcal{H}_A and \mathcal{H}_B , the partial trace over one of the subsystems (say B) is a linear map $\text{Tr}_B : G(\mathcal{H}) \rightarrow G(\mathcal{H}_A)$ where $G(\mathcal{H})$ is the space of all operators acting on the Hilbert space \mathcal{H} . It is defined by,

$$\text{Tr}_B\{A \otimes B\} = A\text{Tr}\{B\} \quad (1.8)$$

where, A and B are operators on Hilbert spaces \mathcal{H}_A and \mathcal{H}_B respectively [2].

When applied to a density matrix ρ_{AB} we get

$$\begin{aligned} \text{Tr}_B\{\rho_{AB}\} &= \text{Tr}_B \left\{ \sum_{ijkl} c_{ijkl} |a_i\rangle\langle a_j| \otimes |b_k\rangle\langle b_l| \right\} \\ &= \sum_{ijkl} c_{ijkl} |a_i\rangle\langle a_j| \langle b_l|b_k\rangle \\ &= \sum_{ijk} c_{ijkk} |a_i\rangle\langle a_j| \end{aligned} \quad (1.9)$$

where $\{|a_i\rangle\}$ and $\{|b_i\rangle\}$ form sets of complete orthonormal basis of \mathcal{H}_A and \mathcal{H}_B , respectively, with $c_{ijkl} = \langle a_i b_k | \rho_{AB} | a_j b_l \rangle$.

1.3 The quantum master equation

In this section, we follow a series of assumptions, that in most of the typical situations are true, in order to derive the quantum master equation in its Lindblad form. Note that the discussion here largely follows the reference [1].

1.3.1 Quantum dynamical semigroups

We have already started in the previous section by considering the open system as part of a larger closed system. Since we are only interested in just the open system, we can now apply the partial trace operation 1.9 to Eq. 1.6,

$$\begin{aligned}\rho_S(t) &= \text{Tr}_B\{\rho(t)\} \\ &= \text{Tr}_B\{U_{SB}\rho(0)U_{SB}^\dagger\} \\ &= \text{Tr}_B\{U_{SB}(\rho_S(0) \otimes \rho_B(0))U_{SB}^\dagger\}\end{aligned}\quad (1.10)$$

The last step here is obtained by our first assumption of separability, meaning that we can prepare the initial state of the system ($S+B$) in an uncorrelated product state of the form $\rho(0) = \rho_S(0) \otimes \rho_B(0)$ where ρ_S is the initial state of the system of interest S and ρ_B is some reference state of the environment. For the next step, we do the following:

- i) we may think of the right hand side of Eq. 1.10, as the superoperator $\mathcal{V}(t)$ representing a dynamical map from the space $S(\mathcal{H}_S)$ onto itself that describes the state change of *only the open system* S over time t .
- ii) we use the spectral decomposition of the density matrix of the environment ρ_B ,

$$\rho_B(0) = \sum_{\alpha} \lambda_{\alpha} |\phi_{\alpha}\rangle\langle\phi_{\alpha}|, \quad (1.11)$$

where $\{|\phi_{\alpha}\rangle\}$ form an orthonormal basis in \mathcal{H}_B with $\lambda_{\alpha} \geq 0$ satisfying the condition $\sum_{\alpha} \lambda_{\alpha} = 1$.

Plugging these two in Eq. 1.10, we get

$$\mathcal{V}(t)\rho_S(0) = \sum_{\alpha\beta} W_{\alpha\beta}(t)\rho_S(0)W_{\alpha\beta}^\dagger(t), \quad (1.12)$$

where $W_{\alpha\beta}(t) = \sqrt{\lambda_{\beta}}\langle\phi_{\alpha}|U_{SB}(t)|\phi_{\beta}\rangle$ are operators acting in \mathcal{H}_S .

Since these operators satisfy the condition $\sum_{\alpha\beta} W_{\alpha\beta}(t)W_{\alpha\beta}^\dagger(t) = I_S$, we get the relation $\text{Tr}\{\mathcal{V}(t)\rho_S(0)\} = \text{Tr}\{\rho_S\} = 1$. This means that the dynamical map \mathcal{V} is trace preserving.

1.3 The quantum master equation

Next, we consider the family of all the dynamical maps $\{\mathcal{V}(t)|t \geq 0\}$ with $\mathcal{V}(0)$ as its identity. This family now describes the entire time evolution of the open system. However, since this could be very involved we turn to an approximation, called the *Markov approximation*. The main idea here is that, if the typical correlation time of the fluctuations is much smaller than the shortest time scale of the system dynamics ($\tau_S \gg \tau_B$), we can neglect the memory of the reservoir, and treat the system as Markovian. This is indeed the case in most of the systems we deal with experimentally. As a consequence of this, the dynamical map now satisfies the semigroup property,

$$\mathcal{V}(t_1 + t_2) = \mathcal{V}(t_1)\mathcal{V}(t_2) \quad t_1, t_2 \geq 0. \quad (1.13)$$

and therefore represents a quantum dynamical semigroup. It is a semigroup because of the constraint on the times being positive, allowing us to propagate only forward in time, meaning that the inverse of the map does not normally exist. This is in contrast to the case of coherent evolution where the dynamical map always also contains inverse operations corresponding to negative times and therefore forming a group.

1.3.2 Markovian quantum master equation

Given a dynamical semigroup, we can write down its generator \mathcal{L} which is a linear map that allows us to represent it in an exponential form,

$$\mathcal{V}(t) = \exp(\mathcal{L}(t)). \quad (1.14)$$

Expanding this map for short times τ , which in the limit $\tau \rightarrow 0$, leads us to a first-order differential equation for the density matrix of the system S ,

$$\frac{d}{dt}\rho_S(t) = \mathcal{L}\rho_S(t). \quad (1.15)$$

This equation is called the Markovian quantum master equation and the generator \mathcal{L} of the semigroup may be understood as the generalization of the Liouville superoperator introduced in section 1.1 but now also including additional incoherent terms.

1.3.3 Lindblad formalism

In the following, we derive an expression for the generator \mathcal{L} to arrive at the most general form of the Markovian quantum master equation.

We consider a finite-dimensional Hilbert space \mathcal{H}_S with dimensionality N . The corresponding Liouville space, the complex vector space of operators, has

a dimension of N^2 , and in this space, we can write down the complete basis of orthonormal operators F_i , where $i = 1, 2, \dots, N^2$ with their inner product defined such that

$$\langle F_i, F_j \rangle = \text{Tr}_S \{ F_i^\dagger F_j \} = \delta_{ij}. \quad (1.16)$$

We choose the operator $F_{N^2} = I_S / \sqrt{N}$ to be proportional to the identity for convenience, so that the other operators are traceless. We can now write the dynamical map in the basis of these operators as,

$$\mathcal{V}(t)\rho_S = \sum_{i=1}^{N^2} c_{ij}(t) F_i \rho_S F_j^\dagger, \quad (1.17)$$

where the coefficients c_{ij} are given by,

$$c_{ij}(t) \equiv \sum_{\alpha\beta} \langle F_i, W_{\alpha\beta}(t) \rangle \langle F_j, W_{\alpha\beta}(t) \rangle^*. \quad (1.18)$$

Note that the coefficient matrix $c = [c_{ij}]$ is Hermitian and positive. If we now insert Eq. 1.17 into Eq. 1.15 we get,

$$\mathcal{L}\rho_S = \lim_{\epsilon \rightarrow 0} \frac{1}{\epsilon} \{ \mathcal{V}(\epsilon)\rho_S - \rho_S \} \quad (1.19)$$

Next, we define the coefficients as $a_{ij} = \lim_{\epsilon \rightarrow 0} \frac{c_{ij}}{\epsilon}$, and introduce the quantities,

$$F = \frac{1}{\sqrt{N}} \sum_{i=1}^{N^2-1} F_i \quad (1.20)$$

$$G = \frac{1}{2N} a_{N^2 N^2} I_S + \frac{1}{2} (F^\dagger + F) \quad (1.21)$$

$$H = \frac{1}{2i} (F^\dagger - F). \quad (1.22)$$

Inserting these definitions in Eq. 1.17, we now get the *first standard form* for the generator,

$$\mathcal{L}\rho_S = -i [H, \rho_S] + \sum_{i,j=1}^{N^2-1} a_{ij} \left(F_i \rho_S F_j^\dagger - \frac{1}{2} \{ F_j^\dagger F_i, \rho_S \} \right) \quad (1.23)$$

Since the coefficient matrix $a = [a_{ij}]$ is positive, it can be diagonalized with an appropriate unitary transformation uau^\dagger in order to get the *diagonal* form of the generator as,

$$\mathcal{L}\rho_S = -i [H, \rho_S] + \sum_{k=1}^{N^2-1} \gamma_k \left(A_k \rho_S A_k^\dagger - \frac{1}{2} \{ A_k^\dagger A_k, \rho_S \} \right) \quad (1.24)$$

Here, the operators A_k , are called *Lindblad operators* (or *jump operators in Lindblad form*) and are appropriate linear combinations of the basis operators F_i . The corresponding density matrix equation 1.15 is called the *Lindblad equation*. Moreover, the corresponding γ_k are non-negative eigenvalues of the coefficient matrix $[a_{ij}]$, and play the role of relaxation rates for the different decay processes of the open quantum system.

1.4 Wave function Quantum Monte Carlo simulation

To calculate the time evolution of a quantum many-body system, one typically needs to solve as many equations as the dimensions of the Hilbert space, which grows exponentially with the system size, making it extremely difficult, if not impossible, to solve systems with large number of particles. In order to tackle this problem, several sophisticated methods were developed. Reference [25] offers a review of most of these techniques that can be broadly classified into stochastic, tensor network simulations or variational approach.

Here, we will focus on the Monte Carlo wave-function (MCWF) method [26, 27] that is stochastic in its nature. With this technique, we can avoid the direct propagation of the full density matrix in time. Instead, the strategy is to propagate individual pure states ψ_i in time, and then take a stochastic average in order to calculate an observable O as,

$$\langle O \rangle = \sum_i p_i \langle \psi_i | O | \psi_i \rangle. \quad (1.25)$$

We are able to do this because we can write the density matrix at an initial time as a statistical ensemble of pure states using Eq. 1.2. Each of these individual states ψ_i , also called the *trajectories*, are independent of each other. Therefore, the statistical error associated with the observable scales as $\Delta O \sim 1/\sqrt{N_{traj}}$.

Let us study, in detail, how to propagate the individual pure states ψ_i . The idea is to evolve the wave function with a modified Hamiltonian and a series of randomly decided so-called quantum jumps, sudden changes that occur at certain times. Therefore, this method can also be called the *quantum-jump approach* [28].

In general, the wave function of the total system $\psi(t)$ evolves according to the Schrödinger Eq. 1.1 with an effective *non-Hermitian* Hamiltonian,

$$H_{eff} = H_S - \frac{i\hbar}{2} \sum_n c_n^\dagger c_n, \quad (1.26)$$

where c_n are the jump operators, or also called the collapse operators, for each of the irreversible processes that occur with rates γ_n respectively.

Since the non-Hermitian part of the effective Hamiltonian is strictly negative, this results in the reduction of the norm of the wave function, which to first-order in small time δt is given by

$$\langle \psi(t + \delta t) | \psi(t + \delta t) \rangle = 1 - \delta p \quad (1.27)$$

where δp is the probability of the occurrence of a quantum jump and is given by,

$$\delta p = \delta t \sum_n \langle \psi(t) | c_n^\dagger c_n | \psi(t) \rangle. \quad (1.28)$$

In case a quantum-jump does occur at time t , then the wave function of the system undergoes a jump to a state $|\psi(t + \delta t)\rangle$ that is defined by projecting $|\psi(t)\rangle$ using the collapse operator corresponding to the quantum jump by,

$$|\psi(t + \delta t)\rangle = \frac{1}{\langle \psi(t) | c_n^\dagger c_n | \psi(t) \rangle^{1/2}} c_n |\psi(t)\rangle \quad (1.29)$$

This treatment is equivalent to the master-equation treatment [27], but the advantage here is that the number of variables involved scale rather linearly with the Hilbert space compared to the quadratic scaling for full density matrix calculations.

For the simulations shown in this thesis, we use the above discussed MCWF implemented in QuTiP [29], which is an open-source framework, designed to simulate mostly open quantum dynamics, written in the Python programming language. In certain cases, where required, we also extend this to a heavily parallelized version for better performance.

The algorithm used here for the implementation is slightly different than the one described above. Instead of evaluating the evolution to first-order in time, the steps are as follows:

Starting from a pure state $|\psi(0)\rangle$,

i) We choose a random number r between 0 and 1, that represents the probability for a quantum jump to occur.

ii) Evolve the state in time using the effective Hamiltonian Eq. 1.26 until a time τ satisfying $\langle \psi(\tau) | \psi(\tau) \rangle = r$, at which point a quantum jump occurs.

iii) The system is then projected into one of the states given by the corresponding collapse operator c_n that is chosen such that n is the smallest integer satisfying the relation $\sum_{i=1}^N \geq r$.

iv) We now use the new state obtained as the initial state, draw a new random number r and repeat the steps until the final simulation time is reached.

1.5 Examples of dissipative processes

	Local	Collective
Emission	$c_i = \sigma_-^i$	$c = \sum_i \sigma_-^i$
Pumping	$c_i = \sigma_+^i$	$c = \sum_i \sigma_+^i$
Dephasing	$c_i = \sigma_z^i$	$c = \sum_i \sigma_z^i$

Table 1.1: A summary of the various dissipative processes that can occur in an open quantum system and the corresponding jump operators that are used to describe them for two-level systems.

1.5 Examples of dissipative processes

Controlled dissipation being the main tool used in the work in this thesis, it is useful to have a list of all the dissipative processes that can occur in an open system. These processes can be broadly classified using two classification schemes:

- (i) depending on which part of the system the dissipative processes act they can be either local or global, and,
- (ii) depending on the kind of the processes, they are called emission, pumping or dephasing.

Local emission processes usually describe radiative or non-radiative losses from the system, and the collective counterpart typically describes superradiant decay [30]. Dissipative pumping processes on the other hand describe incoherently raise (or *pump*) the system to an excited state and dephasing describes the decay of coherence in the system over passing time.

Table 1.1 summarizes these processes and the corresponding Lindblad operators used to describe them for two-level systems that are relevant to this thesis.

Additionally, there are several other kinds of dissipative processes. E.g. in field of quantum information, one describes channels via which a qubit undergoes a decoherence process resulting in an *error* [31]. The error can result in a *bit flip* ($|0\rangle \rightarrow |1\rangle, |1\rangle \rightarrow |0\rangle$), *phase flip* ($|0\rangle \rightarrow |0\rangle, |1\rangle \rightarrow -|1\rangle$), or both ($|0\rangle \rightarrow i|1\rangle, |1\rangle \rightarrow -i|0\rangle$). The processes can be modeled by the Pauli matrices σ_x , σ_z , and σ_y , respectively.

Chapter 2

Theory of phase transitions

The basic concept of phase transition is familiar to us from our daily life experiences, such as water boiling into vapor on the gas stove and freezing into ice inside the freezer, or the melting of an ice candy on a hot day, or the formation of dew drops on a cold morning. We understand that these events, where matter changes from one state to another, occur as the result of a change in certain external quantities, such as the temperature, or the pressure. We also know that the different states of matter have their characteristic properties, e.g., solids are rigid, liquids can flow, whereas gases occupy the entire space available to them. When a system goes from one phase to another, we say that the system has undergone a *phase transition*.

The theory of phase transitions, however, is much richer than the simple solid-liquid-gas transitions, and the difference in properties of the different states of matter, or in general, the thermodynamic phases of a system is very subtle. It is often the case that one of the phases is more *ordered* than the others, e.g., all the atoms in a crystal are arranged in a regular fashion but one cannot say such a thing for the liquid phase. This allows us to describe the properties of the different phases of the system using a quantity called the *order parameter*. This parameter basically quantifies the amount of order present in the state of the system [32]. A closely related concept to describe phase transitions is based on the idea of symmetry breaking, especially the process of spontaneous symmetry breaking. This process typically describes systems where the ground state does not respect the symmetry of the Hamiltonian of the system. Usually, the disordered phase of the system is invariant under certain symmetry transformations, whereas the ordered phase does not respect this symmetry. Therefore, as the system undergoes a phase transition from the disordered phase to the ordered phase, it is accompanied by such a symmetry breaking process.

From a fundamental point of view, phase transitions are very interesting as they provide a perfect example of how rather simple dynamics at the microscopic level can result in a highly complex behavior at the macroscopic scale. Furthermore, the tools and methods developed to study them have found applications not just in physics but also other fields such as chemistry, biology and even economics.

On the other hand, phase transitions play an important role in many technological applications, because certain phases of matter have crucial properties that make them promising candidates for these innovations. For example, liquid crystals that are used in display devices change their transparency when subjected to an external voltage or a change in temperature. Bose-Einstein condensates can be used as high precision accelerometers in geological pursuits to locate deep reservoirs of gas, oil and minerals. Furthermore, we show in part III, that phase transitions can also be used to sense extremely weak magnetic fields.

Building upon the strong foundation laid by Gibbs [33] for the theory of thermodynamics, there have been an enormous amount of studies that have helped us better understand these transitions, be it classical or quantum. In the following, we will briefly distinguish between the two.

2.1 Classical and quantum phase transitions

In classical systems, the interplay of the three thermodynamic variables, energy, entropy S , and temperature T is crucial to the understanding of phase transitions. There is a constant competition between the minimization of the internal energy of the system, and the maximization of its entropy. In thermal equilibrium, the final microstate of the system has an internal energy U and entropy, such that the free energy F of the system is minimal. These quantities are related to one another by the relation,

$$F = U - TS. \tag{2.1}$$

By controlling the temperature, one can drive the system to behave differently in different regimes. For example, a lower temperature would lower the contribution of the entropy to the free energy of the system, resulting in the system being in an ordered phase. However, if the thermal fluctuations are large enough to overcome the energy lost in breaking the order in the ordered phase, the system undergoes a phase transition into the disordered phase. Therefore, phase transitions occurring at a finite temperature are mostly classical in nature, typically driven by thermal fluctuations.

2.1 Classical and quantum phase transitions

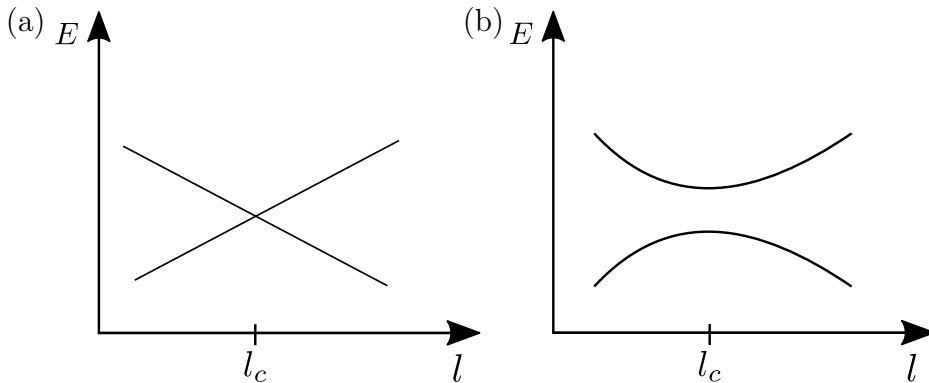


Figure 2.1: Behavior of the ground state energy of a Hamiltonian of the form $H_0 + lH_1$ as a function of dimensionless coupling l resulting in (a) level-crossing in the case where $[H_0, H_1] = 0$ and (b) avoided level-crossing where $[H_0, H_1] \neq 0$.

In quantum systems, on the other hand, at the absolute zero temperature, there are no thermal fluctuations. Phase transitions here are rather driven by the so-called quantum fluctuations that arise from the uncertainty principle [34]. We say that a phase transition has occurred in a system when its ground state behaves in a nonanalytic manner due to a small change in the coupling constants of the Hamiltonian, resulting in a macroscopic change of the properties of the ground state.

To probe further into this, let us consider the following Hamiltonian,

$$H = H_0 + lH_1. \quad (2.2)$$

We are interested in the ground state energy for varying values of the dimensionless constant l . In the case where H_0 and H_1 commute with one another, at some critical value of l , say at $l = l_c$, there may be a level-crossing where an excited state becomes the ground state as shown in figure 2.1 (a). Thus the ground state energy has a nonanalytic behavior at l_c .

However, if the two parts of the Hamiltonian do not commute such that $[H_0, H_1] \neq 0$, which is often the case, the level-crossing may be avoided, as is shown in figure 2.1 (b). In such cases, when the size of the system increases, the avoided crossing becomes increasingly sharper and at infinite size limit, the energy gap closes leading again to nonanalytic behavior of the ground state. In both these cases, we have a quantum phase transition.

Some systems also exhibit both quantum and classical phase transitions in the same phase diagram (see figure 2.2). At $T = 0$, the system undergoes a quantum phase transition at the critical point l_c , whereas on the other

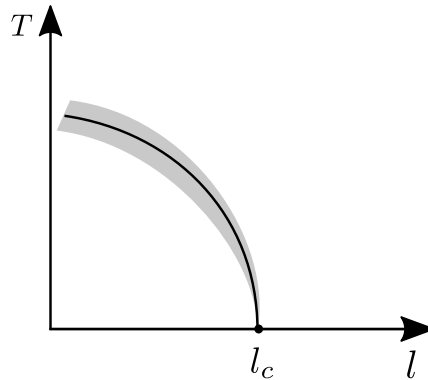


Figure 2.2: Classical and quantum phase transitions in the same phase diagram. At $T = 0$, the system undergoes a quantum phase transition at the quantum critical point l_c . At $T > 0$ there is a line of transition that terminates at l_c around which classical theory of phase transitions can be applied (shaded area).

hand, at $T > 0$ there is a line around which the classical theory of phase transitions can be applied where the system is driven by thermal fluctuations. An example for such a case is that of the Bose-Hubbard model [35] which at $T = 0$ exhibits a quantum phase transition from the superfluid phase at weak interaction regime to a Mott insulator phase at the strong interaction regime, and at $T > 0$ it exhibits a superfluid to normal liquid transition.

2.2 Classification of phase transitions

Originally, Paul Ehrenfest classified phase transitions depending upon how the thermodynamic free energy of the system behaved as a function of the various relevant thermodynamic variables $\{K_i\}$. The idea was to label them by the lowest derivative of the free energy that is discontinuous at the transition point [36]. Therefore, transitions where the first order derivative of the free energy with respect to a thermodynamic variable exhibits a discontinuous behavior, are called first-order transitions. All solid-liquid-gas transitions fall into this category as they are accompanied by a discontinuous change in density, which is the inverse of the first order derivative of the free energy with respect to the pressure. In second order transitions, quantities like compressibility and specific heat, that are second order derivatives of the free energy show a jump across the transition. An example for this category is the phase transition in materials such as iron where the magnetic suscepti-

2.2 Classification of phase transitions

bility, a second order derivative of the free energy with respect to the applied magnetic field, displays a discontinuous behavior. The magnetization, on the other hand, which is the first order derivative of the free energy, is a smooth function across the phase transition.

However, this scheme of classification does not take those cases into account where a derivative of the free energy diverges, and is therefore incomplete. The modern classification, which is very similar to the original scheme, classifies phase transitions into the following two categories [37].

First order phase transition: a phase transition is said to be first-order in nature if one or more of the first order derivatives of the free energy $\partial F/\partial K_i$ is discontinuous across the phase boundary. In part III of this thesis, we will only deal with first order phase transition.

Continuous phase transition: in this kind of phase transitions, all the first order derivatives $\partial F/\partial K_i$ are continuous across the phase boundary. However, it is most often (not necessarily always) the case that one or more of the second order derivatives $\partial^2 F/\partial K_i^2$ is discontinuous across the transition. These transitions are also sometimes called second order phase transitions.

An interesting case worth mentioning, is when the free energy is non-analytic but all its derivatives are continuous. The famous example for such a transition is the Berezinsky-Kosterlitz-Thouless [38, 39] (BKT) transition in two-dimensional systems. In such transitions, the correlation functions decay exponentially in one phase and algebraically in the other. Here, the free energy of the system is non-analytic but all its derivatives are continuous, therefore, these transitions are said to be *infinite-order transitions*.

Close to the critical point of a continuous phase transition, the system becomes scale invariant, meaning that the microscopic details are no longer relevant and the macroscopic behavior of the system has universal properties that are rather determined by long-range physics. This gives rise to the concept of universality where two completely different systems in terms of microscopic properties have the same so-called *critical exponent* that describes their behavior at the macroscopic level. A prominent example of this is that the scaling of the temperature in the case of change in density for the liquid-gas transition and in the case of magnetization of an Ising ferromagnet is non-trivially the same [32]. This feature is particularly powerful as once we establish a universality class for a given system, we immediately know its thermodynamic properties even without knowing all of the microscopic details.

So far, we have only mentioned scenarios where the properties of the ground state of the system undergoing a phase transition are considered. Alternatively, one could also consider the properties of a steady state of the system. This is especially important in driven-dissipative quantum systems

that evolve into non-equilibrium steady states, also shortly called NESS. Criticalities in these systems are defined via non-analyticities in the behavior of the steady state ρ_{ss} of the system while varying the relevant control parameters. Although these systems are out of equilibrium, the classification scheme mentioned above can still be applied to them since one can find the relevant free-energy functional that has a discontinuous jump across the phase transition [40]. Steady state phase transition is particularly relevant to part III of this thesis where we study first order transition in the magnetization of our system.

2.3 Spin models

Spin models serve as great paradigmatic models for the theoretical understanding of phase transitions. Since here, in this thesis, we mostly deal with spin-1/2 models it is useful to study some of these models in the following section and describe their properties.

2.3.1 Ising model

The Ising model is one of the spin models with fascinating properties that has significantly improved our understanding in the field of statistical physics, especially the concept of phase transitions.

The one-dimensional spin-1/2 quantum Ising model is defined by the Hamiltonian,

$$H = -g \sum_i \sigma_x^{(i)} - J \sum_i \sigma_z^{(i)} \otimes \sigma_z^{(i+1)}, \quad (2.3)$$

where, g is the strength of the transverse field, and, J is the strength of the interaction between the two nearest neighbour spins. The Pauli matrices $\sigma_{x,y,z}$ at each site i represent the quantum degrees of freedom and take the well known form

$$\sigma_x = \begin{pmatrix} 0 & 1 \\ 1 & 0 \end{pmatrix}; \quad \sigma_y = \begin{pmatrix} 0 & -i \\ i & 0 \end{pmatrix}; \quad \sigma_z = \begin{pmatrix} 1 & 0 \\ 0 & -1 \end{pmatrix} \quad (2.4)$$

Depending on the boundary condition, the ends of the chain may be treated as:

- (i) free ends, where $1 \leq i \leq N$ for the transverse field term and $1 \leq i \leq N-1$ for the interaction term, or,
- (ii) a cyclic chain, where $1 \leq i \leq N$ and $\sigma_z^{(N+1)} = \sigma_z^{(1)}$.

We will denote the eigenstates of the σ_z Pauli matrix as $|\uparrow\rangle$ and $|\downarrow\rangle$ that have eigenvalues ± 1 and either be oriented up or down. Consequently, these

2.3 Spin models

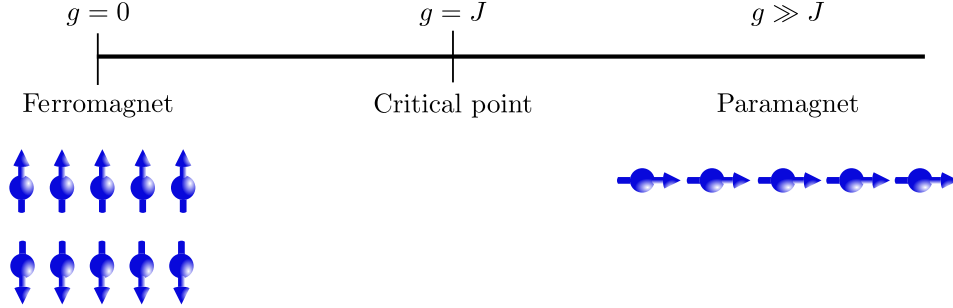


Figure 2.3: One dimensional quantum Ising model in a transverse field undergoes a phase transition from a ferromagnet ($g = 0$) to a paramagnet ($g \gg J$) via the critical point at $g = J$.

are related to the eigenstates of the σ_x Pauli matrix by

$$\begin{aligned} |\rightarrow\rangle &= (|\uparrow\rangle + |\downarrow\rangle)/\sqrt{2} \\ |\leftarrow\rangle &= (|\uparrow\rangle - |\downarrow\rangle)/\sqrt{2} \end{aligned} \quad (2.5)$$

Since the symmetry properties of the Hamiltonian will play a crucial role in determining the different phases under the transition, let us study them. We see that the Ising Hamiltonian (Eq. 2.3) is invariant under the global Z_2 transformation

$$\sigma_z^i \rightarrow -\sigma_z^i; \quad \sigma_x^i \rightarrow \sigma_x^i \quad (2.6)$$

Let us now consider the scenario where the transverse field is much stronger than the Ising interaction ($g \gg J$). In this case all the spins would align themselves along the x-axis and the ground state is a *quantum paramagnet* given by

$$|0\rangle = \prod_i |\rightarrow\rangle_i \quad (2.7)$$

On the other side of the limit where $g \ll J$, at $g = 0$, the spins would all point either up or down with the ground state being a *ferromagnet* given by

$$|0\rangle = \prod_i |\uparrow\rangle_i \quad \text{or} \quad |0\rangle = \prod_i |\downarrow\rangle_i \quad (2.8)$$

Crucially, we see that these two ground states are not invariant under the Z_2 transformation, but rather map to each other. At the critical point of $g = J$, there exists a quantum phase transition (see figure 2.3) from the ordered phase (quantum ferromagnet) to the disordered phase (paramagnet).

The exact solution:

Let us now study the exact spectrum of this model. For this, we will use the Jordan-Wigner transformation which is a map between the Hilbert space of a system of spin-1/2 particles and that of spinless fermions which hop between sites with single orbitals. The spin-up state of the spin system may be associated with an empty orbital of the fermionic system and the spin-down state with an occupied orbital which immediately leads to

$$\sigma_z^{(i)} = 1 - 2c_i^\dagger c_i, \quad (2.9)$$

where the canonical fermion operators c_i and c_i^\dagger annihilate and create a fermion at site i respectively.

This transformation is named after Jordan and Wigner who modified the single site operator to a string of operators in order to incorporate the anticommutation property of the fermions,

$$\begin{aligned} \sigma_+^{(i)} &= \prod_{j<i} (1 - 2c_j^\dagger c_j) c_j \\ \sigma_-^{(i)} &= \prod_{j<i} (1 - 2c_j^\dagger c_j) c_j^\dagger. \end{aligned} \quad (2.10)$$

The inverse mapping is then given by,

$$\begin{aligned} c_i &= \left(\prod_{j<i} \sigma_z^{(j)} \right) \sigma_+^{(i)} \\ c_i^\dagger &= \left(\prod_{j<i} \sigma_z^{(j)} \right) \sigma_-^{(i)}. \end{aligned} \quad (2.11)$$

For our analysis of the Ising model, it is convenient to rotate the spin axes about the y axis by 90 degrees such that

$$\sigma_z \rightarrow \sigma_x, \quad \sigma_x \rightarrow -\sigma_z. \quad (2.12)$$

Under this convention, the mapping becomes,

$$\begin{aligned} \sigma_x &= 1 - 2c_i^\dagger c_i \\ \sigma_z &= - \prod_{i<j} (1 - 2c_j^\dagger c_j) (c_i + c_i^\dagger). \end{aligned} \quad (2.13)$$

We can now write the Hamiltonian using the fermionic operators, for the case of open boundaries as,

$$H = \sum_i^N \left(2gc_i^\dagger c_i + g \right) - \sum_i^{N-1} \left(Jc_i^\dagger c_{i+1} + Jc_{i+1}^\dagger c_i + Jc_i^\dagger c_{i+1}^\dagger + Jc_{i+1} c_i \right). \quad (2.14)$$

2.3 Spin models

For the cyclic chain, we also have additional terms and the Hamiltonian reads,

$$H = \sum_i^N \left(2gc_i^\dagger c_i + g \right) - \sum_i^N \left(Jc_i^\dagger c_{i+1} + Jc_{i+1}^\dagger c_i + Jc_i^\dagger c_{i+1}^\dagger + Jc_{i+1} c_i \right) + \left(Jc_N^\dagger c_1 + Jc_1^\dagger c_N + Jc_1^\dagger c_1^\dagger + Jc_N c_1 \right) (\exp(i\pi L) + 1) \quad (2.15)$$

where, $L = \sum_{j=1}^N c_j^\dagger c_j$. We will neglect the last correction term as in references [41, 42] to turn this so-called a-cyclic problem into the simpler c-cyclic problem.

Next, we diagonalize the Hamiltonian for which we first use the momentum eigenstates given by,

$$c_k = \frac{1}{\sqrt{N}} \sum_j c_j e^{-ikr_j}, \quad (2.16)$$

with $k = 2\pi m/N$, where,

$$m = \begin{cases} -\frac{N}{2}, \dots, 0, \dots, \frac{N}{2} - 1 & \text{for } N \text{ even} \\ -\frac{N-1}{2}, \dots, 0, \dots, \frac{N-1}{2} & \text{for } N \text{ odd.} \end{cases}$$

Then, we use the Bogoliubov transformation to map to new Fermionic operators a_k, a_k^\dagger that are related to c_k, c_k^\dagger by,

$$a_k = u_k c_k - i v_k c_{-k}^\dagger, \quad (2.17)$$

where, u_k and v_k are real numbers such that $u_k^2 + v_k^2 = 1$, $u_{-k} = -u_k$, and $v_{-k} = -v_k$. The diagonalized Hamiltonian finally reads,

$$H = \sum_k \varepsilon_k (a_k^\dagger a_k - 1/2). \quad (2.18)$$

Here, ε_k is the single particle energy given by,

$$\varepsilon_k = 2J\sqrt{1 + l^2 - 2l \cos k} \quad (2.19)$$

where we have defined the ratio $l = g/J$. The ground state of the Hamiltonian $|0\rangle$ has no a fermions and satisfies $a_k|0\rangle = 0$ for all k , whereas, the n -particle excited states can be created by $a_{k_1}^\dagger a_{k_2}^\dagger \dots a_{k_n}^\dagger |0\rangle$. The many-body gap of this model, i.e., the energy difference between the first excited state and the

ground state is at $k = 0$ and is equal to $2J|1 - l|$. Therefore, at $l = 1$, i.e., at the critical point, the gap vanishes.

If we now consider the ground state of our original Hamiltonian, its energy should correspond to $E_0 = \sum_k \varepsilon_k(0 - 1/2)$ since we have, $a_k^\dagger a_k = 0$ for all k . This is indeed the case as can be seen from figure 2.4 which shows the energy levels for a system of 10 spins with periodic boundary condition for various values of the ratio l . For $l \ll 1$, there are two degenerate ground states, whereas, on the $l \gg 1$ side there is only one ground state. The excited state, on the other hand, corresponds to having one fermion in the $k = 0$ mode, such that, $E_1 = \sum_{k \neq 0} \varepsilon_k(0 - 1/2) + \varepsilon_0(1 - 1/2)$ for $l \gg 1$. Note, however, that since we have neglected the last term in Eq. 2.15, we have considered only the odd parities and the fermionic ground state has no degeneracy in the ferromagnetic phase. In order to completely characterize the original spin model, one also needs to consider the a-cyclic terms.

2.3.2 Heisenberg model

In addition to the $\sigma_x \sigma_x$ interaction term of the Ising model, the Heisenberg model has spin interactions along the other two axes as well. The Hamiltonian of the Heisenberg model (without any external transverse field) reads,

$$H = \sum_{j=1}^{N-1} \sum_{i=x,y,z} J_i \sigma_i^{(j)} \otimes \sigma_i^{(j+1)}. \quad (2.20)$$

Depending on the interaction strengths J_i , it is common to name the model e.g., as XXZ model if $J_x = J_y \neq J_z$, or as XYZ model if $J_x \neq J_y \neq J_z$, and so on.

Let us consider the one-dimensional XXZ Heisenberg model with $J_x = J_y = J$, and study the different regimes of J_z .

When $J_z < -J$ this model is in the ferromagnetic Ising phase with all spins aligned along or opposite to the z -axis. Here, the ground state does not respect the discrete symmetry of the Hamiltonian which remains invariant under spin reflection $\sigma_z \rightarrow -\sigma_z$, therefore, this is the phase with a broken symmetry. The low-lying excited states in the ferromagnetic phase are called magnons and they obey the dispersion law for general spin S [43],

$$\epsilon(k) = 2JS(1 - \cos k - (J_z + 1)). \quad (2.21)$$

The excitation spectrum has a gap at $k = 0$, whereas, at $J_z = -J$, i.e., at the isotropic ferromagnetic point it becomes gapless. Additionally, at this point,

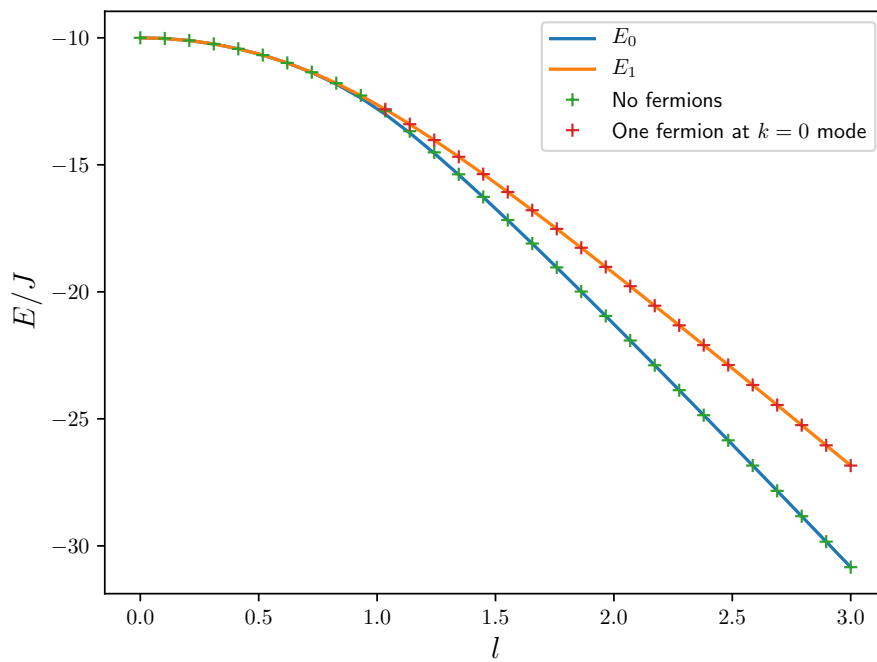


Figure 2.4: Ground state and the first excited state of the Ising model with $N = 10$ spins for various values of $l = g/J$ and the corresponding energies in the fermionic picture (plus markers). The ground state corresponds to zero fermions and the first excited state for $l > 1$ corresponds to one fermion at the $k = 0$ mode.

the discrete spin reflection symmetry generalizes to the continuous rotational symmetry.

When $-J < J_z < J$, the system is in the so-called XY phase which is characterized by uniaxial symmetry and a gapless excitation spectrum [43].

When $J_z > +J$, the model is in the antiferromagnetic phase or the Néel phase. When a spin system is antiferromagnetic, its ground state comprises of spins alternately pointing in opposite directions. Therefore, to describe such a system, one divides the lattice into two sublattices: A , which comprises of all the spins pointing, say, upwards, and B which comprises of the ones pointing downwards. Although these two sublattices are coupled to each other via the J term, spin-wave theory predicts that this coupling preserves the parity of the number of spin wave excitations. To see this, we will use the theory presented by Kubo [44]. First, we express the spin operators using the Holstein-Primakoff transformation [45],

$$\begin{aligned}\sigma_x^{(j)} + i\sigma_y^{(j)} &= [1 - a_j^\dagger a_j]^{\frac{1}{2}} a_j \\ \sigma_x^{(j)} - i\sigma_y^{(j)} &= a_j^\dagger [1 - a_j^\dagger a_j]^{\frac{1}{2}} \\ \sigma_z^{(j)} &= \frac{1}{2} - a_j^\dagger a_j\end{aligned}\quad (2.22)$$

for a spin at site j of the sublattice A , and,

$$\begin{aligned}\sigma_x^{(k)} + i\sigma_y^{(k)} &= b_k^\dagger [1 - b_k^\dagger b_k]^{\frac{1}{2}} \\ \sigma_x^{(k)} - i\sigma_y^{(k)} &= [1 - b_k^\dagger b_k]^{\frac{1}{2}} b_k \\ \sigma_z^{(k)} &= b_k^\dagger b_k - \frac{1}{2}\end{aligned}\quad (2.23)$$

for a spin at site k of the sublattice B . The bosonic creation and annihilation operators $a, a^\dagger, b, b^\dagger$ are matrices with infinite dimensions so as to satisfy the commutation rules,

$$a_j a_j^\dagger - a_j^\dagger a_j = 1, \quad b_k b_k^\dagger - b_k^\dagger b_k = 1. \quad (2.24)$$

Additionally, the operators also satisfy

$$a_j a_j^\dagger = n_j, \quad b_k b_k^\dagger = n_k \quad (2.25)$$

where $n_{j(k)}$ is the so-called spin deviation.

Introducing $f_s(n) = [1 - n]^{\frac{1}{2}}$ and inserting these in Eq. 2.20 we get,

$$\begin{aligned}H = & - \frac{NJ_z}{4} + J_z \left(\sum_j n_j + \sum_k n_k \right) - J_z \sum_{j,k} n_j n_k \\ & + \frac{J}{2} \sum_{j,k} \left[f_s(n_j) a_j f_s(n_k) b_k + a_j^\dagger f_s(n_j) b_k^\dagger f_s(n_k) \right]\end{aligned}\quad (2.26)$$

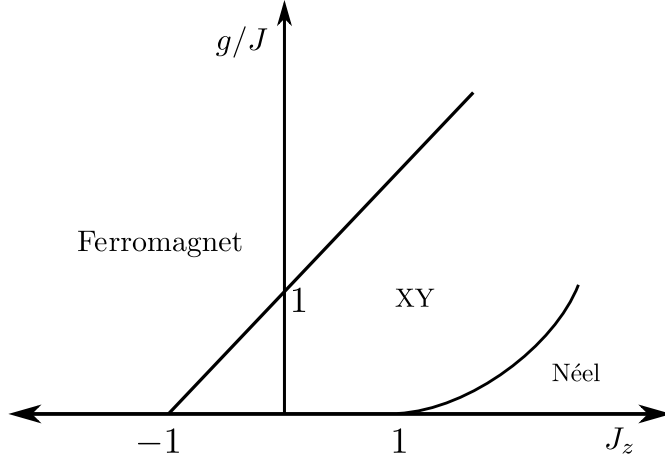


Figure 2.5: Phase diagram of the XXZ Heisenberg spin-1/2 model in a transverse field g .

To simplify this even further, we approximate $f_s(n)$ using binomial expansion and neglect higher order terms in n as explained in the reference [44]. We then obtain the Hamiltonian of the spin waves,

$$H = -\frac{NJ_z}{4} + J_z \left(\sum_j n_j + \sum_k n_k \right) + \frac{J}{2} \sum_{j,k} \left(a_j b_k + a_j^\dagger b_k^\dagger \right) \quad (2.27)$$

As we see, there are no terms of the form $a_j^\dagger b_k$ or $a_j b_k^\dagger$, in the Hamiltonian. This implies that only those interactions between the two sublattices that preserve the parity of the number of spin wave-excitations are allowed.

The most interesting regime of this model, however, is at $J_z \sim J$. When crossing this point of $J_z = J$, the system goes from a gapless XY phase to the gapped antiferromagnetic Ising phase undergoing a Kosterlitz-Thouless type of phase transition [39]. Figure 2.5 shows the phase diagram of the model in a transverse field g .

Part II

Initialization of quantum simulators by sympathetic cooling

Chapter 3

Quantum simulation

Quantum simulation is one of the most promising emergent technologies that has gained popularity in the past decades and has ever since been growing fast and expanding. It holds great potential in solving many open problems in multiple areas of physics such as atomic physics, condensed matter physics and high-energy physics [46].

The idea of quantum simulation stems from the early 1980s when Richard Feynman realized the problem of *exponential explosion* that one faces while dealing with large physical systems. This problem arises due to the fact that the state of a large system described by a number of parameters grows exponentially with the system size. Furthermore, the number of operations to be done during the time evolution of the system also grows exponentially. Although there are quite a few powerful approximation methods (for e.g. the Monte Carlo method as described in section 1.4, density functional theory [47], density matrix renormalization group [48] etc.), there are still a large class of problems that cannot be solved using these methods.

The solution to this problem was proposed by Feynman himself which, in his exact words, was "Let the computer itself be built of quantum mechanical elements which obey quantum mechanical laws." [49], and so the idea of quantum computers was born. The advantage of this over classical devices is that since they are quantum systems themselves, they can store big amounts of information and in a small amount of physical space. A system of N *qubits* can store exponentially more information than N *classical bits*.

However, to build a generic quantum computer, one needs full control over quantum many-body systems which can be a very challenging task. Firstly, there is the technical problem of preventing unwanted interactions with the surroundings during the time when calculations are made, that destroy the pure quantum state of the computer [50]. The second problem

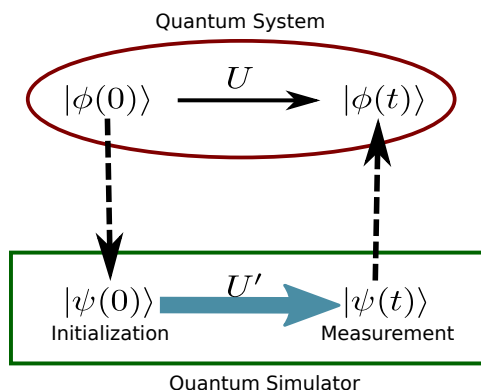


Figure 3.1: The schematic for the working of a quantum simulator as it simulates a given quantum system. The simulator is constructed such that there exists a mapping between the simulator and the system to be simulated $\phi \leftrightarrow \psi$ and $U \leftrightarrow U'$.

is that the errors arising from inaccuracies in each transformations involved get accumulated requiring error correcting codes [51, 52].

A quantum simulator on the other hand, although not universal in the true sense, lets us avoid these problems as it does not require individual addressing of all the involved components. The basic principle behind the working of a quantum simulator can be seen in figure 3.1. The first step is to find a mapping between the quantum system to be simulated and the quantum simulator. Next, we prepare the simulator in a known initial state, let the system evolve, and then measure the system at some time t . All that is remaining now is to map it back to the original quantum system and extract the relevant information.

However, it can be challenging to find algorithms or protocols for the implementation of the quantum simulator that are *efficient*, meaning, that the required resources scale only *polynomial* with the system size and not exponential.

3.1 The working of a quantum simulator

The steps involved in the successful realization of a quantum simulator are as follows (note that this discussion closely follows the review paper [46]):

i) *Initial-state preparation* - The first step towards the implementation of a quantum simulator is to prepare it in a known initial state. This is often difficult as one needs to find an efficient protocol. In this thesis, we will focus

3.2 The task of initialization

on this crucial first step.

ii) *Hamiltonian engineering* - This step mainly deals with finding the unitary transformation $U = e^{-iH_{\text{sys}}t/\hbar}$ in order to obtain the solution $|\psi(t)\rangle = U|\psi(0)\rangle$ of the Schrödinger equation for the Hamiltonian $H_{\text{sys}} = \sum H_i$ which can be written as a sum of many local interactions. This is mostly done by using some approximations (for eg. first-order Trotter formula [2]) in order to decompose the Hamiltonian into local quantum gates. This is in general the scheme for digital quantum simulation (DQS) and considerable amount of work has been done in this direction [15, 53, 54]. Analog quantum simulation (AQS), on the other hand, directly maps the Hamiltonian of the system to be simulated onto that of the simulator [55, 56, 57].

iii) *Measurement* - The last step in quantum simulation is to perform the measurement at the final time and then extract relevant information from the state. One way to characterize a state is to perform quantum state tomography [58, 59] but this method is not very efficient for large system sizes. Alternatively, one could directly estimate certain physical quantities such as the correlation functions in order to describe the final state. [60, 61].

In the following sections, after a brief overview of the different available methods for the task of preparing the quantum simulator in a known initial state, we describe our novel scheme of preparing the simulator in its ground state.

3.2 The task of initialization

As already mentioned earlier, for the successful implementation of a quantum simulator, one needs to first prepare the simulator in a known initial state $|\psi(0)\rangle$. Doing so is not always trivial as one needs to find an efficient protocol that does not grow exponentially with system size with regard to the resources it needs.

The preparation of a general pure state with N qubits has been studied and proposed by several groups in the past decades. For example, reference [62] proposes a method to prepare the antisymmetrized state of a system of N fermions starting from an unsymmetrized state using a combination of quantum gates and sorting algorithms, whereas references [60, 61] describe methods to prepare the same system in any arbitrary state starting from the vacuum state using single-qubit and two-qubit gate operations. Other systems of interest have been N -particle quantum states on lattices [63], states of chemical interest [64], or molecular systems [65].

Alternatively, one could also map the initial state to another state of

the system which behaves similarly with regards to the expectation values with the difference of just a scalar factor. Such so-called *pseudo-pure states*, however, require a high signal-to-noise measurement techniques which can limit the efficiency of the protocols [66].

Typically, however, one is rather interested in the evolution of a certain class of states, mostly the ones with low energies, and not just any arbitrary initial state. Methods to prepare a system in the ground state of the simulated Hamiltonian in the past have mostly involved preparing the system in an experimentally accessible state and then using coherent methods that use quantum logic gates or adiabatic means to prepare them in the ground state [67, 68]. However, it is impossible to realize a perfectly isolated quantum system, making these schemes extremely difficult, since inevitable decoherence processes destroy the nonclassical states.

In 2008, the idea of harnessing open system dynamics was proposed in the references [13, 14] where an interaction with a dissipative environment is appropriately engineered so that the resulting dynamics drives the system into a given pure state. The main principle behind these methods is to design this reservoir such that the steady state of the corresponding master equation is a unique dark state of the dynamics. This proposal ignited a series of dissipative state engineering techniques to cool the system into the ground state of the Hamiltonian of interest [15, 17, 69, 70]. These techniques, being themselves dissipative in nature, are typically robust against unwanted decoherence processes.

However, these methods have mostly been developed for the ground state preparation of stabilizer Hamiltonians or frustration-free models [14, 15, 71, 72, 73], i.e., Hamiltonians whose ground states can be found by performing local optimizations alone. In this thesis, we go beyond such models and give a protocol for the cooling of an arbitrary Hamiltonian. Our goal is to prepare a system in the ground state of a black-box Hamiltonian.

3.3 The initialization protocol

Having motivated the reason for the need of a novel technique for the initialization of a quantum simulator, in the following, we will present our protocol providing a motivation as to why such a dissipative protocol could actually be successful. We will then discuss some of the most prominent features of the protocol in the following chapter 4.

3.3.1 Sympathetic cooling using controlled dissipation

The schematic for the setup of the initialization protocol is shown in figure 3.3.1 which consists of a system of N spins and a single extra auxiliary spin which we also call the "bath spin" denoted by b . The system Hamiltonian H_{sys} could in general be any spin Hamiltonian. One boundary spin of the chain is then coupled to this bath spin via an interaction of the form

$$H_{int} = g_{sb} \sum_{x,y,z} f_i \sigma_i^{(N)} \sigma_i^{(b)} \quad (3.1)$$

where g_{sb} is the strength of the interaction and the quantities f_i are dimensionless parameters that are chosen in a way that would break any symmetries in the system which could otherwise prevent the cooling of some degrees of freedom. In general, it is beneficial to assign different values to them.

The next step is to add a dissipation channel to the bath spin b that would basically flip the state of the spin from up to down at a rate γ . Such a mechanism can be captured in the quantum master equation using the jump operator $\sigma_-^{(b)}$ that acts on the bath spin. Additionally, the bath spin is also driven resulting in a splitting Δ . We can now write the Hamiltonian of the bath spin as,

$$H_b = \frac{\Delta}{2} \sigma_z^{(b)} \quad (3.2)$$

The central idea here is that this driven dissipative channel acting on the bath spin would help remove the excitations in the system as shown in the schematic in figure 3.3 (a). An excitation in the system is first transferred resonantly to the bath spin via H_{int} . The excitation energy of the bath spin is emitted into its environment during the event of firing of the jump operator σ_- . This results in the relaxation of the bath spin back to its lower state (spin down state). After many such processes, eventually, the system is then cooled down to a low-energy state that is very close to the ground state of the Hamiltonian.

Although we use a one dimensional spin-1/2 system for our demonstrations here, note that this setup can be easily generalized to higher dimensions or even to other many-body systems, for example fermionic systems or bosonic systems having larger local Hilbert spaces. Besides, the setup can be implemented easily on both digital as well as analog simulators.

The problem now boils down to two questions, first, how to choose the bath spin splitting Δ , and the second, how much control can we have over the cooling dynamics by tuning the system-bath coupling strength g_{sb} and the dissipation rate γ .

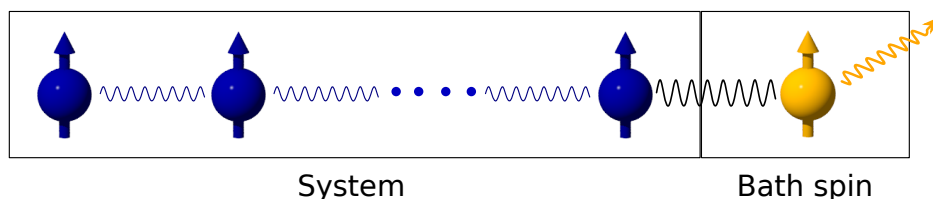


Figure 3.2: Schematic for the setup of the cooling protocol where a system of N spins is sympathetically cooled by interacting with an auxiliary spin (here termed the "bath" spin) which is driven dissipatively.

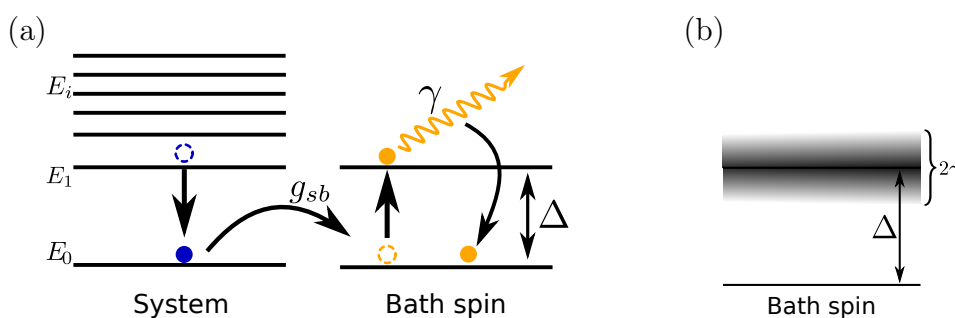


Figure 3.3: (a) Schematic for understanding the mechanism behind the cooling protocol using energy level diagrams. An excitation in the system is resonantly transferred to the auxiliary spin after which it is dissipatively pumped into its ground state. (b) Broadening of the auxiliary spin splitting Δ due to (and of the order of) the dissipation rate γ .

Let us start with the first question. The choice of this bath spin splitting Δ indeed plays an important role in the extent to which we can cool our system as this is so to say the door through which we can remove the energies from the system. As can be seen from the schematic in figure 3.3 (a), any excitation that is very high in the spectrum will always find a lower energy level that is resonant with the bath spin splitting Δ . This is because the density of states increases exponentially with the energy. This would mean that the bottleneck for the transfer of energy is rather lower down the spectrum. Therefore, for the most efficient transfer of energy from the system to the bath spin, one needs to hit the resonance condition that the bath spin splitting is equal to the many-body gap, i.e., $\Delta = \Delta E$, the difference in energy between the first excited state E_1 and the ground state E_0 .

Besides, although the bath spin splitting Δ is resonant to only a single energy, the uncertainty in the dissipation rate γ broadens this splitting which can be described by a Lorentzian function. However, for a qualitative understanding it suffices to assume that this broadening is of the order of γ (see

3.3 The initialization protocol

figure 3.3 (b)). This means that in reality, any energy that falls in the range $\Delta + \gamma$ to $\Delta - \gamma$ can be transferred from the system to the bath spin. Additionally, this even increases the number of possible pathways which an excitation could take in order to be cooled all the way down to the ground state of the system, making this protocol promisingly efficient. Figure 3.4 shows all such possible paths for a system of $N = 5$ spins having (a) Ising interaction and (b) antiferromagnetic Heisenberg interaction. The solid black lines correspond to each of the possible transitions that have an energy ranging from $\Delta \pm \gamma$. As can be seen from the drawing, there are multiple pathways to cool the system to its ground state.

With this motivation, we can now move on to performing numerical simulations that would tell us if this protocol really works. For this, we turn to the wave-function quantum Monte Carlo method as described in section 1.4. All the results shown here have been obtained by averaging over 1000 trajectories.

3.3.2 A measure of cooling

Before getting to performing the numerical simulations, we still need to define some quantities that would give us an indication of the amount of cooling that has been achieved via our protocol. In the following, we define two such useful model-independent quantities that would quantitatively suggest how close the finally prepared state is to the ground state of the system:

Ground state fidelity (f):

The simplest quantity that can tell us how close the state of a system is to its ground state, is its fidelity with respect to the ground state manifold. Such a fidelity can be calculated using,

$$f = \langle \Pi_g \rangle = \text{Tr}\{\rho(t)\Pi_g\}, \quad (3.3)$$

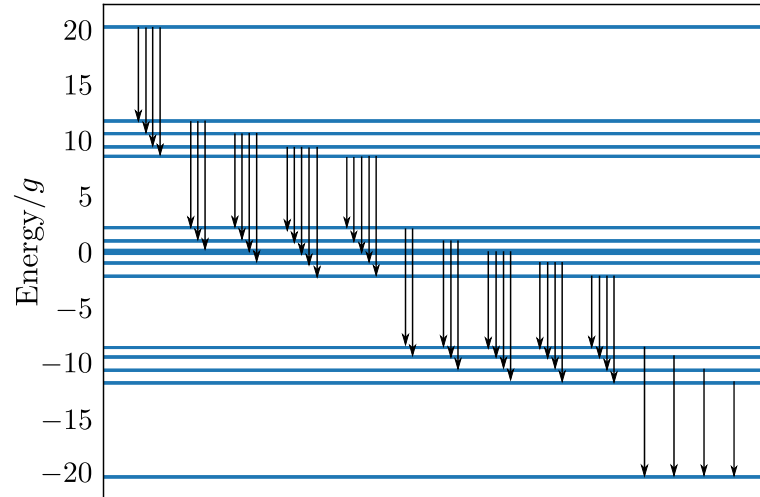
where, Π_g represents the sum of the projectors onto the ground states given by $\Pi_g = \sum_i |\psi_0^i\rangle\langle\psi_0^i|$.

Dimensionless excitation energy (ϵ):

A second quantity that is also useful in indicating the extent to which a system has been cooled is the number of excitations remaining in the system. By measuring in units of the many-body gap Δ , we can define this dimensionless quantity called the excitation energy ϵ using the following equation,

$$\epsilon = \frac{\langle H_{sys} \rangle - E_0}{\Delta E}. \quad (3.4)$$

(a)



(b)

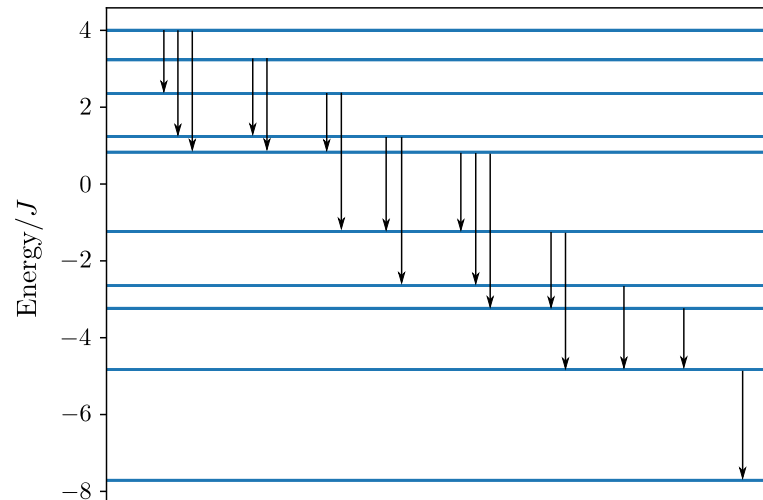


Figure 3.4: An excitation in the system can take multiple pathways in order to be cooled all the way down to the ground state. Solid black lines show all possible transitions between levels that have energy differences in the range $\Delta \pm \gamma$. The energy levels are shown here for (a) an Ising chain with $N = 5$, $J/g = 5$, $\gamma/g = 3.5$ and (b) an antiferromagnetic Heisenberg chain with $N = 5$, $\gamma/J = 1.26$.

3.3 The initialization protocol

where, E_0 is the energy of the ground state of the system.

In the limit of low-energies, i.e., $\epsilon \ll 1$, and assuming that the excitation energy is mostly concentrated in low-energy excitations, we can relate ϵ to the ground state fidelity f according to $\epsilon = 1 - f$.

3.3.3 Control parameters of the cooling dynamics

To get an insight about the cooling protocol, we now analyze exactly how the system dynamics is affected by the two main parameters of control available at our disposal, i.e., the system-bath interaction strength g_{sb} and the rate of dissipation γ .

To be explicit, we consider the transverse field Ising model (Eq. 2.3) with N spins, as our system. However, we will consider the transverse field along the z -axis so that the Hamiltonian reads,

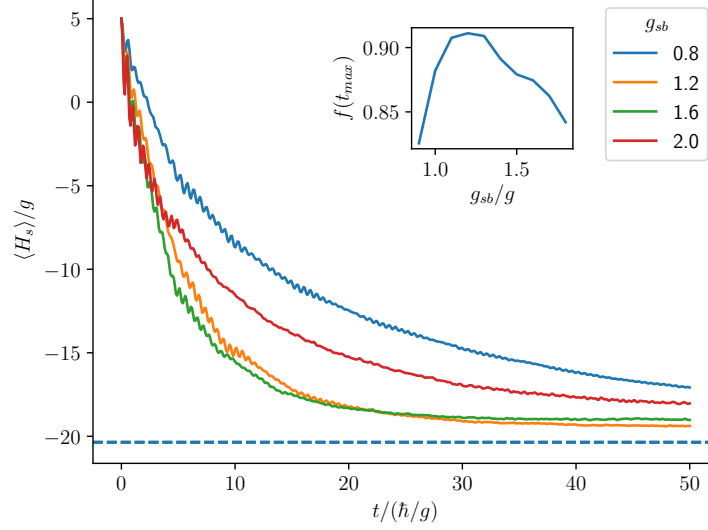
$$H = g \sum_{i=1}^N \sigma_z^{(i)} - J \sum_{i=1}^{N-1} \sigma_x^{(i)} \otimes \sigma_x^{(i+1)} \quad (3.5)$$

Let us start with the simplest case of 2 spins in the system Hamiltonian and the auxiliary bath spin. Using the effective operator formalism [74], we reduce the evolution to just the dynamics of the ground state of the bath spin. The idea is to employ perturbation theory to adiabatically eliminate the excited states of the open quantum system and derive a single effective Hamiltonian and an effective Lindblad operator for each decay process. These operators can then be immediately applied to the ground states. Applying this formalism to our system, we find that the effective rate of decay from the excited states to the ground state manifold is approximately proportional to $g_{sb}^2 \gamma$ in the limit of $g_{sb}, \gamma \rightarrow 0$. See appendix A for details.

With these first insights let us now numerically simulate a system with N spins. We check the time evolution of the expectation value of the energy of the system $\langle H_{sys} \rangle$ for different values of g_{sb} at constant γ and vice versa, first in the ferromagnetic regime. Additionally, we calculate the ground state fidelity f of the final state prepared.

Figure 3.5 shows the cooling dynamics for an Ising chain with 5 spins in the ferromagnetic phase ($J/g = 5$) with the experimentally accessible state of all spins pointing up being the initial state of the system. We see that the dynamics depends largely on (a) the strength of the system-bath interaction g_{sb} and (b) the dissipation rate γ . From the insets of both the plots, we can see that, for a given preparation time t_p , there exists an optimal regime in the values of g_{sb} and γ that results in maximum fidelity of the prepared state of the system to its ground state.

(a)



(b)

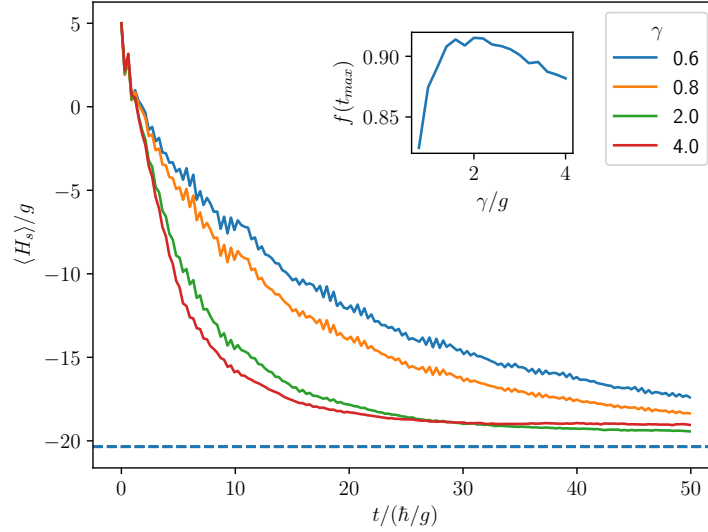
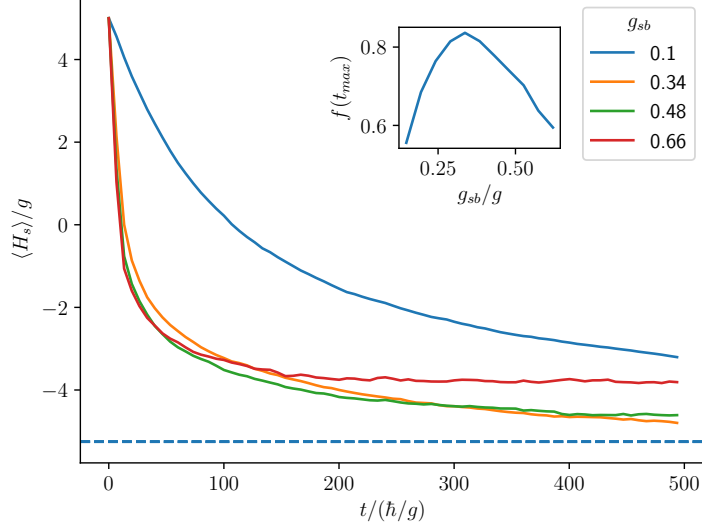


Figure 3.5: The dynamics of sympathetic cooling of the transverse field Ising chain with $N = 5$ spins in the ferromagnetic phase ($J/g = 5$). The final energy of the system, as well as, the speed of cooling depend largely on the parameters (a) g_{sb} (at fixed $\gamma/g = 1.9$), and, (b) γ (at fixed $g_{sb}/g = 1.15$). Dashed line indicates the ground state energy of the system. For a given preparation time t_p , there exist optimal values of g_{sb} and γ that result in maximum fidelity f of the prepared state to the ground state of the system (inset).

3.3 The initialization protocol

(a)



(b)

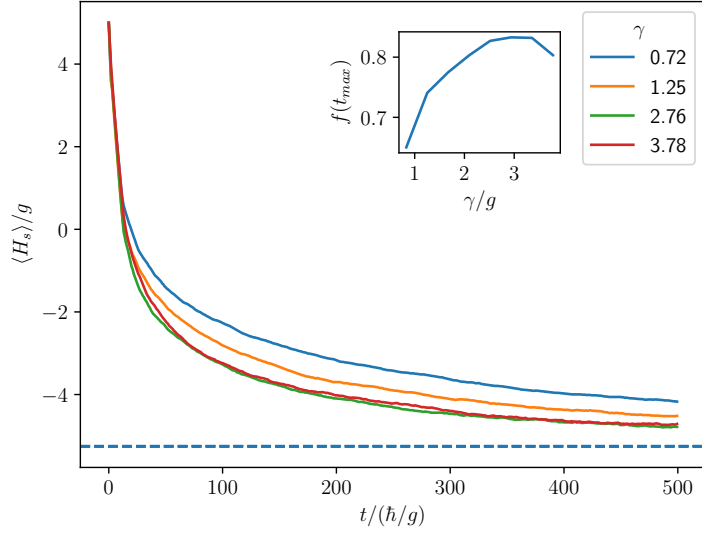
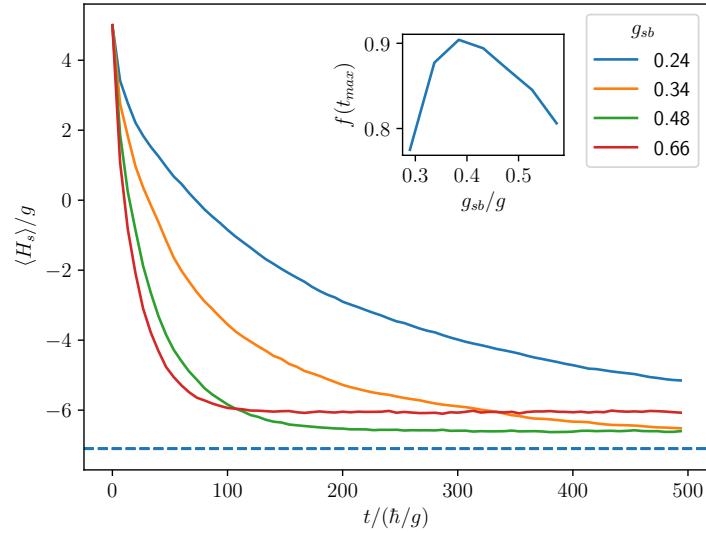


Figure 3.6: Cooling dynamics in the paramagnetic regime ($J/g = 0.2$) behaves qualitatively similar to the case of ferromagnetic phase having an optimal value for the parameters (a) g_{sb} at fixed $\gamma/g = 2.74$, and, (b) γ at fixed $g_{sb}/g = 0.35$.

(a)



(b)

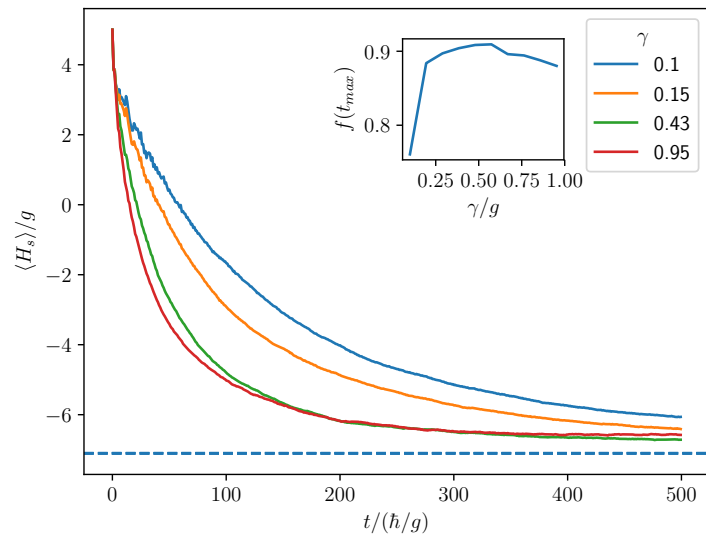


Figure 3.7: Cooling dynamics in the paramagnetic regime ($J/g = 1.4$) behaves qualitatively similar to the case of ferromagnetic phase having an optimal value for the parameters (a) g_{sb} at fixed $\gamma/g = 0.39$, and, (b) γ at fixed $g_{sb}/g = 0.39$.

3.3 The initialization protocol

These results can be explained in the following. For small values of g_{sb} and γ , it takes a very long time for the system to cool to the ground state as the cooling dynamics is very slow. Therefore, for a given time t_p , the system is not cooled down to a large extent. On the other hand, if the system-bath interaction g_{sb} is very large, the bath spin would get strongly entangled with the system. Whereas, if the dissipation rate γ is too large, it leads to the quantum Zeno suppression of the energy transfer from the system to the bath spin. In both these cases, the system is not cooled efficiently. Therefore, our parameters g_{sb} and γ need to be optimized such that it leads to maximum cooling of the system.

Next, we check if this behavior is also true in the paramagnetic regime and the critical regime. These simulation results are shown in figure 3.6 for the paramagnetic case ($J/g = 0.2$) and in figure 3.7 for the critical regime. We observe that the dependence of the cooling dynamics is qualitatively the same as in the case of ferromagnetic regime. Note, however, that the critical point for a system of $N = 5$ spins is not at $J = g$ but rather at $J/g = 1.4$ which can be determined by calculating the peak of the magnetic susceptibility as a function of J/g (see appendix B). These findings are encouraging as it shows that the cooling procedure works independently of the choice of J/g , especially, in the critical regime where the many-body gap closes making for a particularly difficult case.

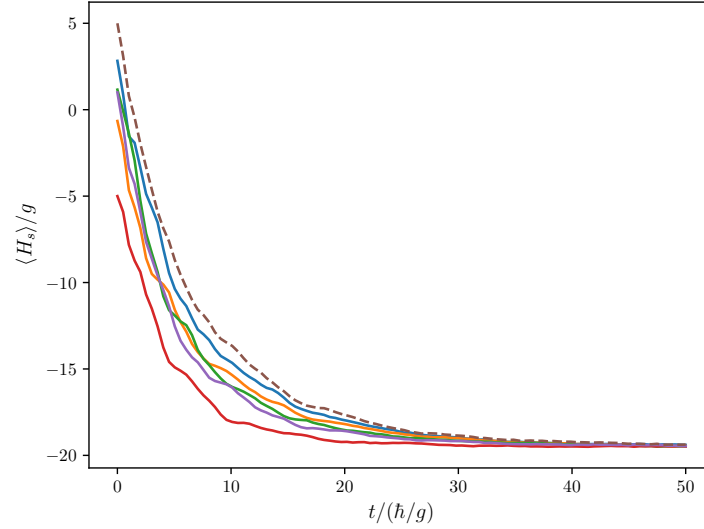
We have so far calculated the dynamics for the case where the system is initially at the state of all spins pointing up. An important question, of course, is what happens if we start in a different initial state. Therefore next, we investigate the dependence of the cooling performance on the initial state of the system. In figure 3.8 we see that although the initial energies of the system differ greatly, the overall cooling dynamics remains the same. This result is in accordance with the fact that the timescale of the dynamics is a property of the system-bath Liouvillian and does not depend on the state of the system.

3.3.4 Optimization of the control parameters

As we have seen in section 3.3.3, for a given time t , there exists a sweet spot with respect to the two control parameters g_{sb} and γ , that offers maximum cooling. Of course, if we choose these parameters to be very small, in the limit of infinite time, we can cool the system perfectly to the ground state. However, in real life scenarios one cannot wait infinitely long, as *time* is an important resource. Therefore, there is a trade-off between the amount of cooling achieved and the preparation time.

For a given preparation time t_p , we can find the optimal values of the

(a)



(b)

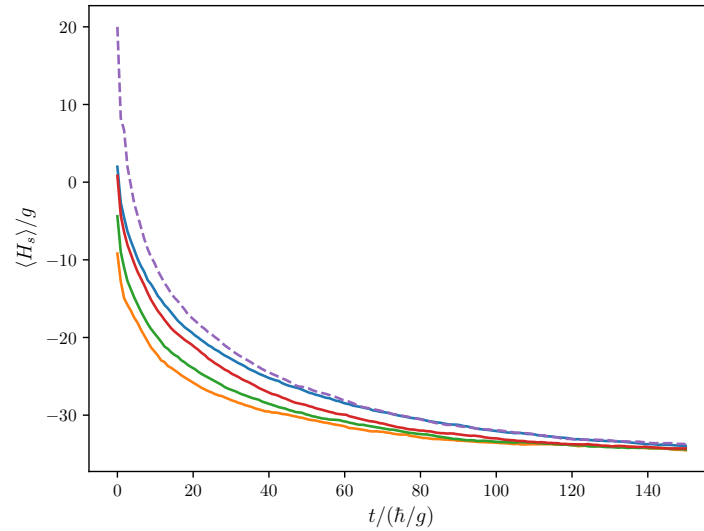


Figure 3.8: Dependence of the cooling performance on the initial state of the system. The different curves correspond to various different random initial states, chosen from a uniform distribution, for a system of 5 spins in the (a) ferromagnetic regime ($J/g = 5$) of the transverse field Ising model with $g_{sb}/g = 1.15$, $\gamma/g = 1.9$, $f_{xyz} = \{1, 1.1, 0.9\}$, and, (b) antiferromagnetic Heisenberg chain with $g_{sb}/g = 1.15$, $\gamma/g = 1.9$, $f_{xyz} = \{0.4, 2.3, 0.3\}$. The dashed line corresponds to the case of all spins initially pointing up.

3.3 The initialization protocol

two control parameters g_{sb} and γ with the help of the quantities we already defined in section 3.3.2. We minimize the dimensionless excitation energy ϵ (or maximize the ground state fidelity f) simultaneously with respect to g_{sb} and γ . For this we use a Nelder-Mead algorithm [75], which is a standard non-linear optimization scheme based on a direct search method. We find that the optimization algorithm typically converges after about 50 simulation runs which does not significantly depend on the size of the system. However, we note that the optimization algorithm can lead to finding a local minima of the problem. In such cases, we use a global optimization algorithm implemented in Python programming language in the library NLopt [76].

On the other hand, we can target a certain amount of cooling (say, $\epsilon = 0.2$, or $f = 0.8$) that we want to achieve and calculate the time required to do so. For this, we perform the optimization scheme for increasing times t and stop when the target cooling is achieved. Alternatively, we can use Brent's method [77] which is an algorithm that combines the bisection and the secant methods to find the zero of a function between two given arguments.

For our simulations here, we use these algorithms as implemented in the Python-based ecosystem SciPy [78]. In an actual quantum simulator, however, we propose to use a hybrid algorithm where the energies measured on the quantum device are fed back into the classical optimization algorithm [79].

Chapter 4

Features of the dissipative protocol

In this chapter, we explore the different features of our protocol such as its scaling with respect to system size, its ability to prepare the system in an entangled state, its performance under decoherence etc.

4.1 Efficiency of the cooling protocol

The true success of any state preparation protocol as the one discussed here lies in its scaling with respect to the system size. We have already elaborated on the problem of exponential explosion and the need to find efficient techniques for the successful working of a quantum simulator in chapter 3. A protocol is said to be efficient if the resources required scales at most polynomially with the system size. In our protocol, the time required to cool the system is the important resource. Therefore, it's crucial to check how this preparation time t_p scales with increasing sizes of the system. We have already studied in section 3.3.4 how to determine the optimized time in order to prepare the system in a state with a given dimensionless excitation energy ϵ (or ground state fidelity f). Here, we are interested in finding out how this optimized preparation time t_p for preparing the system in a state with $\epsilon = 0.2$, scales with the system size N .

Figure 4.1 shows exactly this. We see here that, on a double logarithmic plot, the preparation time t_p follows a straight line with respect to the system N and has a slope of $\alpha = 3.1 \pm 0.1$. This means that the time required to prepare a state with the desired amount of cooling grows only polynomially with increasing system sizes and not exponentially, confirming that our protocol is efficient.

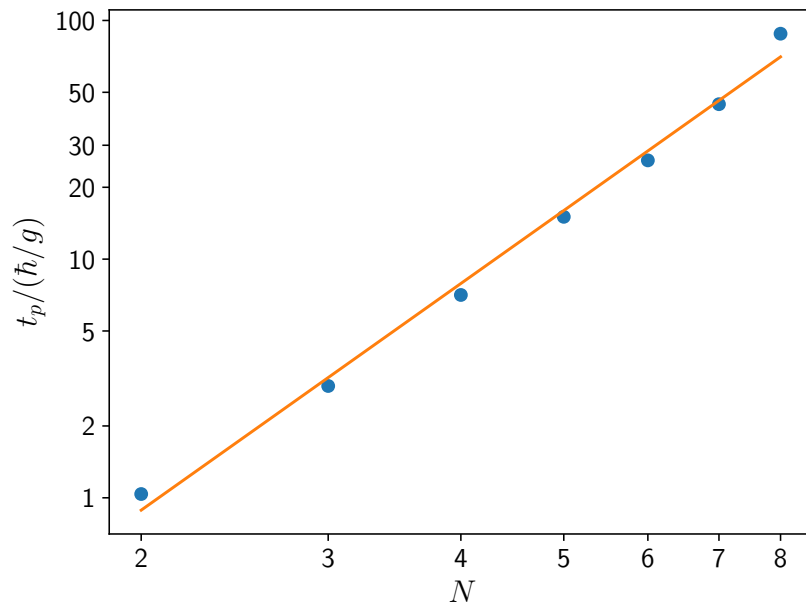


Figure 4.1: Scaling of the cooling protocol for the transverse field Ising model. The time t_p required to prepare the system in a state with dimensionless excitation energy $\epsilon = 0.2$ grows polynomially with the system size. The solid line is a fit to the data according to $t_p \sim N^\alpha$ where the exponent $\alpha = 3.1 \pm 0.1$.

4.1 Efficiency of the cooling protocol

Although the transverse field Ising model is a simple model, it already lies outside of the class of frustration-free Hamiltonians, since it is impossible for us to minimize the interaction term and the transverse field term at the same time. By showing the polynomial scaling of the cooling protocol for this model, we confirm that our protocol goes beyond the general class of frustration-free models.

However, we would still like to test our protocol on a critical model such as the antiferromagnetic Heisenberg model. Additional to being a critical point for the Kosterlitz-Thouless type of phase transition, the ground state of this model is highly entangled [80] making for a challenging candidate for our protocol to be tested on.

We have learnt in section 2.3.2 that there exists a symmetry in this model that conserves certain spin wave-excitations. Such a symmetry of course adds a minor complication concerning the ground state preparation in the sense that it restricts the protocol to be very efficient. This is due to the fact that the bath spin "talks" rather only to one of the two sublattices resulting in the possibility that a single excitation might get stuck in the system limiting the ground state fidelity of the final state prepared. In order to solve this issue, we extend the system-bath interaction to also the second last spin of the chain with the strength $g_{sb}/2$. The system-bath interaction Hamiltonian is now given by,

$$H_{int} = g_{sb} \sum_{x,y,z} f_i \left(\sigma_i^{(N)} \sigma_i^{(b)} + \frac{1}{2} \sigma_i^{(N-1)} \sigma_i^{(b)} \right) \quad (4.1)$$

Having written down all that is necessary, we can now apply the same strategy as we did for the Ising model in order to check the scaling of the preparation time t_p with respect to the system size N for the anti-ferromagnetic Heisenberg chain by following the same procedure as described in section 3.3.4. Figure 4.2 shows that the optimized preparation time t_p also scales polynomially with the system size. We also notice that the systems with odd number of spins require a smaller preparation time t_p compared to those for even system sizes. This can be explained by the fact that an anti-ferromagnetic Heisenberg chain with odd number of spins has a doubly degenerate ground state which provides for more pathways for faster cooling of the system. Finding the same exponent for the two data sets is not too surprising, because it can be expected to be linked to a universal exponent of the underlying phase transition. The prefactor, however, is a non-universal quantity, and can therefore have different values for the odd and even system sizes.

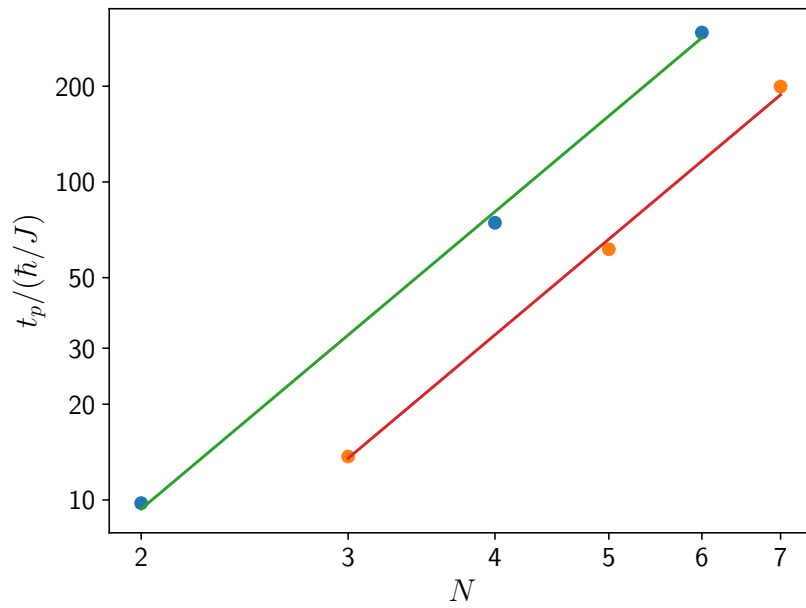


Figure 4.2: The optimized preparation time t_p to reach a final state with dimensionless energy of $\epsilon = 0.2$ for the anti-ferromagnetic Heisenberg model also grows only polynomially with respect to the system size N . The green line is a fit to the data for systems with even number of spins N and the red line corresponds to odd number of system sizes, and, both fit the data according to a common exponent $\alpha = 3.11 \pm 0.01$.

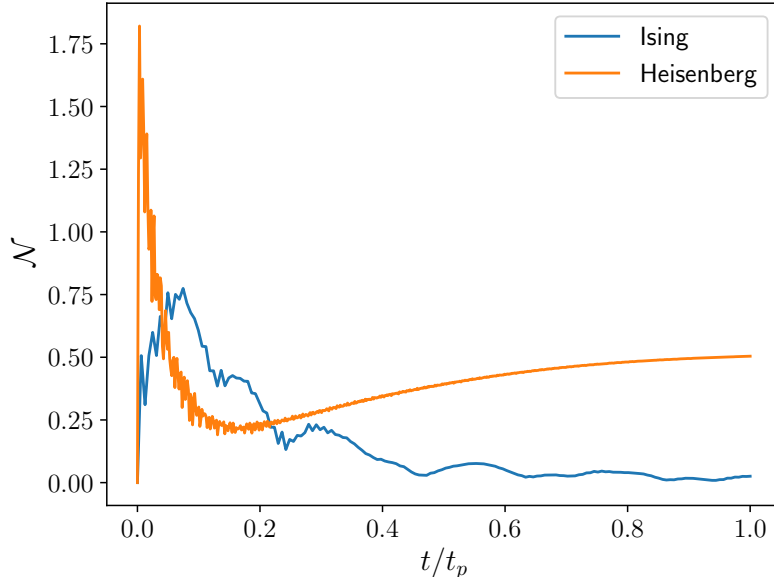


Figure 4.3: Negativity as an entanglement measure of the prepared states of a system of $N = 6$ spins. The blue line corresponds to the transverse field Ising model ($J/g = 5$) that has a low negativity in the long time limit. On the other hand, the orange line corresponds to the anti-ferromagnetic Heisenberg model that has a highly entangled final state. Both the curves shown are for the optimized parameters resulting in a final state with $\epsilon = 0.2$.

4.2 Preparing highly entangled states

We have seen in section 4.1 that the cooling protocol works also for the complicated case of antiferromagnetic Heisenberg model. Since this model has a highly entangled ground state, it tells us that our scheme is also successful in preparing a system in entangled states. Here, we explicitly test this ability of our protocol to prepare a system in an entangled state. To do this, we turn towards the quantity called the negativity that gives us a measure of the entanglement of a state. Given a subsystem A , the negativity is defined as

$$\mathcal{N}(\rho) = \frac{\|\rho^{T_A}\|_1 - 1}{2}, \quad (4.2)$$

where $\|\cdot\|_1$ denotes the trace norm, and, ρ^{T_A} is the partial transpose of ρ with respect to the subsystem A [81].

Figure 4.3 shows the negativity of the prepared state (calculated by treating half of the system as the subsystem A) for both the cases of the Ising model and the Heisenberg model as a function of progressing time t normalized with respect to the final preparation time t_p required to prepare the state with $\epsilon = 0.2$. We can see that the final state of the system is highly entangled for the case of the Heisenberg model, whereas, the Ising model on the other hand is hardly entangled.

A second observation that can be made is that there is an initial increase in the negativity. This is because typical high-energy states follow a volume law for entanglement measures whereas, the ground states exhibit a weaker area law [82]. Note, however, that for quantum information processing tasks, this initial entanglement is not really useful [83].

4.3 Measuring the many-body gap

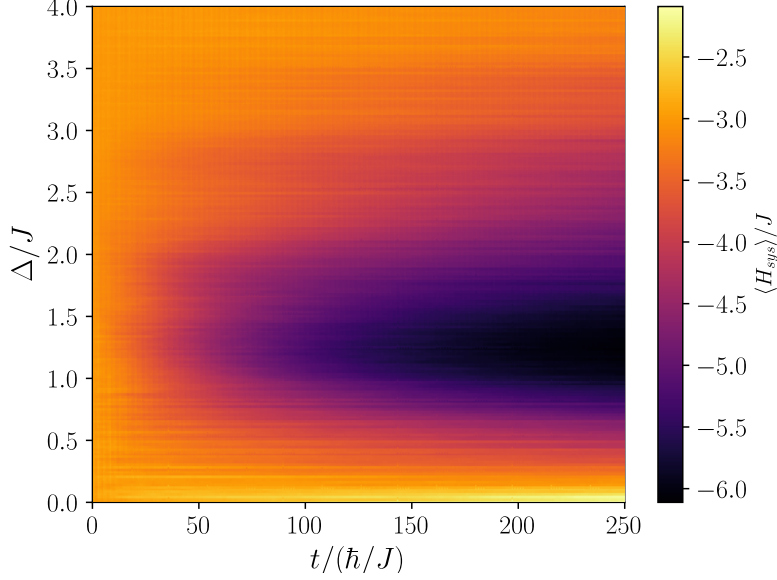
In section 3.3, we have motivated that the choice of the bath spin splitting Δ plays an important role in the efficiency of the cooling and for the most efficient energy transfer from the system to the bath spin, this splitting should be set resonant to the many-body gap. Here, we numerically simulate the dynamics for various choices of Δ in order to confirm this. From figure 4.4 we can see that this is indeed true. Part (a) is a density map showing the dynamics of cooling of the anti-ferromagnetic Heisenberg chain with $N = 4$ spins for various choices of the bath spin splitting Δ . The blue curve in part (b) shows the cross-section of the density map at the final time $t = 250\hbar/J$. Here, we can see that the system is cooled most efficiently around a certain choice of the bath spin splitting and this is exactly equal to the many-body gap. The same minimum is also seen by the orange curve which on the other hand is obtained by calculating the energy dissipated out by the bath spin.

These results motivate us to devise a scheme that allows us to measure the many-body gap of the system by using information just from the energy dissipated out of the dynamics E_{dis} . Thus, this dissipative protocol not only initializes the quantum simulator in its ground state but also helps extracting crucial information about the many-body system of interest. This is particularly important because in many of the setups of quantum simulation, it is extremely difficult to measure the energy of the system H_{sys} . This is because, one needs to typically perform quantum tomography on all the operators in the Hamiltonian. Moreover, in many architectures not all the coupling constants in the Hamiltonian can be perfectly controlled; leading to additional uncertainties in the estimated many-body gap of the system.

Figure 4.4 (b) therefore shows a promising way to estimate the many-body

4.3 Measuring the many-body gap

(a)



(b)

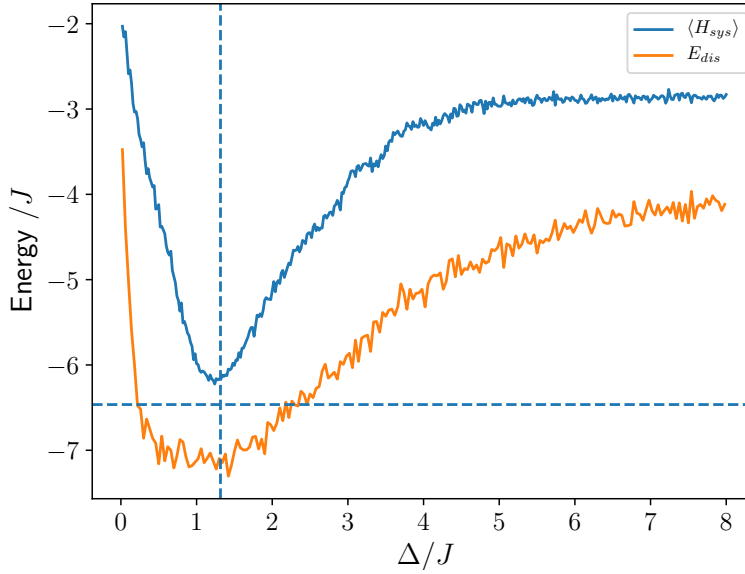


Figure 4.4: (a) Colour map showing the cooling dynamics as a function of the bath spin splitting Δ for the antiferromagnetic Heisenberg model with $N = 4$, $g_{sb}/J = 0.2$, $\gamma/J = 0.6$, $f_{x,y,z} = \{0.4, 2.3, 0.3\}$. (b) The most efficient cooling is observed for the case when the bath spin splitting is equal to the many-body gap (indicated by the vertical dashed line) i.e., $\Delta = \Delta E$. The horizontal dashed line indicates the energy of the ground state of the system.

gap of the system by only measuring the energy dissipated out by the bath spin during the cooling dynamics. Since each quantum jump that occurs in the dynamics lowers the energy of the system by an amount Δ , we can relate the dissipated energy E_{dis} to the number of quantum jumps N_{jump} by the relation $E_{dis} = N_{jump}\Delta$. Therefore, by calculating the number of quantum jumps, we can measure the energy dissipated out by the system.

There are two ways by which one can measure the number of quantum jumps N_{jump} experimentally. The first way is to directly count the number of quantum jumps, for e.g., by counting the number of photons emitted if the dissipation on the bath spin is implemented by an event of spontaneous emission. However, this is not always possible as it can be extremely challenging to count every single photon emitted with a high probability. This brings us, therefore, to the second way to measure the number of quantum jumps by calculating the integrated probability of finding the bath spin in the spin-up state using the equation,

$$N_{jump} = \gamma \int_0^{t_p} \text{Tr}\{\sigma_+^{(b)} \sigma_-^{(b)} \rho(t)\} dt \quad (4.3)$$

Here, the probability is integrated over the total preparation time t_p .

Although the main observation from figure 4.4 (b) is the identical minima in H_{sys} and E_{dis} for the optimal choice of Δ , we also observe the following: a slightly larger magnitude of the dissipated energy E_{dis} than the system energy E_{sys} . This can be explained by the fact that there is still a finite probability for quantum jumps to occur even at a large time limit. This is a consequence of the ground state of the system not being a perfect dark state of the quantum master equation due to a finite system bath coupling g_{sb} . These additional quantum jumps may occur also for non-optimal values of the bath splitting Δ , which brings us to the second observation, i.e., the broadening of the dissipated energy E_{dis} compared to the system energy H_{sys} .

4.4 Performance under decoherence

So far, we have only looked at idealized setups. However, in all of the quantum simulation architectures today, there are several sources of unwanted decoherence processes that cannot be eliminated. Therefore, it is essential to check the performance of the protocol under such processes.

For this, let us consider the worst case scenario of all local decoherence processes: σ_z spin flips on all the N spins of the transverse field Ising model acting at a rate of κ . We consider this the worst case scenario because, in

4.5 Experimental realization of the protocol

the ferromagnetic phase, one such spin flip will result in the creation of two domain-wall excitations. Meaning, that if a system is in its ground state, and one of the spins undergo a σ_z flip, the dimensionless excitation energy will increase approximately to $\epsilon \approx 2$.

To implement this process in our numerical simulations, we consider additional jump operators of the form $c_i = \sqrt{1/\kappa}\sigma_z^{(i)}$ on each of the spins of the system. Let us now consider the quantity κt_p , which basically tells us the probability of any spin to undergo a spin flip within the time t_p . The next step for us now is to analyze the behaviour of the number of excitations ϵ for different values of κt_p . Figure 4.5 shows exactly this for a system of $N = 4$ spins, and from the inset we see that for $\kappa t_p \approx 2$, the value of $\epsilon \approx 1$. This means that the system picks up only 1 excitation when all the spins of the system have undergone a decoherence process. Therefore, the characteristic scale observed here is κ , which is in strong contrast to the typical scale of $N\kappa$ that is observed in protocols involving adiabatic state preparation methods [84]. This improved performance under decoherence processes can be explained by the fact that the cooling protocol is itself based on a dissipative approach and therefore can correct additional decoherence events on its own.

4.5 Experimental realization of the protocol

In this section, we propose an implementation of the initialization protocol for a trapped-ion simulator. Note, however, that the protocol is, in fact, largely independent of the physical realization and we choose the trapped-ion environment just as an example.

We propose to confine a one-dimensional (1D) string of N $^{40}\text{Ca}^+$ ions in a linear Paul trap using the setup similar to the one described in the reference [85]. The energy level diagram for one such $^{40}\text{Ca}^+$ ion is shown in figure 4.6, where $|\uparrow\rangle = |^2\text{D}_{5/2}, m = +5/2\rangle$ and $|\downarrow\rangle = |^2\text{S}_{1/2}, m = +1/2\rangle$ denote the two levels of each of the spins in the spin-1/2 system. The energy splitting of $\hbar\omega_0$ between these two levels is coherently manipulated by radial laser beams. The bath ion can be isolated from the system by shelving the population to an auxiliary state $|\uparrow\rangle = |^2\text{D}_{5/2}, m = -5/2\rangle$ using a separate laser beam addressing only the bath ion. Note, that this would work only if there is sufficient distance between the bath ion and the nearest ion of the system chain.

The next step is the realization of the system and the system-bath Hamiltonians. Focusing first on the system Hamiltonian H_{sys} , the transverse field Ising like model has been implemented in trapped ion systems with up to 53

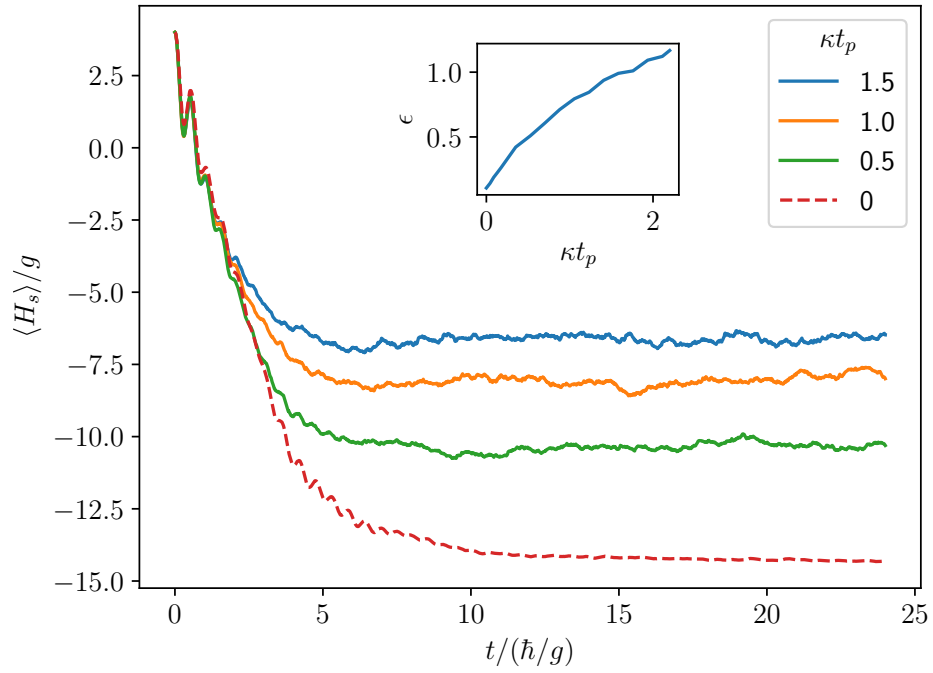


Figure 4.5: Performance of the cooling protocol in the presence of additional decoherence processes of different strengths κ in the transverse field Ising model (with $N = 4, J/g = 5$). The dashed red line is for the ideal case of no decoherence processes and corresponds to the state preparation with ground state fidelity $f = 0.9$. The inset shows the dimensionless energy ϵ for different values of κt_p , where t_p is the preparation time corresponding to the dashed red line.

4.5 Experimental realization of the protocol

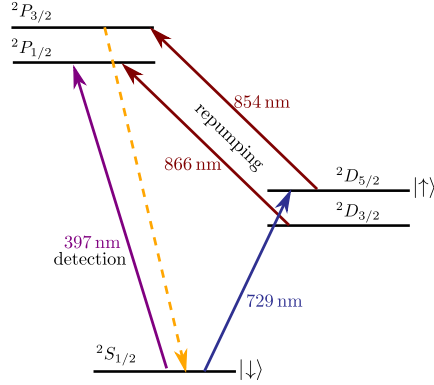


Figure 4.6: Energy level diagram of a $^{40}\text{Ca}^+$ ion and the scheme for the implementation of the cooling protocol in a trapped-ion architecture.

qubits [86]. A global bichromatic laser beam with a frequency of $\omega_0 \pm \delta$ can be used to implement a gate operation by coupling to all the radial modes. This results in the coupling between two spins i and j with a strength J_{ij} which follows a power law scaling according to $J_{ij} \propto 1/|i - j|^\alpha$ [55, 87], where the exponent α can be varied between 0 and 3 by changing the trap frequencies. The system-bath Hamiltonian H_{sb} , on the other hand, can be implemented using a separate laser that addresses only the bath spin and the neighboring system spin. The $\sigma_x \sigma_x$ type interaction between the spins can then be provided by a Mølmer-Sørensen gate [88, 89] on the radial motional modes.

To be specific, let us consider a system of 5 $^{40}\text{Ca}^+$ ions in a linear chain with single ion radial and axial trapping frequencies of $\omega_r = 2\pi \times 0.5$ MHz, and, $\omega_z = 2\pi \times 0.15$ MHz respectively [85]. For a Rabi frequency of $2\pi \times 125$ kHz for all the ions, and a detuning of $\delta - \omega_r \approx 2\pi \times 10.5$ kHz, the long-range interaction $J_{i,j}$ between two ions at sites i and j , ranges between $2\pi \times 2.7$ kHz and $2\pi \times 1.2$ kHz, and the largest Lamb-Dicke parameter is given by $\eta_{\max} = 0.128$. Note that these values are only valid in the Lamb-Dicke regime, which we verify in appendix C. Given these parameters, the bath spin is separated from the nearest system spin by a distance of around $14 \mu\text{m}$, which is large enough to provide a sufficient 10^{-7} factor suppression of the scattering rate in order for the electron shelving detection on the neighbouring ion when a beam is focused to $2.6 \mu\text{m}$ on the bath ion.

In such setups, the fluctuations of the global magnetic field contribute towards the most dominant decoherence events. These processes can be captured by an additional jump operator of the form $c = \sqrt{\kappa_c} \sum_i \sigma_z^{(i)}$, where κ_c is the collective decoherence rate which can be as low as $\kappa_c = 3.3$ Hz [90].

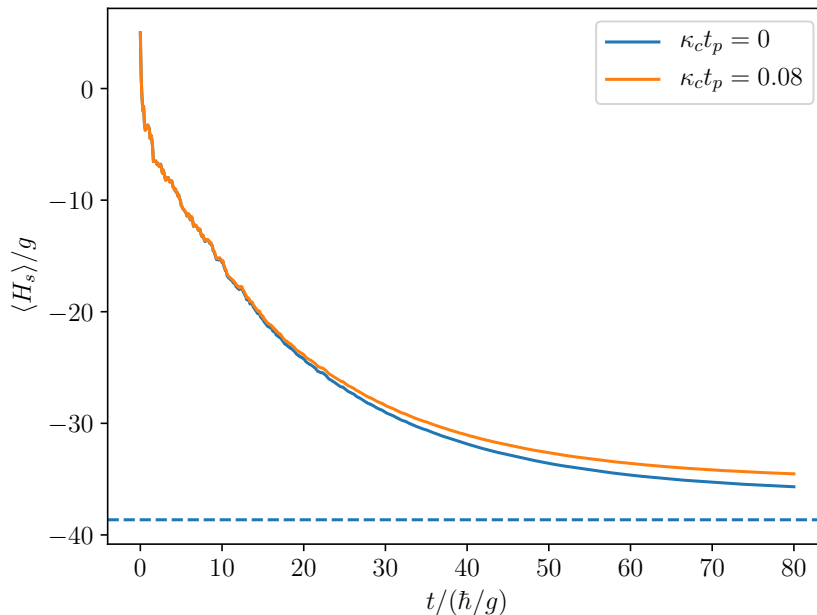


Figure 4.7: Cooling dynamics for an Ising-like chain with full long-range interactions in a system with $N = 5$ spins for a preparation time $t_p = 80\hbar/g \equiv 24$ ms. The blue line corresponds to the case of no additional decoherence processes resulting in the ground state fidelity $f = 0.92$, and the orange line shows the dynamics in the presence of a collective decoherence of strength $\kappa_c = 3.3$ Hz, resulting in a fidelity of $f = 0.89$. The ground state energy of the system is indicated by the the dashed line.

Figure 4.7 shows the cooling dynamics for such a system to an optimized ground state fidelity of $f = 0.92$ in the absence of any decoherence processes (blue curve). In the presence of a collective decoherence as described above, the system is prepared in a state with ground state fidelity of $f = 0.89$ (orange curve), resulting in a decrease of only about 3% in the fidelity.

Chapter 5

Cooling of molecular ions

Controlling and manipulating the quantum mechanical states of cold and ultra-cold atomic and molecular ions is particularly important and has been the goal in multiple fields of physics and chemistry. This has led to great advances in mass spectroscopy [91], high precision spectroscopy [92, 93, 94], reaction measurements [95, 96] etc. Trapping and cooling of atoms and atomic ions has enabled us to observe exotic phases of matter [97], to develop state-of-the-art technologies such as atomic clocks [98], quantum simulation [99], quantum computation [100, 101], and so on. Achieving the same level of control over molecules and molecular ions is promising as it could lead to novel insights into fundamental physics and chemistry [102, 103].

However, when compared with atoms, molecules have a rich internal energy level structure with vibrational and rotational states, as can be seen in the schematic shown in figure 5.1. These additional degrees of freedom pose great challenges to extend cooling strategies from the atomic species to the molecular counterparts.

In this chapter, we discuss the first steps to extend our cooling protocol presented in section 3.3.1 to cool molecular ions. Before that, let us first study the energy spectra of a diatomic molecule using mechanical models, focusing on the vibrational and the rotational degrees of freedom.

5.1 Vibrational energy levels

Molecular vibrations can be approximated as simple harmonic oscillators that are associated with an energy,

$$E_v = \left(v + \frac{1}{2}\right) h\nu \quad (5.1)$$

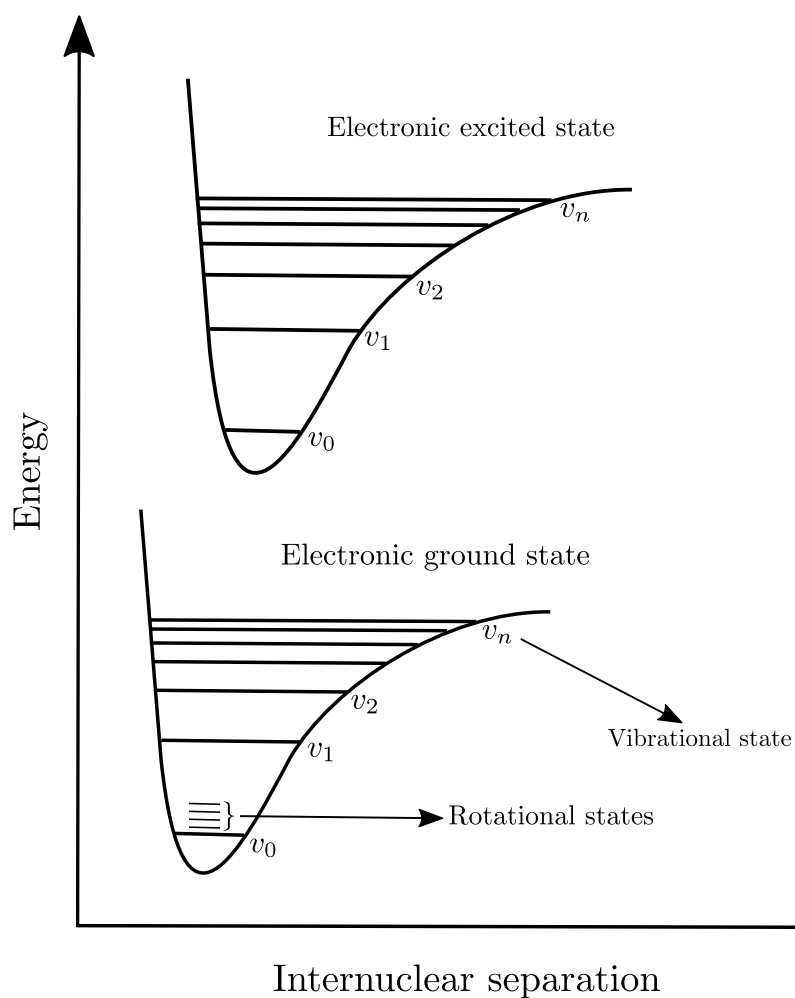


Figure 5.1: Schematic showing the energy levels of a molecule. The vibrational motions of the molecule give rise to the various vibrational levels v_n for each of the electronic levels, and the rotational motions of the molecule further give rise to different rotational levels giving rise to the spectrum.

5.2 Rotational energy levels

where, v is the vibrational quantum number, and ν is the vibrational frequency. Typically, however, one replaces $h\nu$ by the vibrational wave number ω_e and the energy is given in units of cm^{-1} .

Although this approximation holds fairly well for the bottom of the potential well, a real molecule, however, has anharmonic potentials, and one needs to consider higher order correction terms while going up the potential well. Often, only the first correction term is used, and the energy then reads,

$$E_v = \omega_e \left(v + \frac{1}{2} \right) - \omega_e \chi_e \left(v + \frac{1}{2} \right)^2, \quad (5.2)$$

where, χ_e is the anharmonicity constant.

5.2 Rotational energy levels

To study rotating systems, we use a mechanical model called the rigid rotor. The quantum mechanical linear rigid rotor model is often used to predict the rotational spectrum of a diatomic molecule. For this, we assume that the distance R between the two atoms comprising the molecule is fixed, and they rotate around each other about their center of mass. The Hamiltonian of this model in polar coordinates takes the form,

$$H = -\frac{\hbar^2}{2I_v} \left[\frac{1}{\sin \theta} \frac{\partial}{\partial \theta} \left(\sin \theta \frac{\partial}{\partial \theta} \right) + \frac{1}{\sin^2 \theta} \frac{\partial^2}{\partial \phi^2} \right], \quad (5.3)$$

where, $I_v = \mu R^2$ is the moment of inertia in the center of mass frame with μ being the reduced mass of the system. Notice that the moment of inertia depends on the vibrational quantum number v .

We can now solve the Schrödinger equation Eq. 1.1 and obtain the expression for the energy of the different rotational levels as,

$$E_J = \frac{\hbar^2}{2I} J(J+1), \quad (5.4)$$

where, J is the rotational quantum number, and each of the J levels are $(2J+1)$ -fold degenerate.

5.3 Selection rules for the ro-vibrational transitions

Depending on the kind of the transition in question, transitions between levels with certain vibrational and rotational quantum numbers are allowed

and those between certain levels are forbidden [104]. These rules are called the selection rules and are derived by calculating the transition moment integral which depends on the two involved states and the transition moment operator.

For electric dipole allowed ro-vibrational transitions, the selection rules are $\Delta v = 0, \pm 1, \pm 2, \dots$, and $\Delta J = \pm 1$. The transition having $\Delta v = \pm 1$ is called the fundamental transition, and the ones with larger Δv are called the overtones. For magnetic dipole allowed transitions, the selection rule is $\Delta J = \pm 1$. Therefore, each rotational level has two allowed transitions. On the other hand, the allowed change in the rotational quantum number for a Raman transition is $\Delta J = 0, \pm 2$.

The lack of selection rules for the vibrational transitions makes laser cooling of molecules extremely difficult, if not impossible. This is because a generic molecule in an electronically excited state may decay into any of the possible lower states making it impossible to scatter a large number of photons which is crucial to the concept of laser cooling.

5.4 Cooling to the rotational ground state

Here, we study the cooling of a molecular ion from an excited rotational state to the ground state using controlled dissipation. Since $\Delta J = \pm 1$ is forbidden for Raman transitions, let us consider the cooling from the $J = 2$ manifold to the $J = 0$ level. The $J = 2$ manifold has 5 degenerate states whose degeneracy can be lifted due to Zeeman splitting, whereas, the $J = 0$ level is non-degenerate. The driving between the different states i and j in the $J = 2$ manifold can be achieved with a time-dependent magnetic field $\Omega_{ij} \sin \omega_B t$. Here, the frequencies $\Omega_{ij} = \Omega_0 f_{ij}$ are determined from the Clebsch-Gordan coefficient matrix f_{ij} for the Zeeman transitions. The schematic for the dissipative cooling protocol is shown in figure 5.2 (a). The dissipation channel acts on the motional mode $|0'\rangle$ at a rate γ .

Figure 5.2 (b) shows the fidelity of the state of the system to the ground state $|0\rangle$ for different strengths of the dissipation rate γ . As can be seen from the figure, the system can be prepared in its ground state with high fidelities of $f > 0.95$.

These results, although preliminary, seem promising and in the future, it would be of interest to generalize the scheme to include all rotational levels.

5.4 Cooling to the rotational ground state

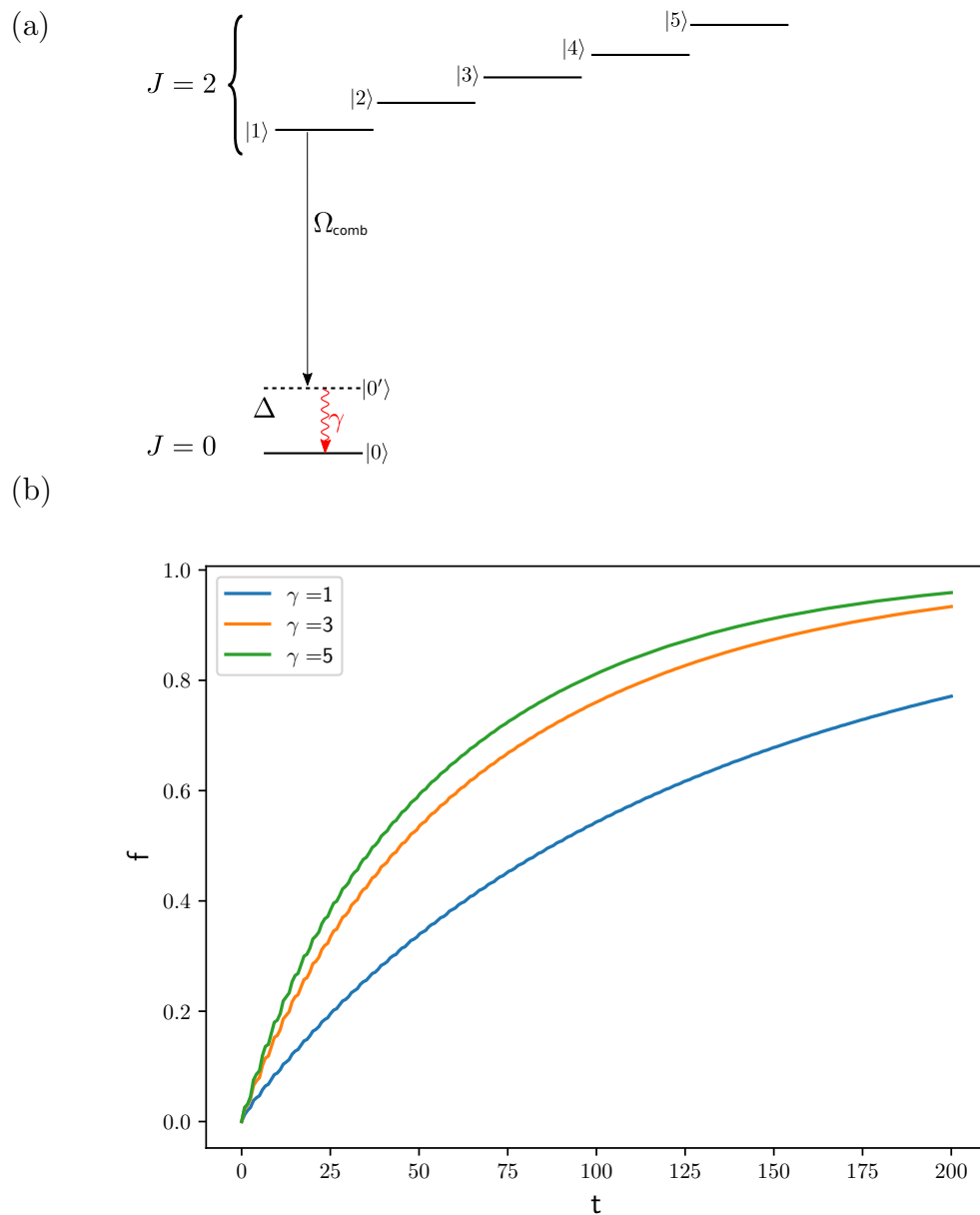


Figure 5.2: (a) Schematic for the dissipative cooling of the $J = 2$ manifold to the $J = 0$ rotational ground state. (b) Dissipative many-body dynamics resulting in the preparation of the system in its ground state with high fidelities of $f > 0.95$.

Part III

High-density quantum sensing with dissipative first order transitions

Chapter 6

Nitrogen-Vacancy centers in diamond

Diamonds, known for their striking beauty, have been adored and treasured as gemstones since ancient times. Although a chemically pure and structurally perfect diamond has no colour, natural diamonds often have a numerous amount of imperfections due to lattice irregularities such as inclusions (impurity atoms present in the crystal), vacancies (atoms missing in the crystal) etc. These crystallographic imperfections are responsible for dramatic changes in the properties of the diamond, especially the color. This is because stable impurities introduce narrow levels within the band gap of the crystal, perturbing the original energy level structure. This results in the coloration of an otherwise transparent crystal (see figure 6.1). Therefore, these defects are also called *color centers* and they emit across the spectrum, from the ultraviolet (UV) to the infrared (IR) [105]. Not only have they been the center of interest among gemologists for decades, but because of their stability and fascinating optical properties, they have also found applications in a large variety of fields ranging from quantum physics to biology [106, 107].

Of all the hundreds of luminescent defects in diamond, the nitrogen-vacancy (NV) center is the most studied. An NV center is a point defect in the lattice where a carbon atom is substituted by a nitrogen atom and an adjacent carbon atom is absent resulting in a vacancy (see figure 6.2 (a)). Although these centers are found in three different charge states (NV^+ , NV^0 , and, NV^-) [107, 108], due to its prominent features such as the electron paramagnetic resonance (EPR), the negatively charged NV center (NV^-), is usually employed in scientific research [109]. From now on, we will refer to the negatively charged NV^- simply as NV.

The most fascinating research using NV center has been the demonstra-

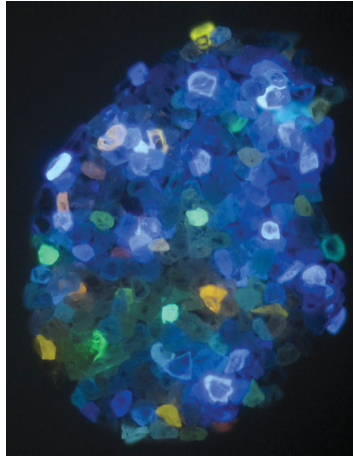


Figure 6.1: Fluorescence of natural diamond particles (each having a diameter of about $10 \mu\text{m}$), under the exposure of UV light, due to the presence of various types of defects. Image adapted from [106].

tion of room-temperature quantum physics in the fields of information processing [110, 111], nanoscale magnetometry [112, 113, 114, 115], nanoscale electrometry [116] and nanoscale thermometry [117, 118].

In the upcoming sections, we will learn some basic properties of the NV center and in the following chapters we will employ them to study high-density sensing using dissipative first order transitions.

6.1 Electronic level structure

The negatively charged NV center has six electrons, of which two are provided by the nitrogen atom, another three come from the three carbon atoms surrounding the vacancy, and the sixth electron is trapped in the lattice at the site. Thus, having an even number of electrons, and possessing a C_{3v} symmetry i.e., invariance under a $2\pi/3$ rotation around the symmetry axis [119], group theory dictates that the electronic states of the NV center comprises of spin triplet states (3A_2 and 3E) and the spin singlet states (1A and 1E). Figure 6.2 (b) shows the electronic structure of the NV center. The eigenstates of the triplets are typically given by the $S = 1$ description with $m_s = 0, \pm 1$ (denoted as $|0, \pm 1\rangle$). Their degeneracy is lifted by a zero field splitting of $D = 1.27$ GHz for the excited state and $D = 2.87$ GHz for the ground state. NV centers show a strong absorption at the wavelength of 532 nm [120, 121], at which they are excited from the ground state to the electronically and

6.1 Electronic level structure

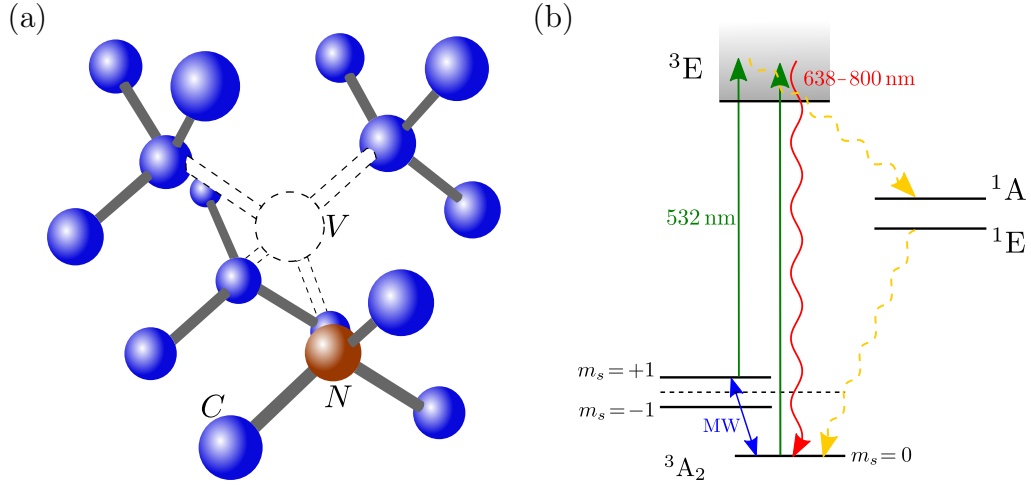


Figure 6.2: (a) Schematic of the NV center depicting the nitrogen atom (brown) and an adjacent vacancy (white) in a lattice of carbon atoms (blue). (b) Electronic structure of the NV center showing the triplet ground state 3A_2 and the excited state 3E . Dashed yellow lines indicate non-radiative transitions.

vibronically excited states which then decay back to the ground state via fluorescence with the zero phonon line (ZPL) between the ground state and the excited state at 637 nm (or 1.945 eV). These optical transitions between the ground and the excited states are primarily spin preserving [121]. However, since the metastable singlet is close to the excited state, the spin-orbit interaction induces inter-state crossing (ISC) [122, 123, 124] between the 3E and 1A states, allowing for the decay of the excited state into the ground state also via this route. The excited NV centers undergoing ISC decay into the singlet level with ZPL at 1042 nm, after which they cross over predominantly to the $m_s = 0$ state of the 3A_2 ground state. These processes are indicated by the yellow dashed lines in figure 6.2 (b). This cycle is spin non-conserving, and helps in the accumulation of more than 80% [125] of the population in the $m_s = 0$ state resulting in the spin-polarization of the NV center. Additionally, the ISC mechanism is mostly non-radiative in nature [121, 122], resulting in a higher probability per cycle of the $m_s = 0$ state for fluorescence than those in $m_s = \pm 1$ states with a contrast that can be as high as 30% [121, 113, 124]. This feature of spin-selective fluorescence is what is basically used for the optical readout in the most schemes of magnetometry using NV centers [113, 114, 126, 127, 128]

6.2 Magnetometry using NV centers

The use of NV centers as nanoscale sensors was first suggested in the references [129, 112] and experimentally demonstrated using single NV centers in references [113, 114] and in ensembles of NV centers in the reference [130] igniting much of the excitement in the following decade. Since then there have been multiple demonstrations of magnetometry using both single and ensembles of NV centers [109, 131] which have found applications covering a wide area ranging from condensed matter physics [132, 133] to nuclear magnetic resonance (NMR) technologies [134] to living systems biology [107, 134].

Although technologies involving alternative candidates such as the alkali vapour cells [135, 136] or the superconducting quantum interference devices (or simply SQUIDS) [137, 136] offer exceptional sensitivities in measuring magnetic fields, their applications at the nano-scale level are limited due to technical complications or low spatial resolution of the sensors. Employing NV centers solves these issues making them promising candidates in nano-scale sensing and magnetometry. This can be owed to the fact that the NV centers can be easily initialized and read-out using just a single 532 nm solid state laser. Apart from the fact that these sensors can work at friendly conditions of temperature, pressure etc., diamonds are also chemically inactive, making them suitable to be placed in close proximity to the source of the magnetic field [138] enabling a spatial resolution of the order of nanometers [139, 140].

As Rondin et al. suggest in the reference [131], that the ultimate test for NV based sensing and magnetometry applications would be to provide novel insights e.g., into processes at the level of a single protein, or exotic new states of matter etc., that could not be possible using current alternative experimental techniques. Banking on the examples [141, 142, 143, 144], they also believe that such a breakthrough could be demonstrated in the near future.

6.2.1 Sensitivity of the sensor

The sensitivity of a spin-based quantum sensor is mostly limited by the quantum noise that is linked with spin projection. For sensors based on NV centers, this is mostly governed by the photon shot noise [114, 112] and the precision scales as $1/\sqrt{N_{\text{photon}}}$ where N_{photon} is the number of photons collected. For quantum metrology schemes, the precision also depends on the accumulation of the phase during the measurement time τ . Since the phase scales linearly with time τ , but the measurement repetition rate scales as

$1/\sqrt{\tau}$, the optimal sensitivity also scales as $1/\sqrt{\tau}$ [145].

For a density of n non-interacting $S = 1/2$ spins in a volume V of the sample, this is given by the following [135, 112, 124, 108].

$$\delta B \simeq \frac{1}{g\mu_B} \frac{1}{\sqrt{nV\tau}} \quad (6.1)$$

where δB is the smallest detectable magnetic field, $\gamma = g\mu_B$ is the NV gyromagnetic ratio ($\gamma = 1.761 \times 10^{11} \text{s}^{-1} \text{T}^{-1}$) with g being the ground state Landé factor and μ_B being the Bohr magneton. The free precession time τ per measurement is chosen for optimal sensitivity and depends on the characteristic decay time of the spin relaxation. In the case of DC magnetometry, this is the ensemble inhomogeneous dephasing time T_2^* which is typically of the order of $1\mu\text{s}$ in most implementations currently [108]. For AC sensing protocols the relevant time is the T_2 coherence time which is normally longer than the T_2^* dephasing time by an order of magnitude of one or two [146, 108].

6.2.2 Sensing at high densities

Performing magnetometry using an ensemble of NV centers has advantages over using just a single center because the projection noise per unit volume scales as inverse square root of the density n of the sensing spins as seen in the previous section 6.2.1. This results in an improved sensitivity of the sensor. Besides, the NV centers in an ensemble are typically distributed along all four crystallographic orientations, each of which are sensitive to a different component of the magnetic field. This feature enables the measurement of not just the magnitude but also the direction of the magnetic field making the NV-ensemble diamond sensor a vector magnetic sensor.

However, at the small scale of a nano-sensor, the NV centers lie at close proximities to each other resulting in strong dipolar interactions between them. These interactions pose great challenges as they contribute towards dephasing of the NV spins resulting in shorter T_2^* , T_2 , and T_1 relaxation times [131, 147] and therefore limiting the sensitivity of the sensor.

In order to overcome this problem a few protocols have been proposed that mostly target to extend the relevant spin relaxation times T_2^* for DC field sensing [148] and T_2 for AC field sensing [149]. However, since these schemes involve partially decoupling the spins from the magnetic fields to be sensed, the gain in sensitivity due to extended relaxation times may be counterbalanced by the partial decoupling.

A second class of proposals to tackle this issue is to use highly entangled states that can beat the standard quantum limit of $1/\sqrt{N}$ for spin projection noise and may approach the Heisenberg limit of $1/N$ [150]. However, this

approach enforces constraints that are challenging to realize experimentally and moreover only applicable to a small range of magnetometry applications [108].

The problems discussed here urge us to develop more methods and ideas in order to enable nanoscale quantum sensing. Here, we propose a novel approach to solve this problem using controlled dissipation. The key idea is to exploit dissipative first order transitions to perform sensing. The principle here is that the signal to be detected triggers a phase transition in the sensor at its critical point resulting in a large change in the value of a physical observable. This is true even for very small change in the signal thereby allowing us to detect even a weak signal with high sensitivity. This is in contrast, however, to quantum phase transitions in systems that are of second-order in nature where a weak signal cannot cause a big change in the observable [151].

In the next chapter, we describe our protocol and highlight its features as applied to two-dimensional lattice geometry and in the following chapter we extend this to three-dimensional systems.

Chapter 7

Dissipative first order transition

Having motivated the reason to study NV based quantum devices for magnetometry, and the need to devise schemes to perform quantum sensing using ensembles of NV centers, in the following, we present our sensing protocol that uses dissipative first order transitions and present results for a two-dimensional setup with a lattice geometry.

7.1 The sensing protocol

The setup (see figure 7.1 (a)) consists of an ensemble of N interacting NV centers in a diamond undergoing microwave driving with a Rabi frequency Ω . Additionally, we assume that the NV centers are aligned parallel to the external magnetic field [152]. We also assume a sufficiently strong bias field such that only transitions with $m_s = 1$ state are near resonance as this allows us to describe each of the NV centers using an effective two-level i.e., a spin-1/2 description.

The Hamiltonian of such a system can then be written in the rotating frame of the driving as,

$$H = \frac{\hbar\Delta}{2} \sum_i^N \sigma_z^{(i)} + \frac{\hbar\Omega}{2} \sum_i^N \sigma_x^{(i)} + \sum_{i<j}^N V_{ij}. \quad (7.1)$$

Here, Δ is the detuning from the electron spin resonance, and, V_{ij} is the magnetic dipole-dipole interaction which takes the following form,

$$V_{ij} = (1 - 3 \cos^2 \vartheta_{ij}) \frac{\mu^2}{|\mathbf{r}_i - \mathbf{r}_j|^3} \left\{ \frac{1}{4} [1 + \sigma_z^{(i)}] [1 + \sigma_z^{(j)}] - \sigma_+^{(i)} \sigma_-^{(j)} - \sigma_-^{(i)} \sigma_+^{(j)} \right\}, \quad (7.2)$$

where μ is the magnetic dipole moment, and ϑ_{ij} is the angle between the NV axis and the vector connecting sites \mathbf{r}_i and \mathbf{r}_j . The exact form of the Hamiltonian 7.1 is derived in appendix D.

The dissipation on each site is implemented by the optical pumping of the NV centers towards the $m_s = 0$ state with a rate γ , that can be controlled by the strength of the green laser pump (see figure 7.1 (a)). For the calculations here, we assume that the distance between the nearest neighbours is $r = 5$ nm and set the optical pumping rate to be $\gamma = 1$ MHz.

We can now write down the quantum master equation in its Lindblad form as,

$$\frac{d}{dt}\rho = -\frac{i}{\hbar}[H, \rho] + \sum_i^N \gamma \left(\sigma_-^{(i)} \rho \sigma_+^{(i)} - \frac{1}{2} \left\{ \sigma_+^{(i)} \sigma_-^{(i)}, \rho \right\} \right). \quad (7.3)$$

The last step of the sensing protocol as shown in figure 7.1 (b) is the optical readout which gives us the information of the NV spin state. Here, we are interested in the total magnetization of the NV system $m = \sum_i (1 + \langle \sigma_z^{(i)} \rangle) / (2N)$, especially its response to changes in the driving field Ω as we expect a behavior as shown in figure 7.1 (c). This is because our system is very similar to driven-dissipative Rydberg systems that are known to undergo a first order phase transition [153, 154, 155]. In order to confirm the existence of a first order phase transition in our system, we will analyze the behavior of the magnetic susceptibility χ , which is the first derivative of the magnetization, for increasing system sizes.

In the following, we first study two-dimensional systems in lattice geometries and then move onto systems with imperfections related to disorders and decoherence processes. For all our calculations below, we assume a periodic boundary condition. We perform numerical simulations of the full quantum master equation 7.3 based on the wave-function Monte Carlo approach implemented in QuTiP [29], as discussed in section 1.4, which we extend here to a heavily parallelized version. This allows us to go to a system size of as high as $N = 20$ spins, which, within our knowledge, is so far the largest number of spins treated in open quantum many-body systems while retaining the entire Hilbert space.

7.2 Two-dimensional lattice geometry

Starting with the simplest case of only nearest-neighbour interactions, let us consider lattice geometries with equal number of NV centers on both x and y

7.2 Two-dimensional lattice geometry

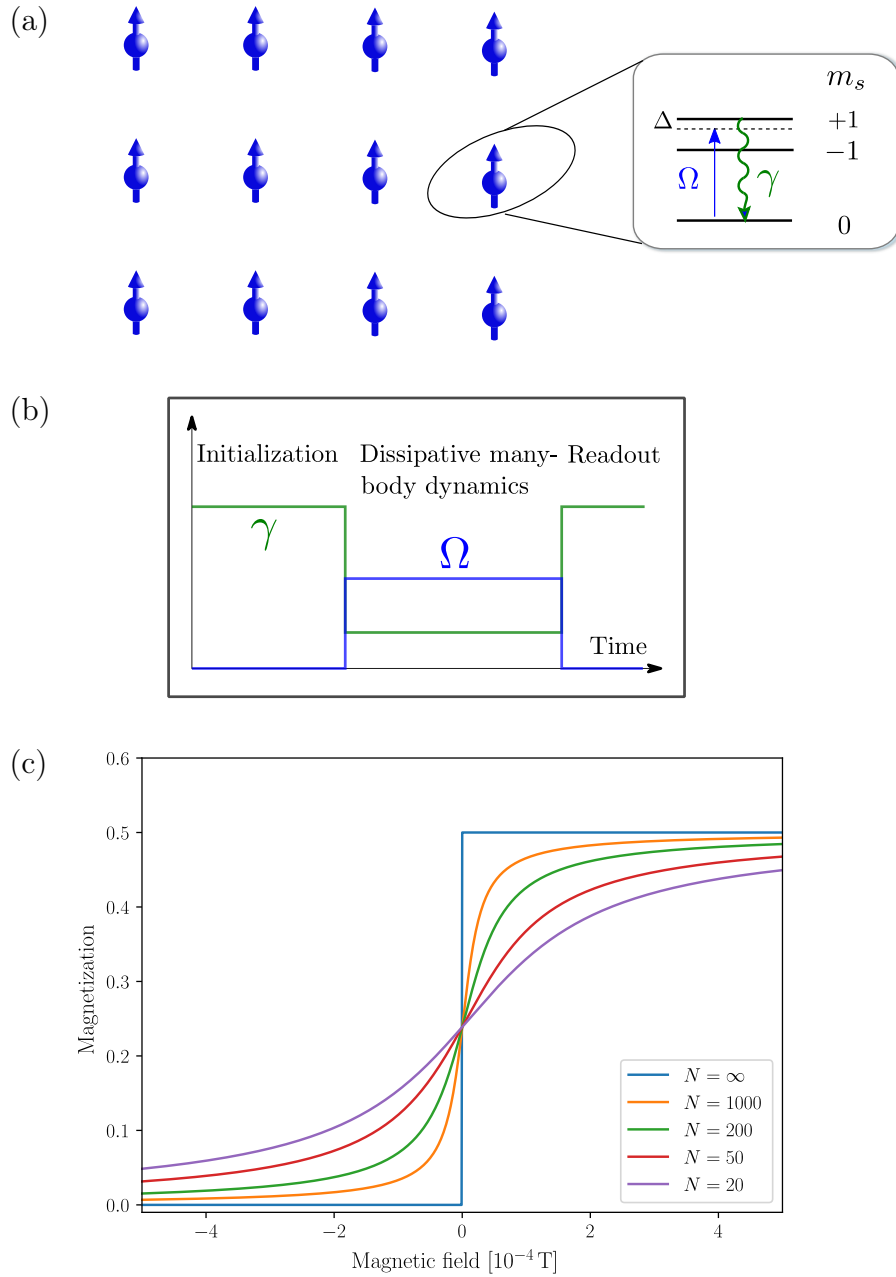


Figure 7.1: Setup for the sensing protocol. (a) The NV centers are arranged in a two-dimensional lattice geometry with each of the centers described using an effective two-level description. Inset shows the energy level diagram for a single NV center. (b) The sensing protocol where the system of NV centers is first initialized, followed by the dissipative many body dynamics and finally the readout of the NV spin state. (c) Sketch of the strong response the NV magnetization across the phase transition for increasing system sizes which can be used to perform sensing. 85

axes i.e., isotropic geometries with $N_x = N_y$. As the first step, we investigate the NV magnetization m at different strengths of the driving field Ω .

Figure 7.2 shows the results for a system of $N = 16$ NV centers in a 4×4 geometry for driving frequencies Ω of 1 MHz (blue curve), 5 MHz (orange curve), and, 8 MHz (green curve). The shaded regions show the variance of the NV magnetization as calculated using the statistics from 1000 different Monte Carlo trajectories by

$$(\Delta m)^2 = \sum_{j=1}^n \frac{(m_j - \bar{m})^2}{n - 1} \quad (7.4)$$

where \bar{m} is the mean magnetization at a time t and n denotes the number of trajectories. An obvious observation is that the orange curve corresponding to $\Omega = 5$ MHz shows a large variance in the magnetization as compared to the other two cases. Such a behavior can be explained using the fact that at any phase transition, there are two solutions which the numerics can basically choose from. Therefore, this already indicates the presence of a phase transition in the NV magnetization.

This by itself, however, is not enough to prove the existence of any phase transition. Therefore, in order to further probe into this, we study the behavior of the derivative of the magnetization with respect to the driving field strength $\chi = \partial m / \partial \Omega$. This derivative χ is called the magnetic susceptibility and is a very good response function that gives us a measure of the change in magnetization m due to the change in an external parameter, here, the driving field Ω .

Figure 7.3 shows the response of this magnetic susceptibility χ to varying field strengths Ω for isotropic geometries of 3×3 (blue curve) and 4×4 (orange curve). The solid lines are fits to the data set that closely fit the Weibull distribution given by,

$$\chi(\omega) \sim \Omega^{k-1} \exp \left[- \left(\frac{\Omega}{\lambda} \right)^k \right]. \quad (7.5)$$

Interestingly, the Weibull distribution has been previously studied with respect to the relaxation from metastable states where the parameter k controls the decay rates of these states [156, 157].

A crucial feature relevant to our study here, is that for a certain value of the driving field Ω , the magnetic susceptibility χ assumes the highest value i.e., there is a peak in χ . Secondly, we also notice that this peak is larger for a system of 16 (4×4) NV centers than for a system of 9 (3×3) NV centers. The question now is, how does this peak in susceptibility scale with

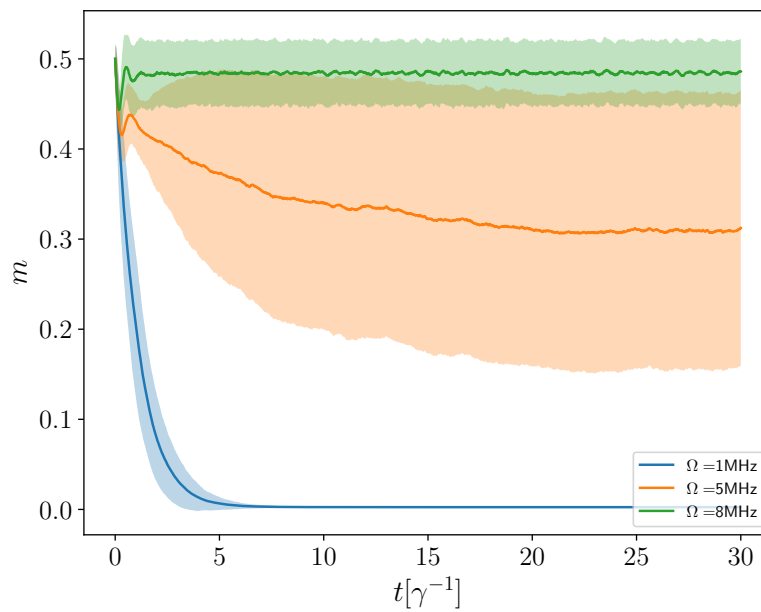


Figure 7.2: Magnetization of a system of 16 NV centers in a 4×4 geometry for various strengths of the driving field Ω . The shaded region shows the variance of the magnetization at each point in time. Large variance in magnetization at $\Omega = 5$ MHz compared to the other two regimes hints at the existence of a phase transition as the numerics chooses between the two steady state solutions present at the transition.

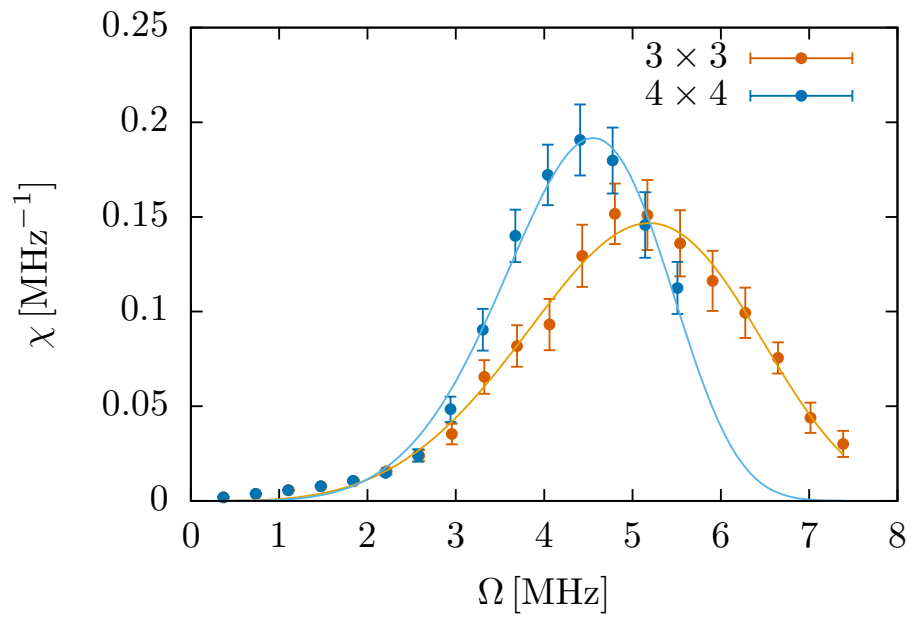


Figure 7.3: Magnetic susceptibility χ for varying driving strengths Ω for 3×3 and 4×4 lattice geometries. Results shown are obtained by averaging 1000 wave-function Monte Carlo trajectories. The solid lines are fits to the data that follows a Weibull distribution.

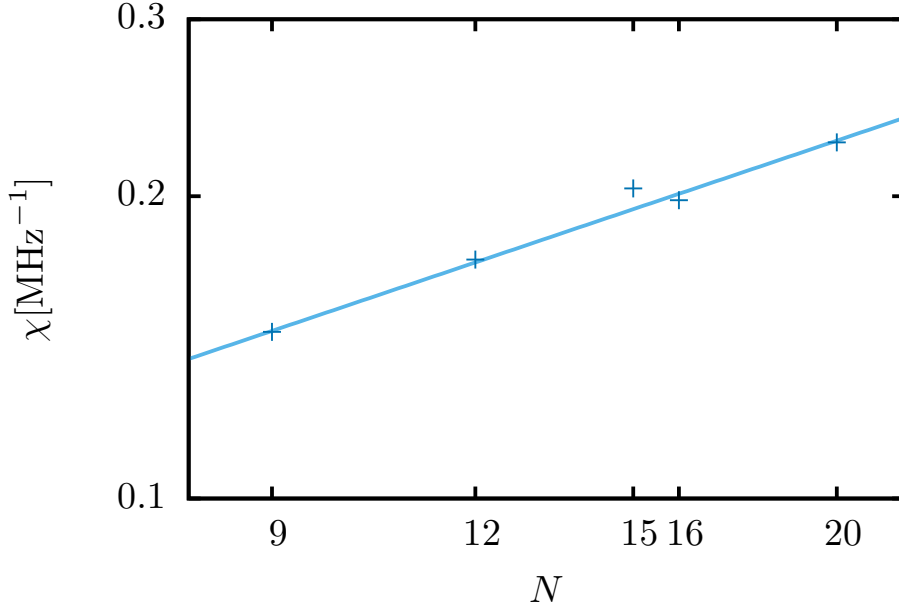


Figure 7.4: The peak of the magnetic susceptibility diverges on a double logarithmic plot with increasing system size indicating the existence of a first order phase transition in magnetization.

increasing system sizes? To analyze this, we also need to include anisotropic geometries where $N_x \neq N_y$ (3×4 , 3×5 and 4×5).

We calculate the peak in susceptibility numerically for each system size N , by fitting a quadratic function around the maximum. When we plot these data points on a double logarithmic scale, we see from figure 7.4, that the peak χ increases with N .

However, it is also noticeable that the data points do not exactly fall on the solid line which is the fit, but are rather scattered around this line. This is explained by the fact that at small system sizes, the effects of anisotropy are easily manifested. Therefore, in order to account for this, one needs to perform a modified finite size scaling [158]. Our ansatz for the scaling function is given by

$$\chi = cN^\alpha \tilde{\chi}(\lambda), \quad (7.6)$$

where $\lambda = N_x/N_y$ is the ratio of the number of spins on the x and y directions respectively, and gives a measure of the anisotropy in the geometry. The parameters c and α are numerical constants that can be determined by fitting our simulation data. Crucially, a positive value for the exponent α indicates the existence of a first order phase transition. Since we want to eliminate the

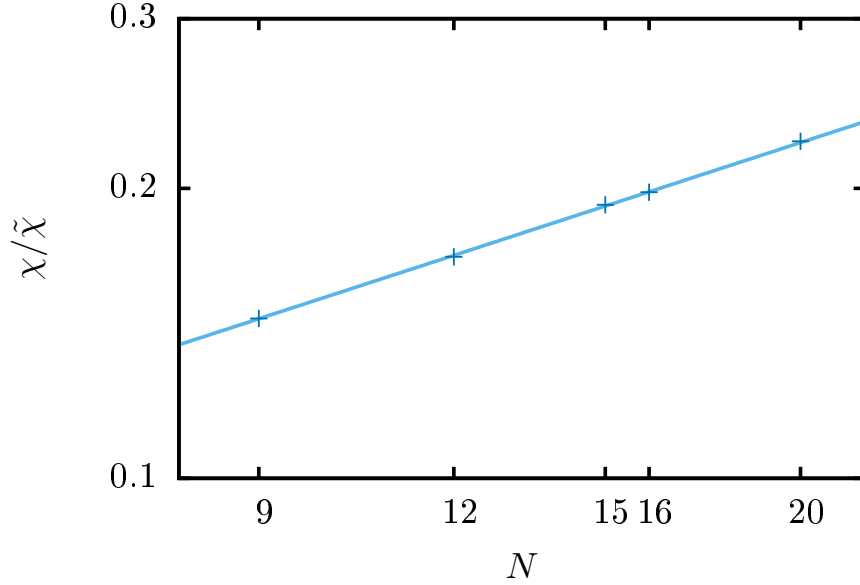


Figure 7.5: Modified finite size scaling results in the collapse of the data onto a single line. The reduced susceptibility $\chi/\tilde{\chi}$ scales with system size N according to $\chi/\tilde{\chi} \sim N^\alpha$ with the exponent $\alpha = 0.527 \pm 0.006$.

effects of the anisotropy, we need to choose the scaling function $\tilde{\chi}(\lambda)$ such that it satisfies the following two conditions:

$$\tilde{\chi}(\lambda) = \tilde{\chi}(1/\lambda) \quad (7.7)$$

$$\tilde{\chi}(1) = 1. \quad (7.8)$$

As a consequence, this leaves us with only the even powers of $\log[\lambda]$ when we perform a series expansion. For anisotropies that are not too large, we can truncate the expansion at the second order and the scaling function is then given by

$$\tilde{\chi}(\lambda) = 1 + d[\log \lambda]^2 + O([\log \lambda]^4) \quad (7.9)$$

Here, d is another numerical constant that can again be found by data fitting. Eq. 7.6 finally takes the following form.

$$\chi = cN^\alpha(1 + d[\log \lambda]^2) \quad (7.10)$$

When we now plot the reduced susceptibility $\chi/\tilde{\chi}$, as a function of the system size N , it should now take the form of a simple algebraic expression given by our ansatz Eq. 7.6. Figure 7.5 shows that this is indeed the case, reassuring

the validity of our ansatz. Furthermore, we find the exponent to be positive confirming the presence of the first order phase transition. Interestingly, the value of the exponent determined is $\alpha = 0.5$, which is basically the same scaling with respect to the sensitivity that is exhibited by a non-interacting ensemble. This means that the sensitivity of our dissipative protocol is about the same as that for a non-interacting ensemble. We will give an estimate for the sensitivity in section 7.6.

7.3 Effects of long-range interactions and vacancy disorder

So far, we have only studied the simplest case of nearest neighbour interaction which is clearly an idealized setup. Therefore, let us study the effects of long-range interactions in the system. Besides, in a real sample of diamond, there are various imperfections that are related to disorder in the lattice, or, various sources of additional decoherence processes. Here, we focus on the effects of the full long-range interactions and disorder in our system and in the following section 7.4 we will study the performance of our sensor under decoherence processes.

We are interested in the investigation of the following:

- i) full long-range dipolar interactions,
- ii) disorder caused by a vacancy in the lattice with only nearest-neighbor interaction,
- iii) disorder caused by a vacancy in the lattice with full long-range dipolar interactions.

In order to compare these three cases with the previously presented case of only nearest neighbour interactions, we need to normalize the interaction strength V_{ij} such that the energies in all the four cases are the same. We now run the wave-function Monte Carlo simulations of the quantum master equation as earlier and plot the results. As can be seen in figure 7.6, the results change only quantitatively. Qualitatively they are the same, showing that the protocol also works in this realistic scenario.

These results are consistent with the following picture that the disorder relating to NV interaction energies or missing sites due to off-axis NV centers only affect the strengths of the coupling constants but cannot reverse their signs. Therefore, they do not play an important role. The analysis of random-bond Ising models [159] shows that the underlying phase transition survives such types of disorder.

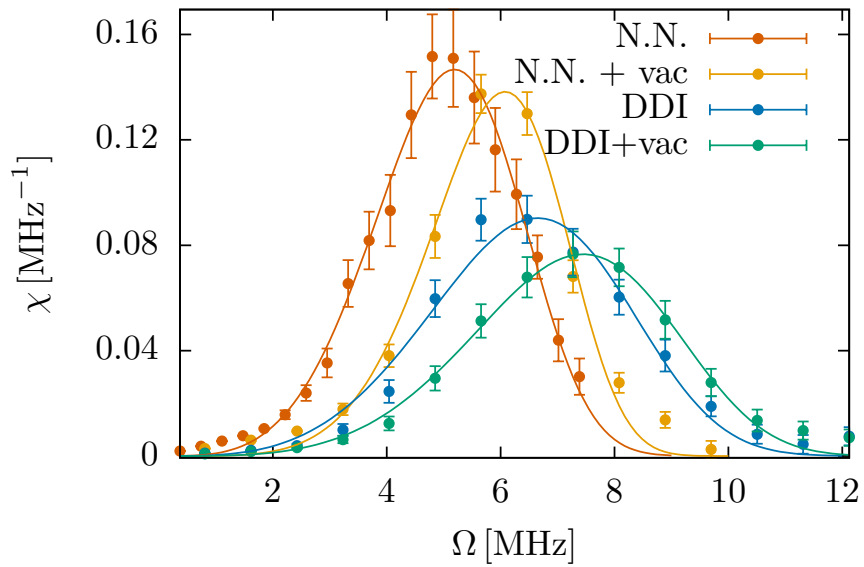


Figure 7.6: Steady state magnetic susceptibility χ for various different cases for 3×3 geometry obtained by averaging results from 1000 Monte Carlo trajectories. The orange and yellow curves correspond to the case of the spins having only nearest neighbour (N.N.) interaction, whereas, the blue and the green lines are for systems that also include the full long-range dipole-dipole interactions (DDI). Additionally, the yellow and the green lines also include a vacancy (vac) disorder present in the lattice.

7.4 Performance under decoherence processes

The next step in our study is to analyze the performance of the dissipative sensor under decoherence processes. In a typical system of NV centers, a dominant challenge is posed by decoherence processes caused by residual nitrogen impurities and by ^{13}C nuclear spins. Hence, we study these processes here and investigate how limited the sensor is by the T_2 decoherence time. To do this, we add additional jump operators to the quantum master equation $c_i = \sqrt{1/T_2}\sigma_z^{(i)}$ on each of the sites.

Since we are interested in the extent to which our protocol is limited by the T_2 decoherence times, we need to perform the analysis at the thermodynamic limit for which we turn to the variational principle for open quantum systems [160]. These simulations, shown in figure 7.7, are performed by Hendrik Weimer. Here, we see that the phase transition is quite robust against decoherence processes. It not only survives in a regime where the decoherence is perturbatively small but also in the regime where the decoherence rates are several times higher than the coherent interaction strengths. Here, the dipole-dipole interaction strength is $V = 2\pi \times 400$ kHz at a separation of $r = 5$ nm between the NV centers. This is about an order of three magnitudes smaller than the decoherence rate of about 50 ns at which the phase transition vanishes. This strong robustness can be accredited to the steady state being an effective non-classical thermal state [161]. Such a state is less vulnerable to decoherence processes as it is diagonal in an appropriate energy eigenbasis. Notice, however, that these additional decoherence processes result in a shift in the point of transition. Therefore, before using the device for quantum sensing, one needs to characterize its coherence properties.

7.5 Sensing DC fields

Here, we investigate the magnetic susceptibility with regard to changes in the magnetic field. A change in the magnetic field will result in a shift of the resonance condition of the microwave driving of the NV centers. Therefore, we can model the effect of a variation in the magnetic field with respect to the external bias field B_0 , by varying the finite detuning Δ in the Hamiltonian 7.1 but for a fixed microwave driving Ω .

The magnetic susceptibility is now the first derivative of the magnetization with respect to the detuning given by $\chi = \partial m / \partial \Delta$ and is shown in figure 7.8. We again notice similar behavior of the DC susceptibility as compared to the previous cases. Since the peak of the susceptibility here for the DC field is only slightly bigger than the case of the AC field, we suggest that

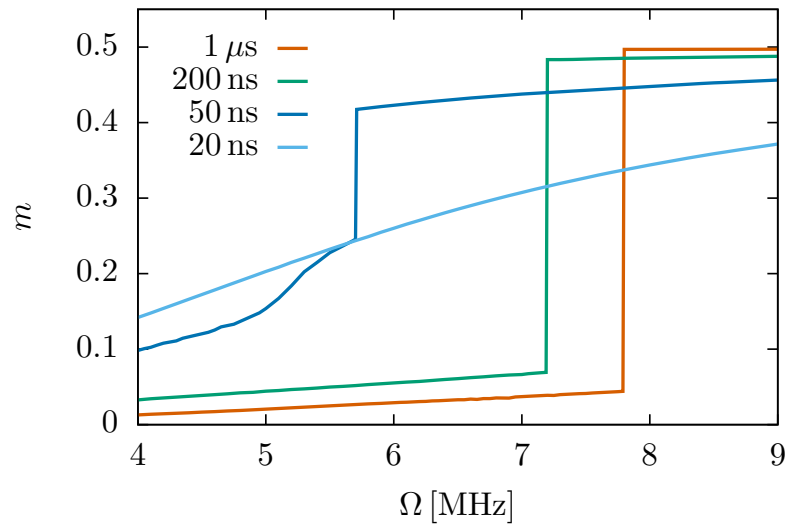


Figure 7.7: Performance of the sensor under decoherence processes with various T_2 times. The phase transition survives even in the regime where the decoherence rates are several times stronger than the coherent interaction strengths. The phase transition vanishes only at a very small T_2 time. Figure taken from reference [162].

7.6 Sensitivity estimation

the sensitivities for both these cases will be comparable. These results are in contrast with NV magnetometry using non-interacting ensembles where the DC sensitivity is limited by the T_2^* times which is, in general, worse than the T_2 times in the case of AC sensing. Thus, our protocol is especially useful for DC sensing.

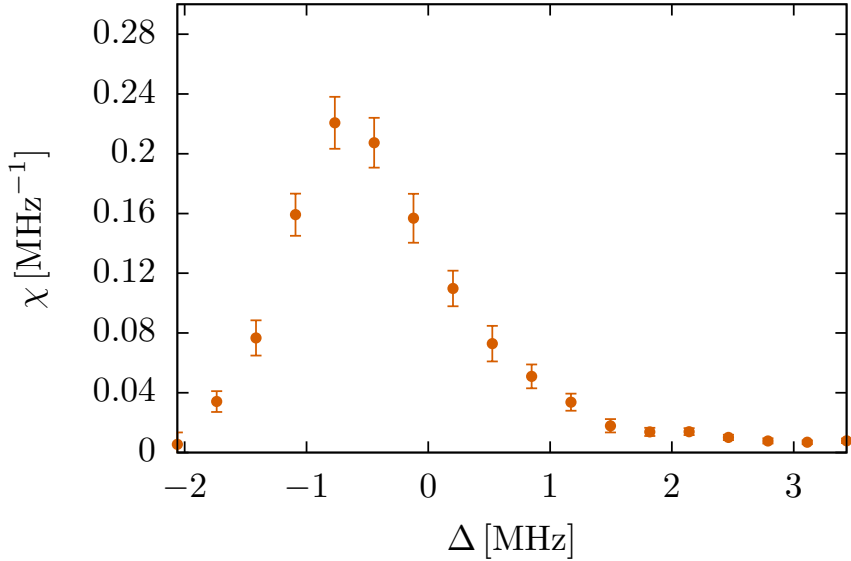


Figure 7.8: Magnetic susceptibility with respect to changes in the magnetic field, here shifts in the detuning Δ , for a system of NV centers in a 3×3 geometry. The behaviour of the peak of the susceptibility similar to that for the previously shown case of AC field.

7.6 Sensitivity estimation

We have previously mentioned that the sensitivity of the dissipative sensor would be similar to that of a non-interacting ensemble owing to the same scaling exponent of $\alpha = 0.5$. However, as opposed to the case of a system of non-interacting NV centers where the measurement is limited by the photon shot noise [131], in our case it is rather limited by the bimodal distribution of the system close to the first order transition. Particularly, the signal for the total NV magnetization behaves as $N(m_0 + \chi_{DC}B)$, where B is the external field that is to be measured. From statistics of bimodal distributions, we know that the noise is given in terms of its standard deviation by

$N/2\delta m$ where δm is the jump in the magnetization at the phase transition in the thermodynamic limit. Since we know from section 7.2 that the magnetic susceptibility scales as \sqrt{N} close to the transition, we can estimate the sensitivity using

$$\eta_{DC} = \frac{\delta m}{2\chi_{DC}\sqrt{\nu}}, \quad (7.11)$$

where ν is the rate of measurement.

With this, we estimate that the sensitivity of our protocol for a system of 10^3 NV centers, with $\delta m = 0.3$ and $\nu = 1$ MHz, would be about $\eta \approx 3$ nT Hz $^{-1/2}$. If we increase the system size to 10^{11} centers, we reach $\eta \approx 300$ fT Hz $^{-1/2}$. This is approximately a factor of 3 improvement over the recently demonstrated subpicotesla diamond magnetometry using a large ensemble noninteracting NV centers [163].

Chapter 8

Three-dimensional systems

In this chapter, we study the functioning of the sensing protocol with three-dimensional systems of NV centers. Moving onto the third dimension is particularly important because it is especially challenging to control the implantation depth of the NV centers in a diamond sample [131].

We will first study the cubic lattice geometry and motivate the reason to extend to geometries with random disorder in the system.

8.1 Cubic lattice geometry

As the first step, let us analyze the dipolar interaction V_{ij} (Eq. 7.2) between the NV centers in a cubic lattice geometry. Figure 8.1 shows the dipolar interaction between a spin (sitting at the centre of the axes) and all its nearest neighbours. When integrated over the full solid angle, the ferromagnetic and the anti-ferromagnetic contributions are exactly equal but opposite in sign. Hence, the two contributions cancel each other out and the net dipolar interaction is zero. Without a net dipolar interaction, the first order phase transition no longer exists.

In order to restore this transition, one needs to ensure that the net dipolar interaction between the NV centers is non-zero. We can do this by breaking the symmetry of the dipolar interaction which can be achieved in many ways. In reference [162], it has been shown that one way to do so would be to apply magnetic field gradient along the NV axis where even a small gradient of $\delta B = 10^3$ T/m restores the first order transition.

Here, we present another way to achieve this, by using random disorder. In the following, we study how a random disorder in the system can restore this phase transition and learn about some of its interesting properties.

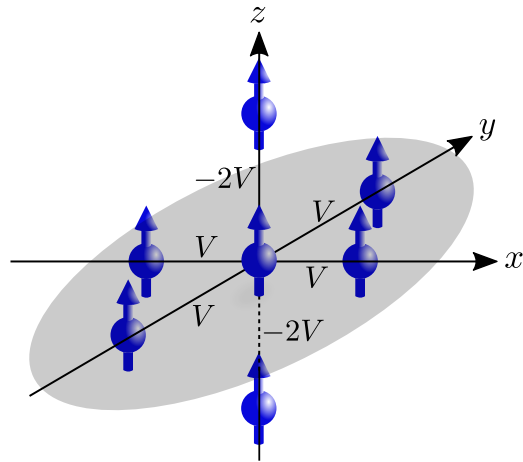


Figure 8.1: The net dipole-dipole interaction in a system of NV centers in a cubic lattice is zero when integrated over the full solid angle in 3D lattice geometry. As a result of this, the first order phase transition no longer exists.

8.2 Random disorder in the system

Going from a system in cubic lattice geometry to one that has random disorder helps us twofold. Firstly, it breaks the symmetry in dipolar interaction that is crucial in restoring the phase transition. Secondly, it relaxes the challenging task to implant NV centers in a perfect lattice geometry.

Figure 8.2 (a) shows the setup of a system of NV centers placed randomly inside a cubic box. To capture the effects of random disorder, we perform simulations for various such random realizations of the system each representing a single Monte Carlo trajectory and then average the obtained results. We take care that the average distance between two centers remains the same for all these realizations.

With such a setup we now investigate the behavior of the total NV magnetization m and the magnetic susceptibility χ similar to the investigations for the two-dimensional lattice systems in chapter 7.

As before, we investigate the peak of the magnetic susceptibility and check its scaling. Figure 8.2 (b) shows such the scaling of the peak of magnetic susceptibility χ with increasing system sizes N . We see that the peak of the magnetic susceptibility diverges, confirming the restoration of the first order phase transition. However, we note that the scaling exponent $\alpha = 0.43$ is slightly smaller than the observed value of $\alpha = 0.2$ in the case of two-dimensional lattice. This may be because we have maintained the average

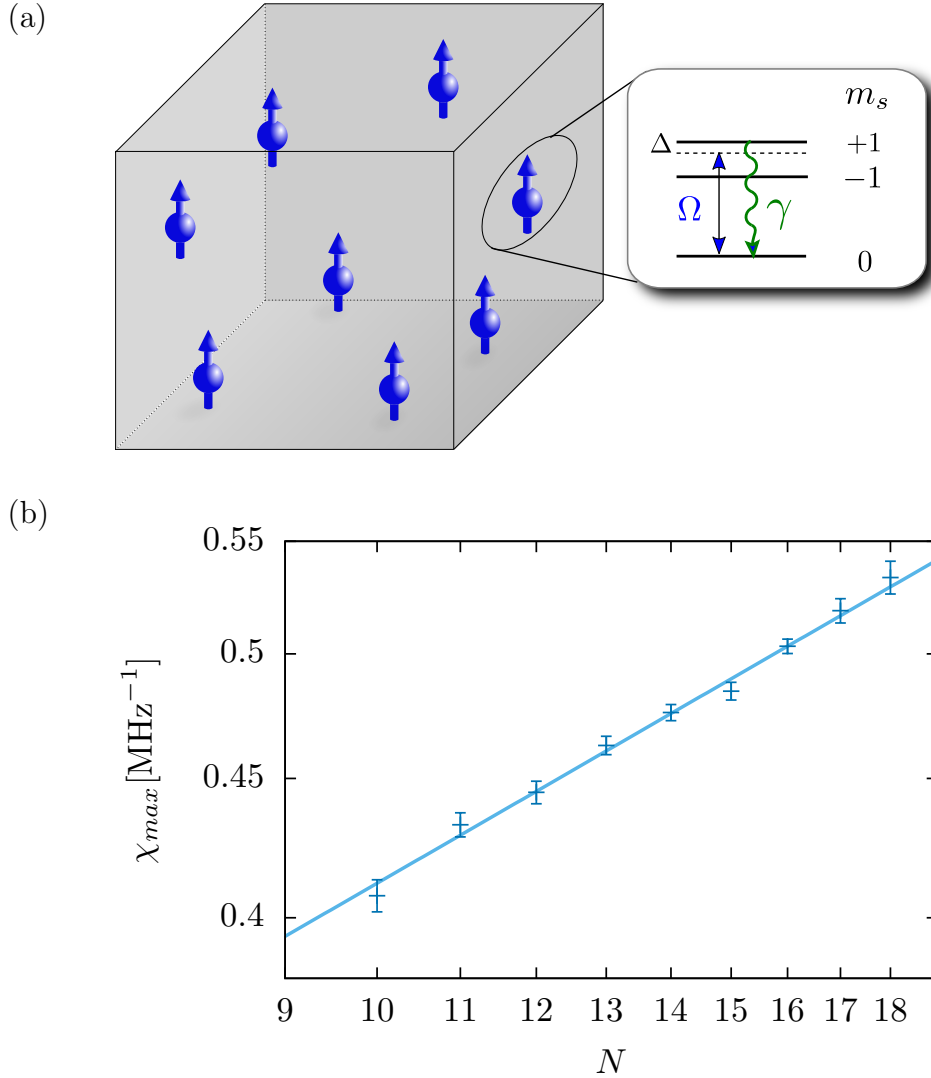


Figure 8.2: (a) Setup of the three-dimensional system of NV centers arranged randomly inside a box. The average distance between two centers for different such realizations is maintained constant. The inset shows the triplet ground state of each spin that can be described using an effective two-level description. (b) Scaling of the peak of magnetic susceptibility χ_{max} with increasing system size N . The diverging peak confirms the restoration of the first order phase transition. The solid line is a fit to the data according to $\chi_{max} \sim N^\alpha$ with the exponent $\alpha = 0.43 \pm 0.02$.

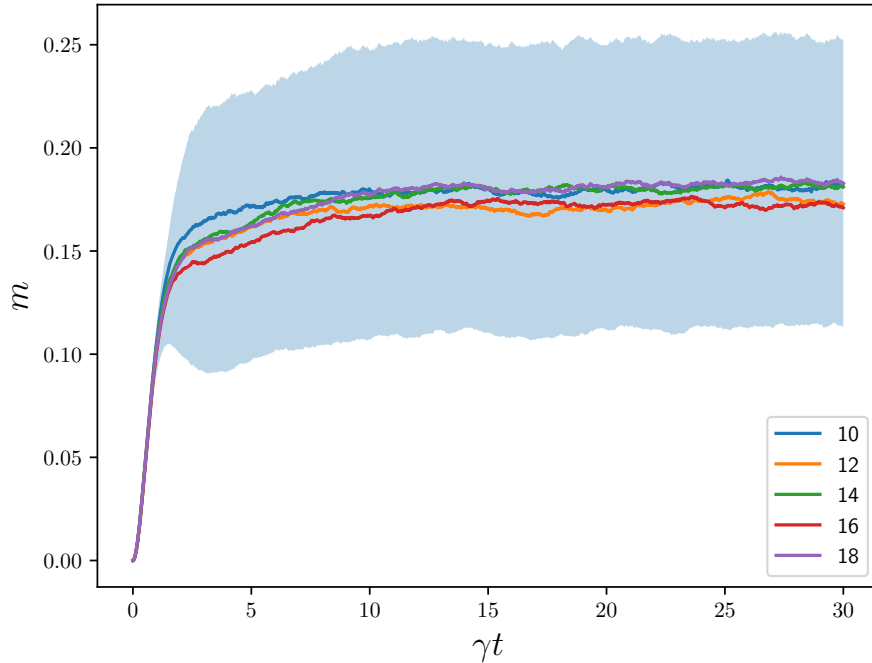


Figure 8.3: Relaxation of the NV magnetization m with time t for various system sizes at the transition point $\Omega = 1$ MHz. The large variance (shaded) in the magnetization is due to the existence of two solutions at the transition.

distance between two NV centers constant, i.e. $\langle r \rangle = \text{constant}$ and not the energy per NV center, i.e. $\langle \frac{1}{r^3} \rangle = \text{constant}$.

Next, let us check the behavior of the NV magnetization at the transition point. The relaxation of the NV magnetization m for progressing times t is shown in figure 8.3 for various system sizes. Similar to the case of two-dimensional lattice geometry in section 7.2, we observe a large variance in m at the transition point as the numerics chooses between the two solutions that exist at the transition. Interestingly, we also observe that the relaxation time does not depend on the size of the system, making the sensing protocol furthermore promising.

In the following we study a few properties of the system in the different regimes of the phase transition.

8.3 Temporal coherence of the NV signal

The second order correlation function $g^{(2)}(\tau)$ is one of the most important tools to learn about the characteristic properties of a photon signal. Here, we calculate this correlation function for the NV readout signal in the three regimes of the phase transitions, i.e., on either side of the phase transition, and, at the phase transition, in order to study its properties.

The second order correlation function is defined as,

$$g^{(2)}(r_1, r_2, \tau) = \frac{\langle I(r_1, t)I(r_2, t + \tau) \rangle}{\langle I(r_1, t) \rangle \langle I(r_2, t) \rangle} \quad (8.1)$$

Since we are interested in the temporal correlation we have $r_1 = r_2 = r$ and the $g^{(2)}$ function only depends on the time difference τ . The $g^{(2)}$ temporal correlation function has the following property that is useful in detecting the coherence of the light signal:

$$\begin{aligned} g^{(2)}(\tau) < g^{(2)}(0) &\implies \text{bunched light} \\ g^{(2)}(\tau) > g^{(2)}(0) &\implies \text{antibunched light.} \end{aligned} \quad (8.2)$$

Let us now calculate the $g^{(2)}$ function for our system. Here, for our purposes, we modify this definition Eq. 8.1 of the correlation function using Bayes' theorem in the following manner,

$$g^{(2)}(\tau) = \left\langle \frac{N [n(t + \tau) > 0 \mid n(t) > 0]}{\langle n(t) \rangle \times N [n(t) > 0]} \right\rangle_{avg}, \quad (8.3)$$

where the average is taken over all the different trajectories of the Monte Carlo simulations. The notations used here reads as follows; $n(t)$ denotes the number of photons emitted at time t , $N[A]$ denotes the number of instances where the event A is true, and, $B|A$ is the usual notation used in conditional probabilities which denotes the case where the event B is true given that the event A is true. We can therefore understand the numerator in Eq. 8.3 as the number of instances where one detects a photon at time $(t + \tau)$ given that a photon was detected at time t . In our numerical simulations, these correspond to the times when a quantum jump has occurred.

Figure 8.4 shows the $g^{(2)}$ correlation function calculated for a system of 16 NV centers at (a) $\Omega = 0.2$ MHz corresponding to the paramagnetic side of the phase transition, (b) $\Omega = 1$ MHz which is at the phase transition, and, (c) $\Omega = 4$ MHz corresponding to the magnetically ordered regime. Using conditions 8.2 of the correlation function, we can see from plots (a)-(c) that

the NV signal changes from antibunching to uncorrelated through the phase transition. Here, we have considered only the spin state readout from the $m_s = 0$ state, but in the future, it would be useful to also consider both optical and infrared signals from $m_s = 1$ state [164, 165].

8.4 Error analysis

It is useful to analyze the error induced by the random disorder. We do this by studying the scaling of the standard deviation σ of the peak of the magnetic susceptibility χ with respect to the number of Monte Carlo trajectories N_{traj} and compare this in the following two scenarios:

- i) all the trajectories correspond to a single realization of the system.
- ii) different trajectories correspond to different configurations of the system.

From figure 8.5, it can be seen that the standard deviation scales basically the same as the expected square root scaling $\Delta O \sim 1/\sqrt{N_{traj}}$ for Monte Carlo simulations as mentioned in section 1.4. However, it is worth noticing that one needs more number of trajectories in order to have quantitatively comparable errors.

8.4 Error analysis

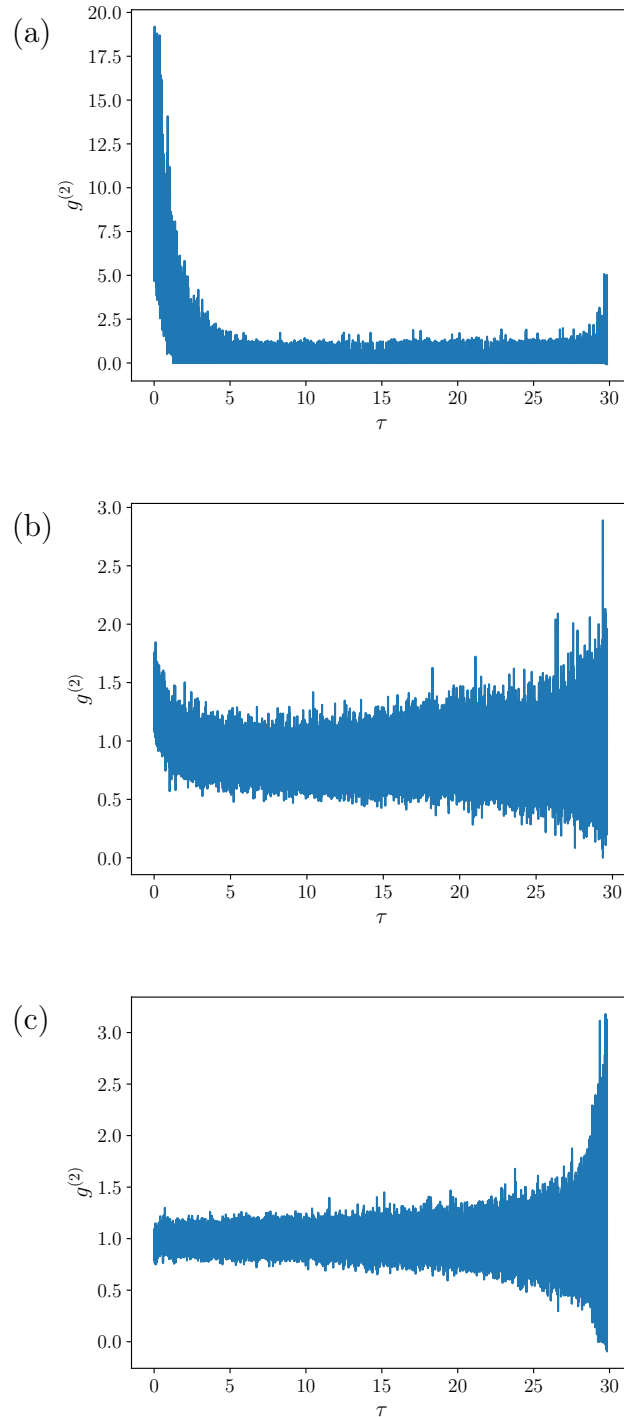


Figure 8.4: Second order auto-correlation function $g^{(2)}(\tau)$ for a system of 16 NV centers at (a) $\Omega = 0.2$ MHz, (b) $\Omega = 1$ MHz, (c) $\Omega = 3.5$ MHz. Results averaged over Monte Carlo simulations of 1000 different realizations.

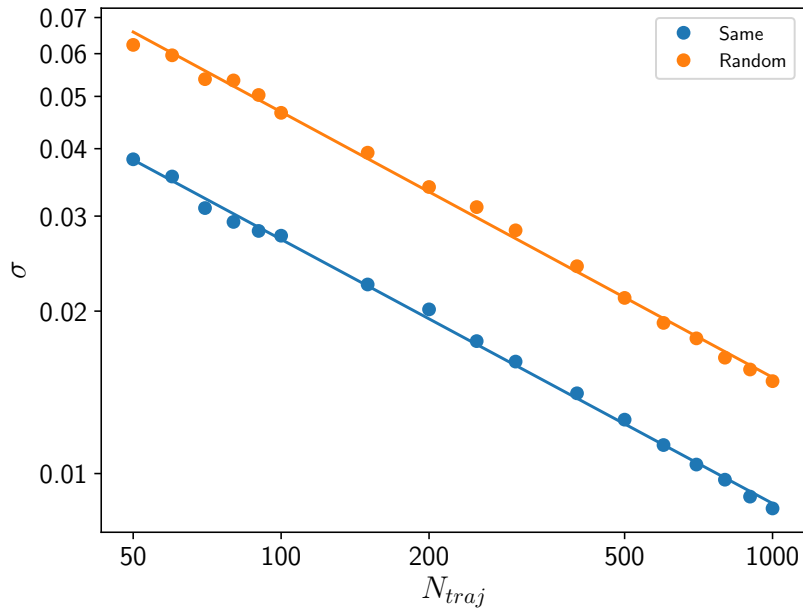


Figure 8.5: Comparison of the scaling of the standard deviation σ of the peak of the magnetic susceptibility with respect to the number of Monte Carlo trajectories N_{traj} , for the case where all the trajectories correspond to a single configuration of the system (blue) and for the case where each of the trajectories correspond to a different configuration (orange). The results are shown on a double logarithmic plot and the solid lines are fits to the data according to $\sigma = \beta/N_{traj}^\alpha$ where $\alpha = 0.489$, $\beta = 0.26$ for the blue curve, and, $\alpha = 0.492$, $\beta = 0.45$ for the orange curve.

Part IV
Conclusion

Chapter 9

Summary and outlook

In this thesis, we presented two examples of quantum technologies that can be enabled by using controlled dissipation. We showed that the system-environment interactions often lead to many interesting features that one can harness in order to build quantum devices that find applications in novel technologies such as quantum simulation and quantum sensing.

In part II, we proposed a novel scheme for the initialization of a quantum simulator where we used a single dissipatively driven auxiliary particle to cool the system to a low-energy state very close to the ground state of the quantum simulator. As a first step we noted down the three parameters that control the cooling dynamics - the strength of the interaction between the system and the auxiliary spin, the rate of the dissipation process at the auxiliary spin, and the energy splitting of the auxiliary spin. Having studied the dependence of the dynamics the system on these parameters of control, we were able to optimize these parameters allowing for maximum cooling achievable in the system. By using the paradigmatic models of the transverse field Ising chain and the antiferromagnetic Heisenberg chain (where the ground state is highly entangled) we showed that this scheme lets us to go beyond the class of stabilizer and frustration-free Hamiltonians. The results showed that this scheme is efficient in the sense that the resources required to perform the task scale only polynomially and not exponentially with the system size. We also showed that the protocol is robust against additional decoherence processes where the characteristic scale is κ (rate of the decoherence process at each of the N sites), which is in contrast to the $N\kappa$ scale observed in typical adiabatic state preparation methods. As an experimental realization of the scheme, we proposed a trapped ion implementation and showed the numerical results for an Ising like system with long-range interactions. Finally, we proposed a method to measure the many-body gap of the system using just the energy

dissipated out of the system.

Future directions of research include the investigation of the scaling behavior upon varying the control parameters in time. The variation of the splitting of the auxiliary spin can be especially useful as it maybe help increasing the number of paths via which an excitement in the system could be cooled down. A second idea for improving the efficiency of the protocol would be to add multiple auxiliary spins. In particular, choosing different values of their splittings would allow the engineering of tailored bath spectral functions for the quantum simulator.

As an extension of the cooling protocol, we also presented the first steps to cool rotational degrees of freedom of a molecule, where we showed the dissipative cooling of the $J = 2$ rotational manifold into the $J = 0$ ground state with a very high fidelity. In the future, it would be useful to generalize the protocol in order to incorporate other rotational degrees of freedom, radio frequency couplings etc.

In part III, we investigated the existence of a dissipative first order phase transition in the magnetization of a system of nitrogen vacancy centers at the critical value of the strength of the driving field. We proposed that using this phase transition that is triggered by the interplay of dissipation and the strong interactions between the centers at high densities, one can perform nanoscale quantum sensing. First, we analyzed a two-dimensional system with a lattice geometry and calculated the magnetic susceptibility at the steady state of the system. Upon a modified finite size scaling that allowed us to also include anisotropic geometries, we found that the reduced magnetic susceptibility, which is the derivative of the magnetization, diverges with the system size proving the existence of a phase transition. We also found the exponent to be the same as that for a system of non-interacting particles indicating that the sensitivity is also of the same order. Upon estimating the sensitivity of the nanoscale dissipative sensor, by extracting information from the finite size scaling behavior, we inferred that the protocol offers a factor of three improvement over the recent demonstration using large ensembles of non-interacting centers. As the next step we extended our protocol to three-dimensional systems. Since there is no phase transition due to net zero dipole-dipole interaction in a three dimensional lattice geometry, we proposed to use random disorder in the system in order to restore the phase transition. By averaging over many random realizations of the system, we again found the diverging behavior of the magnetic susceptibility with increasing system sizes. Finally, we investigated some properties of the phase transition by calculating the second order correlation function for the photon collection (or the jump operator firings) and found that the system changes its behavior from bunching to uncorrelated across the phase transition.

Future directions of research include considering different energies for different NV centers. All calculations shown in this thesis assume that all the NV centers have the same energies. However, this is realistically not the case, because during the implantation of the NV centers in a real diamond sample, there are additional electronic fields that are generated by strains in the sample. This causes different NV centers to have different zero field splittings. This generally results in a decreased T_2 decoherence times, against which the dissipative sensing protocol is typically robust, as already shown. Nevertheless, it would be useful to quantitatively study the effects due to different energies per NV center.

Part V
Appendices

Appendix A

Effective operator formalism

Here, we apply the effective operator formalism to an Ising system with $2+1$ spins. We first separate the ground states $|\lambda_{12}, 0\rangle$ and the excited states $|\lambda_{12}, 1\rangle$ of the total system as shown in figure A.1, and the various couplings between these levels are shown in table A.

The ground state Hamiltonian H_g is constructed by considering all the couplings between the $|\lambda_{12}, 0\rangle$ states, whereas, the excited state Hamiltonian H_e involves all the couplings between the $|\lambda_{12}, 1\rangle$ states.

The effective Lindblad operators are given by

$$L_k = \sqrt{\gamma} |\lambda_k, 0\rangle \langle \lambda_k, 1|, \quad (\text{A.1})$$

where, $\lambda_k = 00, 01, 10, 11$, are the different states of the system excluding the bath spin. We can now write the non-Hermitian Hamiltonian for the excited states as

$$H_{\text{NH}} = H_e - \frac{i}{2} \sum_k L_k^\dagger L_k. \quad (\text{A.2})$$

Finally, the effective Hamiltonian H_{eff} and the effective Lindblad operator L_{eff} for the ground states read,

$$\begin{aligned} H_{\text{eff}} &= -\frac{1}{2} V_- \left[H_{\text{NH}}^{-1} + (H_{\text{NH}}^{-1})^\dagger \right] V_+ + H_g \\ L_{\text{eff}} &= \sum_k L_k H_{\text{NH}}^{-1} V_+ \end{aligned} \quad (\text{A.3})$$

where, V_\pm are the perturbative (de-)excitations from the excited states to the ground states,

$$\begin{aligned} V_+ &= 2g_{sb} [|001\rangle \langle 010| + |101\rangle \langle 110|] \\ V_- &= 2g_{sb} [|010\rangle \langle 001| + |110\rangle \langle 101|]. \end{aligned} \quad (\text{A.4})$$

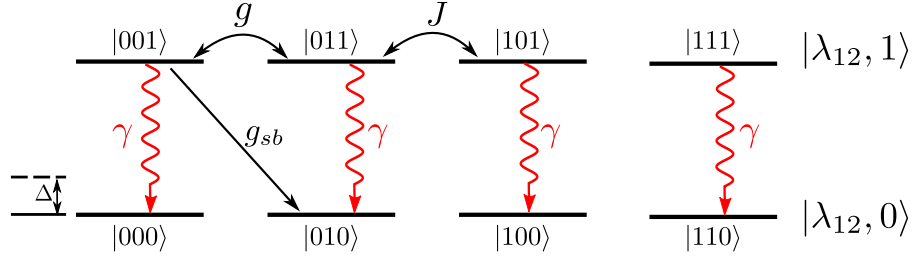


Figure A.1: Effective operator formalism: the ground states and excited states with respect to the auxiliary bath spin are separated into two different manifolds.

The effective rates of decay from a state a to a state b in the ground state manifold is given by,

$$\Gamma_{a \rightarrow b} = |\langle b | L_{\text{eff}} | a \rangle|^2 \quad (\text{A.5})$$

Applying this to our system, and using approximations from series expansions, we find that the ground state is prepared with an effective rate that is proportional to $g_{sb}^2 \gamma$ in the limit of $g_{sb}, \gamma \rightarrow 0$.

	$ 000\rangle$	$ 010\rangle$	$ 100\rangle$	$ 110\rangle$	$ 001\rangle$	$ 011\rangle$	$ 101\rangle$	$ 111\rangle$
$ 000\rangle$	J $+g_{sb}$ $-\Delta$	g	g		γ			
$ 010\rangle$	g	$-J$ $-g_{sb}$ $-\Delta$		g	$2g_{sb}$	γ		
$ 100\rangle$	g		$-J$ g_{sb} $-\Delta$	g			γ	
$ 110\rangle$		g	g	J $-g_{sb}$ $-\Delta$			$2g_{sb}$	γ
$ 001\rangle$		$2g_{sb}$			J $-g_{sb}$ $+\Delta$	g	g	
$ 011\rangle$					g	$-J$ $+g_{sb}$ $+\Delta$		g
$ 101\rangle$				$2g_{sb}$	g		$-J$ $-g_{sb}$ $+\Delta$	g
$ 111\rangle$						g	g	J g_{sb} $+\Delta$

Table A.1: Coupling between various states of the system with $2 + 1$ spins in order to obtain effective Hamiltonian and Lindblad operators.

Appendix B

Critical point of the finite size Ising model

At the thermodynamic limit, the critical point of the transverse field Ising model Eq. 2.3 is at $J = g$. However, for small system sizes this point is slightly shifted because of the finite size effects.

Here, we calculate the critical point for the transverse field Ising model with $N = 5$ spins. To do so, we calculate the magnetization m of the system as a function of the parameter $l = g/J$ and then the magnetic susceptibility $\chi = \partial m / \partial l$. The point corresponding to the peak in susceptibility is then the critical point.

Figure B.1 shows the magnetic susceptibility χ for various values of the ratio l and we see that the susceptibility has a peak at $l = 0.7$, which we take as the critical point. Since in the main text we give all our parameter values in units of g , this corresponds to $J/g = 1.4$,

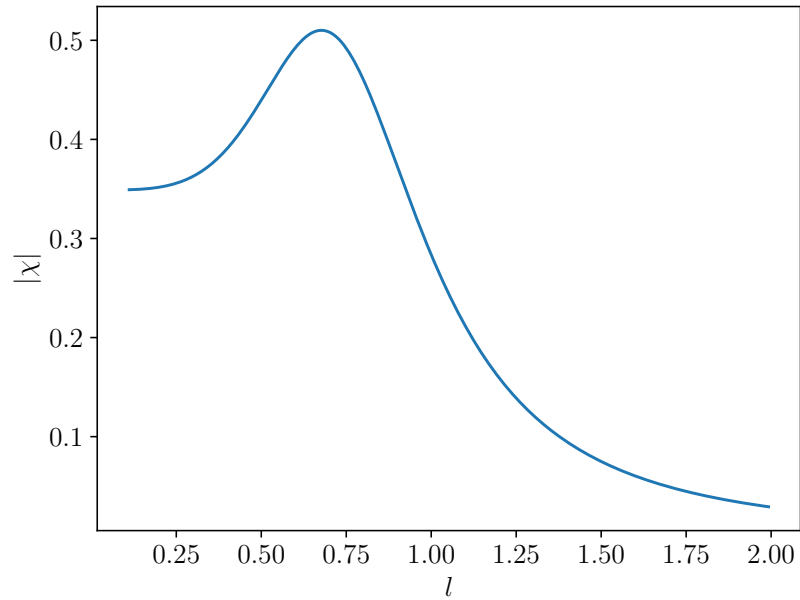


Figure B.1: Magnetic susceptibility χ for different values of the ratio $l = g/J$ for a transverse field Ising model with $N = 5$ spins. The peak of the susceptibility and therefore the critical point corresponds to $l_c = 0.7$.

Appendix C

Lamb-Dicke regime for long-range Ising Hamiltonian

The power-law scaling of the interaction term J_{ij} in the long-range Ising-like Hamiltonian which we consider in section 4.5 is only valid in the Lamb-Dicke regime [87]. Here, we verify that our system of trapped ions is in the Lamb-Dicke regime for the parameters mentioned in section 4.5.

The Lamb-Dicke regime is basically the regime in trapped-ion experiments where the detuning δ is far from each of the normal modes of the ion as compared to the Rabi frequency i.e.,

$$|\delta - \omega_m| \gg \eta_{i,m}\Omega_i. \quad (\text{C.1})$$

Here, the Lamb-Dicke parameter for each normal mode is given by,

$$\eta_{i,m} = b_{i,m}\delta k \sqrt{\frac{\hbar}{2M\omega_m}}, \quad (\text{C.2})$$

where, $b_{i,m}$ refers to the m th normal mode of the i th ion, δk corresponds to the 729nm transition between the spin-up and the spin-down states of each ion, M is the mass of the ion and ω_m is the frequency of the m th normal mode.

The calculations to obtain the eigenfrequencies of the different modes for each of the ions have been performed by Fabian Wolf and Piet O. Schmidt. We plug in these values and construct table C.1, which confirms that the ions are in the Lamb-Dicke regime.

Ion	$ \delta - \omega_m $ (kHz)	$\eta_{i,m}\Omega_i$ (kHz)
1	$2\pi \times 103.63$	$2\pi \times 17.0833$
2	$2\pi \times 1331.47$	$2\pi \times 17.4928$
3	$2\pi \times 673.434$	$2\pi \times 18.1668$
4	$2\pi \times 1142.71$	$2\pi \times 19.2328$
5	$2\pi \times 1782.42$	$2\pi \times 21.0434$
Bath ion	$2\pi \times 2720.37$	$2\pi \times 24.9573$

Table C.1: Table confirming that the trapped ions are in the Lamb-Dicke regime since $|\delta - \omega_m| \gg \eta_{i,m}\Omega_i$ for each of the ions in the Ising-like chain.

Appendix D

NV spin Hamiltonian

Since we describe the NV centers with an effective two-level description as mentioned in section 7.1, we will use the Pauli spin-1/2 matrices σ to represent the NV electron and construct the Hamiltonian. The spin Hamiltonian of one NV center is then given by

$$H_{NV} = D\sigma_z^2 + \gamma_e \vec{B} \cdot \vec{\sigma} \quad (\text{D.1})$$

where \vec{B} is the magnetic field vector, D the zero field splitting, and, γ_e the electron gyromagnetic ratio. The full dipole-dipole interaction between two NV centers at sites i and j can be written as

$$V_{ij} = \frac{C_3}{|\vec{r}_i - \vec{r}_j|^3} \left[P_i^\dagger P_j^\dagger - (\sigma_+^i \sigma_-^j + \sigma_-^i \sigma_+^j) \right] \quad (\text{D.2})$$

where C_3 is the coefficient corresponding to the dipolar term, and the projector $P_i^\dagger = |\uparrow\rangle\langle\uparrow| = (1 + \sigma_z^i)/2$ in the first part projects to the excited states [84] and the second part captures the flip-flop interaction.

Next, we transform the Hamiltonian into the rotating frame of the driving field ω_{RF} using the transformation,

$$H_R = R^\dagger(t) H R(t) - i R^\dagger(t) \frac{d}{dt} R(t) \quad (\text{D.3})$$

where in our case the unitary transformation $R(t)$ is

$$R(t) = e^{i\omega_{RF} t \sigma_z} \quad (\text{D.4})$$

Before applying this transformation to the Hamiltonian, we compute the following,

$$\begin{aligned} R^\dagger(t) \sigma_z R(t) &= e^{-i\omega_{RF} t \sigma_z} \sigma_z e^{i\omega_{RF} t \sigma_z} = \sigma_z \\ R^\dagger(t) \sigma_x R(t) &= \cos \omega_{RF} t \sigma_x + \sin \omega_{RF} t \sigma_y \\ R^\dagger(t) \sigma_y R(t) &= \cos \omega_{RF} t \sigma_y - \sin \omega_{RF} t \sigma_x \end{aligned} \quad (\text{D.5})$$

We also recall that $\sigma_{\pm} = \sigma_x \pm i\sigma_y$ which gives us

$$\sigma_+\sigma_- + \sigma_-\sigma_+ = 2(\sigma_x\sigma_x + \sigma_y\sigma_y) \quad (\text{D.6})$$

Combining and applying these, we obtain the Hamiltonian in the rotating frame as

$$H_R = D\sigma_z^2 + (\gamma_e B_0 + \omega_{RF})\sigma_z + B_1\gamma_e\sigma_x - B_1 \cos 2\omega_{RF}t\gamma_e\sigma_x + B_1 \sin 2\omega_{RF}t\gamma_e\sigma_y \quad (\text{D.7})$$

As the next step we use the rotating wave approximation and neglect rapidly oscillating terms. Here, these correspond to the terms involving $2\omega_{RF}$. The final Hamiltonian then reads,

$$H = \Delta\sigma_z + \Omega\sigma_x + V_{ij} \quad (\text{D.8})$$

with $\Delta = D + \gamma_e B_0 + \omega_{RF}$ and $\Omega = \gamma_e B_1$.

Bibliography

- [1] H.-P. Breuer, F. Petruccione, *The Theory of Open Quantum Systems*, Oxford University Press, Oxford, 2002.
- [2] M. A. Nielsen, I. L. Chuang, *Quantum computation and quantum information*, Cambridge University Press, Cambridge, 2000.
- [3] W. Demtröder, *Laser spectroscopy: basic concepts and instrumentation*, Springer Science & Business Media, 2013.
- [4] M. Müller, S. Diehl, G. Pupillo, P. Zoller, Engineered open systems and quantum simulations with atoms and ions, in: *Advances in Atomic, Molecular, and Optical Physics*, Vol. 61, Elsevier, 2012, pp. 1–80.
- [5] J. Eisert, T. Prosen, Noise-driven quantum criticality, arXiv:1012.5013 (2010).
- [6] M. Hoening, M. Moos, M. Fleischhauer, Critical exponents of steady-state phase transitions in fermionic lattice models, *Physical Review A* 86 (1) (2012) 013606.
- [7] C. Ates, B. Olmos, W. Li, I. Lesanovsky, Dissipative binding of lattice bosons through distance-selective pair loss, *Physical Review Letters* 109 (23) (2012) 233003.
- [8] M. Lemesko, H. Weimer, Dissipative binding of atoms by non-conservative forces, *Nature communications* 4 (2013) 2230.
- [9] S. D. Huber, H. P. Büchler, Dipole-interaction-mediated laser cooling of polar molecules to ultracold temperatures, *Physical Review Letters* 108 (19) (2012) 193006.
- [10] B. Zhao, A. Glaetzle, G. Pupillo, P. Zoller, Atomic rydberg reservoirs for polar molecules, *Physical Review Letters* 108 (19) (2012) 193007.

-
- [11] C. Elouard, G. Thomas, M. Olivier, J. P. Pekola, A. N. Jordan, A quantum heat switch based on a single driven qubit, arXiv:2001.10367 (2020).
- [12] N. Lambert, Y.-N. Chen, Y.-C. Cheng, C.-M. Li, G.-Y. Chen, F. Nori, Quantum biology, *Nature Physics* 9 (1) (2013) 10.
- [13] S. Diehl, A. Micheli, A. Kantian, B. Kraus, H. Büchler, P. Zoller, Quantum states and phases in driven open quantum systems with cold atoms, *Nature Physics* 4 (11) (2008) 878.
- [14] F. Verstraete, M. M. Wolf, J. I. Cirac, Quantum computation and quantum-state engineering driven by dissipation, *Nature physics* 5 (9) (2009) 633.
- [15] H. Weimer, M. Müller, I. Lesanovsky, P. Zoller, H. P. Büchler, A rydberg quantum simulator, *Nature Physics* 6 (5) (2010) 382.
- [16] S. Diehl, W. Yi, A. Daley, P. Zoller, Dissipation-induced d-wave pairing of fermionic atoms in an optical lattice, *Physical Review Letters* 105 (22) (2010) 227001.
- [17] J. T. Barreiro, M. Müller, P. Schindler, D. Nigg, T. Monz, M. Chwalla, M. Hennrich, C. F. Roos, P. Zoller, R. Blatt, An open-system quantum simulator with trapped ions, *Nature* 470 (7335) (2011) 486.
- [18] H. Krauter, C. A. Muschik, K. Jensen, W. Wasilewski, J. M. Petersen, J. I. Cirac, E. S. Polzik, Entanglement generated by dissipation and steady state entanglement of two macroscopic objects, *Physical Review Letters* 107 (8) (2011) 080503.
- [19] E. G. Dalla Torre, J. Otterbach, E. Demler, V. Vuletic, M. D. Lukin, Dissipative preparation of spin squeezed atomic ensembles in a steady state, *Physical Review Letters* 110 (12) (2013) 120402.
- [20] J. Otterbach, M. Lemeshko, Dissipative preparation of spatial order in rydberg-dressed bose-einstein condensates, *Physical Review Letters* 113 (7) (2014) 070401.
- [21] G. De Lange, Z. Wang, D. Riste, V. Dobrovitski, R. Hanson, Universal dynamical decoupling of a single solid-state spin from a spin bath, *Science* 330 (6000) (2010) 60–63.
- [22] Y. Xie, J. Geng, H. Yu, X. Rong, Y. Wang, J. Du, Experimental dissipative quantum sensing, arXiv:1907.11363 (2019).

Bibliography

- [23] S. Alipour, M. Mehboudi, A. Reza khani, Quantum metrology in open systems: dissipative cramer-rao bound, *Physical Review Letters* 112 (12) (2014) 120405.
- [24] F. Reiter, A. S. Sørensen, P. Zoller, C. Muschik, Dissipative quantum error correction and application to quantum sensing with trapped ions, *Nature communications* 8 (1) (2017) 1–11.
- [25] H. Weimer, A. Kshetrimayum, R. Orús, Simulation methods for open quantum many-body systems, *arXiv:1907.07079* (2019).
- [26] J. Dalibard, Y. Castin, K. Mølmer, Wave-function approach to dissipative processes in quantum optics, *Phys. Rev. Lett.* 68 (1992) 580–583.
- [27] K. Mølmer, Y. Castin, J. Dalibard, Monte carlo wave-function method in quantum optics, *J. Opt. Soc. Am. B* 10 (3) (1993) 524–538.
- [28] M. B. Plenio, P. L. Knight, The quantum-jump approach to dissipative dynamics in quantum optics, *Rev. Mod. Phys.* 70 (1998) 101–144.
- [29] J. Johansson, P. Nation, F. Nori, Qutip 2: A python framework for the dynamics of open quantum systems, *Comp. Phys. Comm.* 184 (4) (2013) 1234–1240.
- [30] N. Shammah, S. Ahmed, N. Lambert, S. De Liberato, F. Nori, Open quantum systems with local and collective incoherent processes: Efficient numerical simulations using permutational invariance, *Physical Review A* 98 (6) (2018) 063815.
- [31] J. Preskill, Lecture notes for ph219/cs219: Quantum information, Accessible via <http://www.theory.caltech.edu/people/preskill/ph229> 2015 (1997).
- [32] K. Huang, *Introduction to statistical physics*, Chapman and Hall/CRC, 2009.
- [33] J. W. Gibbs, *The scientific papers of J. Willard Gibbs, Vol. 1*, Longmans, Green and Company, 1906.
- [34] S. Sachdev, Quantum phase transitions, *Handbook of Magnetism and Advanced Magnetic Materials* (2007).
- [35] M. P. Fisher, P. B. Weichman, G. Grinstein, D. S. Fisher, Boson localization and the superfluid-insulator transition, *Physical Review B* 40 (1) (1989) 546.

-
- [36] G. Jaeger, The ehrenfest classification of phase transitions: introduction and evolution, *Archive for history of exact sciences* 53 (1) (1998) 51–81.
- [37] N. Goldenfeld, *Lectures on phase transitions and the renormalization group*, CRC Press, 2018.
- [38] V. Berezinsky, Destruction of long range order in one-dimensional and two-dimensional systems having a continuous symmetry group. i. classical systems, *Zh. Eksp. Teor. Fiz.* 32 (1970) 493–500.
- [39] J. M. Kosterlitz, D. J. Thouless, Ordering, metastability and phase transitions in two-dimensional systems, *Journal of Physics C: Solid State Physics* 6 (7) (1973) 1181.
- [40] V. R. Overbeck, M. F. Maghrebi, A. V. Gorshkov, H. Weimer, Multicritical behavior in dissipative ising models, *Physical Review A* 95 (4) (2017) 042133.
- [41] E. Lieb, T. Schultz, D. Mattis, Two soluble models of an antiferromagnetic chain, *Annals of Physics* 16 (3) (1961) 407–466.
- [42] P. Pfeuty, The one-dimensional ising model with a transverse field, *ANNALS of Physics* 57 (1) (1970) 79–90.
- [43] H. Mikeska, A. Kolezhuk, *One-Dimensional Magnetism*, Vol. 645, 2004, pp. 1–83.
- [44] R. Kubo, The spin-wave theory of antiferromagnetics, *Physical Review* 87 (4) (1952) 568.
- [45] T. Holstein, H. Primakoff, Field dependence of the intrinsic domain magnetization of a ferromagnet, *Physical Review* 58 (12) (1940) 1098.
- [46] I. M. Georgescu, S. Ashhab, F. Nori, Quantum simulation, *Reviews of Modern Physics* 86 (1) (2014) 153.
- [47] R. G. Parr, Density functional theory of atoms and molecules, in: *Horizons of Quantum Chemistry*, Springer, 1980, pp. 5–15.
- [48] U. Schollwöck, The density-matrix renormalization group, *Reviews of modern physics* 77 (1) (2005) 259.
- [49] R. P. Feynman, Simulating physics with computers, *International journal of theoretical physics* 21 (6) (1982) 467–488.

Bibliography

- [50] C. Zalka, Simulating quantum systems on a quantum computer, *Proceedings of the Royal Society of London. Series A: Mathematical, Physical and Engineering Sciences* 454 (1969) (1998) 313–322.
- [51] P. W. Shor, Polynomial-time algorithms for prime factorization and discrete logarithms on a quantum computer, *SIAM review* 41 (2) (1999) 303–332.
- [52] A. Steane, Multiple-particle interference and quantum error correction, *Proceedings of the Royal Society of London. Series A: Mathematical, Physical and Engineering Sciences* 452 (1954) (1996) 2551–2577.
- [53] B. P. Lanyon, C. Hempel, D. Nigg, M. Müller, R. Gerritsma, F. Zähringer, P. Schindler, J. T. Barreiro, M. Rambach, G. Kirchmair, et al., Universal digital quantum simulation with trapped ions, *Science* 334 (6052) (2011) 57–61.
- [54] Y. Salathé, M. Mondal, M. Oppliger, J. Heinsoo, P. Kurpiers, A. Potočnik, A. Mezzacapo, U. Las Heras, L. Lamata, E. Solano, et al., Digital quantum simulation of spin models with circuit quantum electrodynamics, *Physical Review X* 5 (2) (2015) 021027.
- [55] D. Porras, J. I. Cirac, Effective quantum spin systems with trapped ions, *Physical Review Letters* 92 (20) (2004) 207901.
- [56] A. M. Zagoskin, S. Savel’ev, F. Nori, Modeling an adiabatic quantum computer via an exact map to a gas of particles, *Physical Review Letters* 98 (12) (2007) 120503.
- [57] J. Braumüller, M. Marthaler, A. Schneider, A. Stehli, H. Rotzinger, M. Weides, A. V. Ustinov, Analog quantum simulation of the rabi model in the ultra-strong coupling regime, *Nature communications* 8 (1) (2017) 1–8.
- [58] G. D’Ariano, P. L. Presti, Quantum tomography for measuring experimentally the matrix elements of an arbitrary quantum operation, *Physical Review Letters* 86 (19) (2001) 4195.
- [59] G. M. D’Ariano, M. G. Paris, M. F. Sacchi, Quantum tomography, *Advances in Imaging and Electron Physics* 128 (2003) 206–309.
- [60] G. Ortiz, J. E. Gubernatis, E. Knill, R. Laflamme, Quantum algorithms for fermionic simulations, *Physical Review A* 64 (2) (2001) 022319.

-
- [61] R. Somma, G. Ortiz, J. E. Gubernatis, E. Knill, R. Laflamme, Simulating physical phenomena by quantum networks, *Physical Review A* 65 (4) (2002) 042323.
- [62] D. S. Abrams, S. Lloyd, Simulation of many-body fermi systems on a universal quantum computer, *Physical Review Letters* 79 (13) (1997) 2586.
- [63] N. J. Ward, I. Kassal, A. Aspuru-Guzik, Preparation of many-body states for quantum simulation, *The Journal of chemical physics* 130 (19) (2009) 194105.
- [64] I. Kassal, S. P. Jordan, P. J. Love, M. Mohseni, A. Aspuru-Guzik, Polynomial-time quantum algorithm for the simulation of chemical dynamics, *Proceedings of the National Academy of Sciences* 105 (48) (2008) 18681–18686.
- [65] H. Wang, S. Ashhab, F. Nori, Efficient quantum algorithm for preparing molecular-system-like states on a quantum computer, *Physical Review A* 79 (4) (2009) 042335.
- [66] D. G. Cory, R. Laflamme, E. Knill, L. Viola, T. Havel, N. Boulant, G. Boutis, E. Fortunato, S. Lloyd, R. Martinez, et al., Nmr based quantum information processing: Achievements and prospects, *Fortschritte der Physik: Progress of Physics* 48 (9-11) (2000) 875–907.
- [67] L.-A. Wu, M. Byrd, D. Lidar, Polynomial-time simulation of pairing models on a quantum computer, *Physical Review Letters* 89 (5) (2002) 057904.
- [68] A. Aspuru-Guzik, A. D. Dutoi, P. J. Love, M. Head-Gordon, Simulated quantum computation of molecular energies, *Science* 309 (5741) (2005) 1704–1707.
- [69] C. Cormick, A. Bermudez, S. F. Huelga, M. B. Plenio, Dissipative ground-state preparation of a spin chain by a structured environment, *New Journal of Physics* 15 (7) (2013) 073027.
- [70] A. Carr, M. Saffman, Preparation of entangled and antiferromagnetic states by dissipative rydberg pumping, *Physical review letters* 111 (3) (2013) 033607.
- [71] H. Weimer, M. Müller, H. P. Büchler, I. Lesanovsky, Digital quantum simulation with rydberg atoms, *Quantum Information Processing* 10 (6) (2011) 885.

Bibliography

- [72] G. Morigi, J. Eschner, C. Cormick, Y. Lin, D. Leibfried, D. J. Wineland, Dissipative quantum control of a spin chain, *Physical Review Letters* 115 (20) (2015) 200502.
- [73] M. Roghani, H. Weimer, Dissipative preparation of entangled many-body states with rydberg atoms, *Quantum Science and Technology* 3 (3) (2018) 035002.
- [74] F. Reiter, A. S. Sørensen, Effective operator formalism for open quantum systems, *Physical Review A* 85 (3) (2012) 032111.
- [75] J. A. Nelder, R. Mead, A simplex method for function minimization, *The computer journal* 7 (4) (1965) 308–313.
- [76] S. G. Johnson, The nlopt nonlinear-optimization package [software]. URL <http://github.com/stevengj/nlopt>
- [77] R. P. Brent, An algorithm with guaranteed convergence for finding a zero of a function, *The Computer Journal* 14 (4) (1971) 422–425.
- [78] E. Jones, T. Oliphant, P. Peterson, et al., *Scipy: Open source scientific tools for python* (2001).
- [79] C. Kokail, C. Maier, R. van Bijnen, T. Brydges, M. Joshi, P. Jurcevic, C. Muschik, P. Silvi, R. Blatt, C. Roos, et al., Self-verifying variational quantum simulation of lattice models, *Nature* 569 (7756) (2019) 355.
- [80] J. I. Latorre, E. Rico, G. Vidal, Ground state entanglement in quantum spin chains, *arXiv preprint quant-ph/0304098* (2003).
- [81] G. Vidal, R. F. Werner, Computable measure of entanglement, *Phys. Rev. A* 65 (2002) 032314.
- [82] J. Eisert, M. Cramer, M. B. Plenio, *Colloquium: Area laws for the entanglement entropy*, *Rev. Mod. Phys.* 82 (2010) 277–306.
- [83] D. Gross, S. T. Flammia, J. Eisert, Most quantum states are too entangled to be useful as computational resources, *Phys. Rev. Lett.* 102 (2009) 190501.
- [84] H. Weimer, N. Y. Yao, C. R. Laumann, M. D. Lukin, Long-range quantum gates using dipolar crystals, *Phys. Rev. Lett.* 108 (2012) 100501.
- [85] P. Jurcevic, B. P. Lanyon, P. Hauke, C. Hempel, P. Zoller, R. Blatt, C. F. Roos, Quasiparticle engineering and entanglement propagation in a quantum many-body system, *Nature* 511 (7508) (2014) 202–205.

-
- [86] J. Zhang, G. Pagano, P. W. Hess, A. Kyprianidis, P. Becker, H. Kaplan, A. V. Gorshkov, Z.-X. Gong, C. Monroe, Observation of a many-body dynamical phase transition with a 53-qubit quantum simulator, *Nature* 551 (7682) (2017) 601–604.
- [87] K. Kim, M.-S. Chang, R. Islam, S. Korenblit, L.-M. Duan, C. Monroe, Entanglement and tunable spin-spin couplings between trapped ions using multiple transverse modes, *Physical Review Letters* 103 (12) (2009) 120502.
- [88] J. Benhelm, G. Kirchmair, C. F. Roos, R. Blatt, Towards fault-tolerant quantum computing with trapped ions, *Nature Physics* 4 (6) (2008) 463–466.
- [89] C. F. Roos, Ion trap quantum gates with amplitude-modulated laser beams, *New Journal of Physics* 10 (1) (2008) 013002.
- [90] T. Ruster, C. T. Schmiegelow, H. Kaufmann, C. Warschburger, F. Schmidt-Kaler, U. G. Poschinger, A long-lived zeeman trapped-ion qubit, *Applied Physics B* 122 (10) (2016) 254.
- [91] M. Drewsen, A. Mortensen, R. Martinussen, P. Sta anum, J. L. Sørensen, Nondestructive identification of cold and extremely localized single molecular ions, *Physical Review Letters* 93 (24) (2004) 243201.
- [92] J. Koelemeij, B. Roth, A. Wicht, I. Ernsting, S. Schiller, Vibrational spectroscopy of hd^+ with 2-ppb accuracy, *Physical Review Letters* 98 (17) (2007) 173002.
- [93] T. Rosenband, P. O. Schmidt, D. B. Hume, W. M. Itano, T. M. Fortier, J. E. Stalnaker, K. Kim, S. A. Diddams, J. Koelemeij, J. Bergquist, et al., Observation of the $s\ 0\ 1\ p\ 0\ 3$ clock transition in al^+ 27, *Physical Review Letters* 98 (22) (2007) 220801.
- [94] M. Herrmann, V. Batteiger, S. Knünz, G. Saathoff, T. Udem, T. Hänsch, Frequency metrology on single trapped ions in the weak binding limit: The $3\ s\ 1/2\ -\ 3\ p\ 3/2$ transition in mg^+ 24, *Physical Review Letters* 102 (1) (2009) 013006.
- [95] K. Højbjerg, D. Offenber, C. Bisgaard, H. Stapelfeldt, P. Sta anum, A. Mortensen, M. Drewsen, Consecutive photodissociation of a single complex molecular ion, *Physical Review A* 77 (3) (2008) 030702.

Bibliography

- [96] P. F. Staantum, K. Højbjerg, R. Wester, M. Drewsen, Probing isotope effects in chemical reactions using single ions, *Physical Review Letters* 100 (24) (2008) 243003.
- [97] T. Mitchell, J. Bollinger, D. Dubin, X.-P. Huang, W. Itano, R. Baughman, Direct observations of structural phase transitions in planar crystallized ion plasmas, *Science* 282 (5392) (1998) 1290–1293.
- [98] A. D. Ludlow, M. M. Boyd, J. Ye, E. Peik, P. O. Schmidt, Optical atomic clocks, *Reviews of Modern Physics* 87 (2) (2015) 637.
- [99] R. Blatt, C. F. Roos, Quantum simulations with trapped ions, *Nature Physics* 8 (4) (2012) 277–284.
- [100] D. Leibfried, B. DeMarco, V. Meyer, D. Lucas, M. Barrett, J. Britton, W. M. Itano, B. Jelenković, C. Langer, T. Rosenband, et al., Experimental demonstration of a robust, high-fidelity geometric two ion-qubit phase gate, *Nature* 422 (6930) (2003) 412–415.
- [101] R. Blatt, D. Wineland, Entangled states of trapped atomic ions, *Nature* 453 (7198) (2008) 1008–1015.
- [102] Y. Wan, F. Gebert, F. Wolf, P. O. Schmidt, Efficient sympathetic motional-ground-state cooling of a molecular ion, *Physical Review A* 91 (4) (2015) 043425.
- [103] C.-w. Chou, C. Kurz, D. B. Hume, P. N. Plessow, D. R. Leibbrandt, D. Leibfried, Preparation and coherent manipulation of pure quantum states of a single molecular ion, *Nature* 545 (7653) (2017) 203–207.
- [104] C. N. Banwell, E. M. McCash, et al., *Fundamentals of molecular spectroscopy*, Vol. 851, McGraw-Hill New York, 1994.
- [105] I. Aharonovich, S. Castelletto, D. Simpson, C. Su, A. Greentree, S. Prawer, Diamond-based single-photon emitters, *Reports on progress in Physics* 74 (7) (2011) 076501.
- [106] L. Childress, R. Walsworth, M. Lukin, Atom-like crystal defects: From quantum computers to biological sensors, *Physics Today* 67 (10) (2014) 38.
- [107] R. Schirhagl, K. Chang, M. Loretz, C. L. Degen, Nitrogen-vacancy centers in diamond: nanoscale sensors for physics and biology, *Annual review of physical chemistry* 65 (2014) 83–105.

-
- [108] J. F. Barry, J. M. Schloss, E. Bauch, M. J. Turner, C. A. Hart, L. M. Pham, R. L. Walsworth, Sensitivity optimization for nv-diamond magnetometry (2019). [arXiv:1903.08176](https://arxiv.org/abs/1903.08176).
- [109] M. W. Doherty, N. B. Manson, P. Delaney, F. Jelezko, J. Wrachtrup, L. C. Hollenberg, The nitrogen-vacancy colour centre in diamond, *Physics Reports* 528 (1) (2013) 1–45.
- [110] M. G. Dutt, L. Childress, L. Jiang, E. Togan, J. Maze, F. Jelezko, A. Zibrov, P. Hemmer, M. Lukin, Quantum register based on individual electronic and nuclear spin qubits in diamond, *Science* 316 (5829) (2007) 1312–1316.
- [111] P. Neumann, N. Mizuochi, F. Rempp, P. Hemmer, H. Watanabe, S. Yamasaki, V. Jacques, T. Gaebel, F. Jelezko, J. Wrachtrup, Multipartite entanglement among single spins in diamond, *science* 320 (5881) (2008) 1326–1329.
- [112] J. Taylor, P. Cappellaro, L. Childress, L. Jiang, D. Budker, P. Hemmer, A. Yacoby, R. Walsworth, M. Lukin, High-sensitivity diamond magnetometer with nanoscale resolution, *Nature Physics* 4 (10) (2008) 810.
- [113] G. Balasubramanian, I. Chan, R. Kolesov, M. Al-Hmoud, J. Tisler, C. Shin, C. Kim, A. Wojcik, P. R. Hemmer, A. Krueger, et al., Nanoscale imaging magnetometry with diamond spins under ambient conditions, *Nature* 455 (7213) (2008) 648.
- [114] J. Maze, P. Stanwix, J. Hodges, S. Hong, J. Taylor, P. Cappellaro, L. Jiang, M. G. Dutt, E. Togan, A. Zibrov, et al., Nanoscale magnetic sensing with an individual electronic spin in diamond, *Nature* 455 (7213) (2008) 644.
- [115] G. Balasubramanian, P. Neumann, D. Twitchen, M. Markham, R. Kolesov, N. Mizuochi, J. Isoya, J. Achard, J. Beck, J. Tissler, et al., Ultralong spin coherence time in isotopically engineered diamond, *Nature materials* 8 (5) (2009) 383.
- [116] F. Dolde, H. Fedder, M. W. Doherty, T. Nöbauer, F. Rempp, G. Balasubramanian, T. Wolf, F. Reinhard, L. C. Hollenberg, F. Jelezko, et al., Electric-field sensing using single diamond spins, *Nature Physics* 7 (6) (2011) 459.

Bibliography

- [117] V. M. Acosta, E. Bauch, M. P. Ledbetter, A. Waxman, L.-S. Bouchard, D. Budker, Temperature dependence of the nitrogen-vacancy magnetic resonance in diamond, *Physical Review Letters* 104 (7) (2010) 070801.
- [118] D. Toyli, D. Christle, A. Alkauskas, B. Buckley, C. Van de Walle, D. Awschalom, Measurement and control of single nitrogen-vacancy center spins above 600 k, *Physical Review X* 2 (3) (2012) 031001.
- [119] A. Lenef, S. Rand, Electronic structure of the n-v center in diamond: Theory, *Physical Review B* 53 (20) (1996) 13441.
- [120] G. Davies, M. Hamer, Optical studies of the 1.945 eV vibronic band in diamond, *Proceedings of the Royal Society of London. A. Mathematical and Physical Sciences* 348 (1653) (1976) 285–298.
- [121] N. Manson, J. Harrison, M. Sellars, Nitrogen-vacancy center in diamond: Model of the electronic structure and associated dynamics, *Physical Review B* 74 (10) (2006) 104303.
- [122] L. Rogers, S. Armstrong, M. Sellars, N. Manson, Infrared emission of the NV centre in diamond: Zeeman and uniaxial stress studies, *New Journal of Physics* 10 (10) (2008) 103024.
- [123] V. Acosta, A. Jarmola, E. Bauch, D. Budker, Optical properties of the nitrogen-vacancy singlet levels in diamond, *Physical Review B* 82 (20) (2010) 201202.
- [124] V. M. Acosta, Optical magnetometry with nitrogen-vacancy centers in diamond, Ph.D. thesis, UC Berkeley (2011).
- [125] L. Robledo, L. Childress, H. Bernien, B. Hensen, P. F. Alkemade, R. Hanson, High-fidelity projective read-out of a solid-state spin quantum register, *Nature* 477 (7366) (2011) 574.
- [126] B. Maertz, A. Wijnheijmer, G. Fuchs, M. Nowakowski, D. Awschalom, Vector magnetic field microscopy using nitrogen vacancy centers in diamond, *Applied Physics Letters* 96 (9) (2010) 092504.
- [127] S. Steinert, F. Dolde, P. Neumann, A. Aird, B. Naydenov, G. Balasubramanian, F. Jelezko, J. Wrachtrup, High sensitivity magnetic imaging using an array of spins in diamond, *Review of scientific instruments* 81 (4) (2010) 043705.

-
- [128] R. S. Schoenfeld, W. Harneit, Real time magnetic field sensing and imaging using a single spin in diamond, *Physical Review Letters* 106 (3) (2011) 030802.
- [129] C. Degen, Scanning magnetic field microscope with a diamond single-spin sensor, *Applied Physics Letters* 92 (24) (2008) 243111.
- [130] V. M. Acosta, E. Bauch, M. P. Ledbetter, C. Santori, K.-M. Fu, P. E. Barclay, R. G. Beausoleil, H. Linget, J. F. Roch, F. Treussart, et al., Diamonds with a high density of nitrogen-vacancy centers for magnetometry applications, *Physical Review B* 80 (11) (2009) 115202.
- [131] L. Rondin, J.-P. Tetienne, T. Hingant, J.-F. Roch, P. Maletinsky, V. Jacques, Magnetometry with nitrogen-vacancy defects in diamond, *Reports on progress in physics* 77 (5) (2014) 056503.
- [132] F. Casola, T. van der Sar, A. Yacoby, Probing condensed matter physics with magnetometry based on nitrogen-vacancy centres in diamond, *Nature Reviews Materials* 3 (1) (2018) 17088.
- [133] Y. Schlüssel, T. Lenz, D. Rohner, Y. Bar-Haim, L. Bougas, D. Groswasser, M. Kieschnick, E. Rozenberg, L. Thiel, A. Waxman, et al., Wide-field imaging of superconductor vortices with electron spins in diamond, *Physical Review Applied* 10 (3) (2018) 034032.
- [134] Y. Wu, F. Jelezko, M. B. Plenio, T. Weil, Diamond quantum devices in biology, *Angewandte Chemie International Edition* 55 (23) (2016) 6586–6598.
- [135] D. Budker, M. Romalis, Optical magnetometry, *Nature Physics* 3 (4) (2007) 227.
- [136] A. Grosz, M. J. Haji-Sheikh, S. C. Mukhopadhyay, High sensitivity magnetometers, Springer, 2017.
- [137] S. J. Bending, Local magnetic probes of superconductors, *Advances in Physics* 48 (4) (1999) 449–535.
- [138] L. M. Pham, S. J. DeVience, F. Casola, I. Lovchinsky, A. O. Sushkov, E. Bersin, J. Lee, E. Urbach, P. Cappellaro, H. Park, et al., Nmr technique for determining the depth of shallow nitrogen-vacancy centers in diamond, *Physical Review B* 93 (4) (2016) 045425.

Bibliography

- [139] M. Grinolds, M. Warner, K. De Greve, Y. Dovzhenko, L. Thiel, R. L. Walsworth, S. Hong, P. Maletinsky, A. Yacoby, Subnanometre resolution in three-dimensional magnetic resonance imaging of individual dark spins, *Nature nanotechnology* 9 (4) (2014) 279.
- [140] K. Arai, C. Belthangady, H. Zhang, N. Bar-Gill, S. DeVience, P. Cappellaro, A. Yacoby, R. L. Walsworth, Fourier magnetic imaging with nanoscale resolution and compressed sensing speed-up using electronic spins in diamond, *Nature nanotechnology* 10 (10) (2015) 859.
- [141] . R. Wang, C. Nisoli, R. S. d. Freitas, J. Li, W. McConville, B. Cooley, M. Lund, N. Samarth, C. Leighton, V. H. Crespi, et al., Artificial ‘spin ice’ in a geometrically frustrated lattice of nanoscale ferromagnetic islands, *Nature* 439 (7074) (2006) 303–306.
- [142] M. Z. Hasan, J. E. Moore, Three-dimensional topological insulators, *Annu. Rev. Condens. Matter Phys.* 2 (1) (2011) 55–78.
- [143] S. Heinze, K. Von Bergmann, M. Menzel, J. Brede, A. Kubetzka, R. Wiesendanger, G. Bihlmayer, S. Blügel, Spontaneous atomic-scale magnetic skyrmion lattice in two dimensions, *Nature Physics* 7 (9) (2011) 713–718.
- [144] A. Thiaville, S. Rohart, É. Jué, V. Cros, A. Fert, Dynamics of dzyaloshinskii domain walls in ultrathin magnetic films, *Europhysics Letters* 100 (5) (2012) 57002.
- [145] F. Dolde, The nitrogen vacancy center in internal and external fields, Ph.D. thesis (2014).
- [146] E. Bauch, S. Singh, J. Lee, C. A. Hart, J. M. Schloss, M. J. Turner, J. F. Barry, L. Pham, N. Bar-Gill, S. F. Yelin, et al., Decoherence of dipolar spin ensembles in diamond, arXiv:1904.08763 (2019).
- [147] J. Choi, S. Choi, G. Kucsko, P. C. Maurer, B. J. Shields, H. Sumiya, S. Onoda, J. Isoya, E. Demler, F. Jelezko, et al., Depolarization dynamics in a strongly interacting solid-state spin ensemble, *Physical Review Letters* 118 (9) (2017) 093601.
- [148] M. F. O’Keeffe, L. Horesh, J. F. Barry, D. A. Braje, I. L. Chuang, Hamiltonian engineering with constrained optimization for quantum sensing and control, *New Journal of Physics* 21 (2) (2019) 023015.

-
- [149] S. Choi, N. Y. Yao, M. D. Lukin, Dynamical engineering of interactions in qudit ensembles, *Physical Review Letters* 119 (18) (2017) 183603.
- [150] S. Choi, N. Y. Yao, M. D. Lukin, Quantum metrology based on strongly correlated matter, arXiv:1801.00042 (2017).
- [151] L.-P. Yang, Z. Jacob, Quantum critical detector: amplifying weak signals using discontinuous quantum phase transitions, *Optics express* 27 (8) (2019) 10482–10494.
- [152] T. Karin, S. Dunham, K.-M. Fu, Alignment of the diamond nitrogen vacancy center by strain engineering, *Applied Physics Letters* 105 (5) (2014) 053106.
- [153] T. E. Lee, H. Häffner, M. Cross, Antiferromagnetic phase transition in a nonequilibrium lattice of rydberg atoms, *Physical Review A* 84 (3) (2011) 031402.
- [154] J. Qian, L. Zhou, W. Zhang, Quantum phases of strongly interacting rydberg atoms in triangular lattices, *Physical Review A* 87 (6) (2013) 063421.
- [155] H. Weimer, Variational analysis of driven-dissipative rydberg gases, *Physical Review A* 91 (6) (2015) 063401.
- [156] R. S. Maier, D. L. Stein, Limiting exit location distributions in the stochastic exit problem, *SIAM Journal on Applied Mathematics* 57 (3) (1997) 752–790.
- [157] D. A. Adams, L. M. Sander, R. M. Ziff, The barrier method: A technique for calculating very long transition times, *The Journal of chemical physics* 133 (12) (2010) 124103.
- [158] K. Binder, J. S. Wang, Finite-size effects at critical points with anisotropic correlations: Phenomenological scaling theory and monte carlo simulations, *J. Stat. Phys.* 55 (1) (1989) 87–126.
- [159] K. Binder, A. P. Young, Spin glasses: Experimental facts, theoretical concepts, and open questions, *Rev. Mod. Phys.* 58 (1986) 801–976.
- [160] H. Weimer, Variational principle for steady states of dissipative quantum many-body systems, *Physical Review Letters* 114 (4) (2015) 040402.

Bibliography

- [161] M. F. Maghrebi, A. V. Gorshkov, Nonequilibrium many-body steady states via keldysh formalism, *Physical Review B* 93 (1) (2016) 014307.
- [162] M. Raghunandan, J. Wrachtrup, H. Weimer, High-density quantum sensing with dissipative first order transitions, *Physical Review Letters* 120 (15) (2018) 150501.
- [163] T. Wolf, P. Neumann, K. Nakamura, H. Sumiya, T. Ohshima, J. Isoya, J. Wrachtrup, Subpicotesla diamond magnetometry, *Physical Review X* 5 (4) (2015) 041001.
- [164] L. Robledo, H. Bernien, T. Van Der Sar, R. Hanson, Spin dynamics in the optical cycle of single nitrogen-vacancy centres in diamond, *New Journal of Physics* 13 (2) (2011) 025013.
- [165] I. Meirzada, S. A. Wolf, A. Naiman, U. Levy, N. Bar-Gill, Enhanced spin state readout of nitrogen-vacancy centers in diamond using ir fluorescence, *arXiv:1906.05055* (2019).

Acknowledgements

I would like to begin by sincerely thanking my supervisor Dr. Hendrik Weimer, for his invaluable guidance that made this thesis possible. Working with you has been such a pleasure and I have learned so much from you. Even under times of pressure you have remained pleasantly calm and offered me great advice and support. Your deep expertise in the field has immensely helped me manoeuvre my way through all my projects.

I express my gratitude for my collaborators Prof. Dr. Jörg Wrachtrup and Dr. Durga Dasari in Stuttgart, and, Prof. Dr. Piet O. Schmidt, Prof. Dr. Christian Ospelkaus and Dr. Fabian Wolf, here in Hannover and Braunschweig. Working with you has helped me gain some knowledge about the experimental side of physics.

I would also like to convey my deep gratitude towards Prof. Dr. Klemens Hammerer and Prof. Dr. Markus Müller for taking the time out of their busy schedules to be a part of my thesis advisory committee. I also thank Prof. Dr. Silke Ospelkaus for kindly agreeing to chair my disputation.

I take this opportunity to thank the administrators of the ITP computing cluster and the LUIS computing cluster who have been working very hard to solve all our IT problems and keep our computers updated and running. I also thank all our secretaries for their cheerful support and for making the bureaucracy work not so dreadful.

I acknowledge financial support from the Volkswagen Foundation and the SFB DQ-mat for providing me with the opportunity to pursue my doctoral studies here in Germany.

Members of the Weimer group and the Santos group, be it present or past, have immensely enriched my PhD life. The conversations at lunch everyday have spanned a large variety of interesting topics making it very enjoyable. I thank Tim for being a great office mate and always lending me an ear, be it for physics or for every other discussions we have had. I have made some unforgettable memories with Vincent, Lorenzo, Javad, Arya, Lars, Amit, and Wei Han, which I would fondly cherish and deeply miss in the future.

I would also like to thank all my friends elsewhere for always being there with me through times thick and thin.

I thank my parents and my brother from the bottom of my heart for always providing me with great emotional support in all my endeavors. I am forever indebted to you for being so comforting and understanding even from miles away. I also thank the rest of my family for wishing my well-being.

I consider myself fortunate to have found a very lovely family-in-law. I thank you for all the warmth with which you have welcomed me and for making it very easy for me to integrate into the German society. Ohne euch hätte ich nicht so schnell Deutsch lernen können.

Finally, I would like to thank my fiancé, Florian Fitzek. Your unwavering encouragement has been a great support during times of doubt and your unconditional love has never failed to spark a joy in me. Thank you for basically everything.

Publications

Parts of the content of this thesis has been published previously in the following manuscripts:

- Meghana Raghunandan, Fabian Wolf, Christian Ospelkaus, Piet O. Schmidt, and Hendrik Weimer
"Initialization of Quantum Simulators by Sympathetic Cooling"
Sci. Adv., in press (arxiv:1901.02019)
- Meghana Raghunandan, Jörg Wrachtrup, and Hendrik Weimer
"High-Density Quantum Sensing with Dissipative First Order Transitions"
Phys. Rev. Lett. **120**, 150501 (2018)

Contents of chapter 8 will be published in the following manuscript which is currently in preparation:

- Meghana Raghunandan, Durga Dasari, Jörg Wrachtrup, and Hendrik Weimer
"Dissipative first order transition in disordered nitrogen-vacancy ensemble"
(to be submitted to *Phys. Rev. B*)

Curriculum Vitae

Meghana Raghunandan
Am Hirtenbach 27,
30457 Hannover,
Lower Saxony, Germany

Email: raghunandan.meghana@gmail.com
Mobile: +49 17695323907

Personal details

Date of birth	:	25.08.1992
Place of birth	:	Bengaluru, India
Gender	:	Female
Nationality	:	Indian

Education

since Dec 2015	:	Doctoral student in Physics, Leibniz University Hannover
2010 - 2015	:	BS-MS Dual degree programme, IISER Pune, India
2008 - 2010	:	Pre-University College, Bangalore, India

Selbstständigkeitserklärung

Hiermit versichere ich, die vorliegende Doktorarbeit selbstständig und unter ausschließlicher Verwendung der angegebenen Hilfsmittel angefertigt zu haben.

Meghana Raghunandan

Hannover, Februar 2020